

MODELING AND MANUFACTURING OF ADAPTIVE PLATES INCORPORATING PIEZOELECTRIC FIBER COMPOSITE PLIES

by

John P. Rodgers

Submitted to the Department of
Aeronautics and Astronautics in Partial
Fulfillment of the Requirements for the
Degree of


Master of Science
in Aeronautics and Astronautics
at the

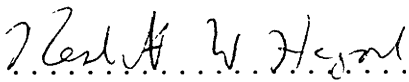
Massachusetts Institute of Technology

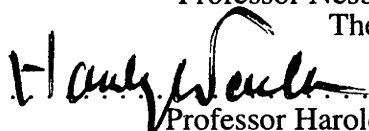
May 1995

© 1995 John P. Rodgers
All rights reserved

The author hereby grants to MIT permission to reproduce and to
distribute publicly paper and electronic copies of this thesis
document in whole or in part

Signature of Author 
Department of Aeronautics and Astronautics
May 22, 1995

Certified by 
Professor Nesbitt W. Hagood
Thesis Supervisor

Accepted by 
Professor Harold Y. Wachman
Chairman, Department Graduate Committee

MASSACHUSETTS INSTITUTE
OF TECHNOLOGY

JUL 07 1995

LIBRARIES

ARCHIVES

MODELING AND MANUFACTURING OF ADAPTIVE PLATES INCORPORATING PIEZOELECTRIC FIBER COMPOSITE PLIES

by

John P. Rodgers

Submitted to the Department of Aeronautics and Astronautics on May 22, 1995
in Partial Fulfillment of the Requirements for the Degree of Master of Science in
Aeronautics and Astronautics

Abstract

Adaptive composite plates with embedded piezoelectric fiber composite actuators have been manufactured and tested. The response of the adaptive plates has also been modeled using a Rayleigh Ritz assumed modes method and Classical Laminated Plate Theory. The model was used to aid in the design of an adaptive plate capable of independent bending and twisting actuation using a pair of anisotropic active plies. The active plies were composed of parallel piezoceramic fibers in an epoxy-based matrix and surrounded by interlaminar electrode layers. The actuators were manufactured in the form of a conformable prepreg tape which could be incorporated as active plies in a standard graphite/epoxy laminate manufacturing process. Independent bending and twisting modes of operation were demonstrated experimentally for a cantilevered plate. In addition, model predictions were compared with measured values for the bend and twist response of the adaptive plates over a range of frequencies. A number of unmodeled effects were found to be significant including high field piezoelectric nonlinearities and a frequency dependence. Data from free and embedded actuators were used to further characterize these effects. The frequency dependent effects have been attributed to a low frequency transition between a resistive-dominated and a capacitance-dominated electromechanical system. In addition, data collected on the stiffness of the actuators suggest that a stiff load transfer path greatly improves the effective stiffness of the piezoelectric fibers. Finally, a comparison with a perfect composite actuator, having ideal properties, was used to evaluate the performance of the active plies. Current actuation capabilities were found to be substantially below the ideal levels as a result of reduced piezoelectric anisotropy and fiber stiffness. Suggestions are made for future improvements in the piezoelectric fiber composites.

Thesis Supervisor: Dr. Nesbitt W. Hagood
Title: Assistant Professor of Aeronautics and Astronautics

Acknowledgments

This work was supported by a grant from the Office of Naval Research (# N00-14-92-J-4067), with Dr. Wallace Smith serving as technical monitor. The support of the Space Engineering Research Center (SERC) and the Technology Laboratory for Advanced Composites (TELAC) has been greatly appreciated. Many individuals contributed to the accomplishments of this work and deserve a great deal of thanks. Mr. Aaron Bent and Mr. Kin Chan provided much of the general background knowledge on piezoelectric fiber composites and active materials. Mr. Kamyar Ghandi provided endless technical assistance with data acquisition and presentation. Ms. Zachira Castro, Mr. Al Supple, and Mr. Alessandro Pizzochero provided immeasurable assistance in the lab. Finally, the support of Miss Margaret Best with typing, editing, and encouragement was greatly appreciated.

Biographical Note

The author is a native of Miami, Florida, where he attended Miami Sunset Senior High School, graduating in 1989. He next attended Duke University in Durham, North Carolina, from September of 1989 through December of 1992. He was awarded a Bachelor of Science in Engineering Degree from the Department of Mechanical Engineering and Materials Science, with a second major from the Department of Mathematics. The author then began his graduate studies at the Massachusetts Institute of Technology in Cambridge, Massachusetts, in January of 1993.

Table of Contents

Abstract	3
Acknowledgments.....	5
Biographical Note.....	7
Table of Contents.....	9
List of Figures	13
List of Tables	17
Nomenclature	19
CHAPTER 1. Introduction.....	23
1.1 Motivation.....	24
1.2 Objectives.....	27
1.3 Background.....	28
1.4 Approach.....	30
CHAPTER 2. Adaptive Plate Model.....	33
2.1 Piezoelectric Fiber composites	34
2.1.1 Piezoelectricity	34
2.1.2 Linear Model of Piezoelectricity	36
2.1.3 Effective Ply Property Model.....	39
2.2 Laminate Model	41
2.2.1 Plane Stress Simplification.....	42
2.2.2 Property Rotations.....	43
2.2.3 Strain-Displacement Relations.....	45
2.2.4 Classical Laminated Plate Theory.....	46
2.2.5 Exact Solution	49
2.2.6 Rayleigh Ritz Method.....	49
2.2.7 Implementation.....	55

2.2.8	Assumed Shape Functions	57
2.2.9	Preliminary Model Validation	60
2.3	Adaptive Plate Design	61
2.4	Summary	66
CHAPTER 3.	Adaptive Plate Manufacture.....	67
3.1	Key Manufacturing Issues	67
3.2	PFC Components.....	70
3.2.1	Fibers.....	70
3.2.2	Hybrid Matrix.....	71
3.2.3	Interlaminar Electrodes.....	73
3.3	Prepreg Manufacturing Procedure.....	74
3.3.1	Mold Construction.....	75
3.3.2	Fiber Lay-Out.....	76
3.3.3	Prepreg Assembly	77
3.3.4	Compression and Staging.....	79
3.4	Adaptive Plate Manufacture	81
3.4.1	Lay-Up	81
3.4.2	Cure	82
3.4.3	Thermal Stresses	84
3.4.4	Preparation for Testing	85
3.5	Summary	86
CHAPTER 4.	Experimental Results	87
4.1	Experimental Procedures	88
4.1.1	PFC Testing.....	88
4.1.2	Adaptive Plate Testing	89
4.1.3	Current Measurements	91
4.2	PFC Characterization.....	91
4.2.1	Typical Operation	92
4.2.2	Component Property Tests.....	94
4.2.3	DUF Model Predictions for Effective Properties	98
4.2.4	Preliminary Strength Testing.....	100
4.3	Adaptive Plate Experiments.....	101
4.3.1	Bend and Twist Operating Modes.....	102
4.3.2	Passive Properties of the Adaptive Plates.....	104

4.3.3	Predicted Actuation.....	107
4.4	Unmodeled Effects	111
4.4.1	High Field Nonlinearities.....	112
4.4.2	Frequency Dependence.....	115
4.5	Evaluation of Peak Actuation Capabilities.....	120
4.6	Summary	122
CHAPTER 5. Conclusions and Recommendations.....		123
5.1	Conclusions.....	123
5.2	Recommendations.....	127
Appendix A.	Rayleigh Ritz MATLAB Code.....	129
Appendix B.	Shape Functions	147
Appendix C.	Rayleigh Ritz Plate Model Validation.....	149
Appendix D.	Noise Control Experiment.....	151
Glossary	155
References	159

List of Figures

- Figure 1-1 Piezoelectric fiber composite embedded in laminated plate structure.
- Figure 1-2 Comparison of actuation capabilities (exaggerated) between a monolithic piezoceramic and a PFC at various orientations.
- Figure 1-3 Adaptive plate manufacturing concept.
- Figure 2-1 Typical transverse strain versus electric field plot for PZT5H.
- Figure 2-2 Standard coordinates for a piezoceramic wafer and actuation strains (dashed lines).
- Figure 2-3 Typical transverse piezoceramic operating curve for PZT5H.
- Figure 2-4 PFC coordinate system and polarization vector.
- Figure 2-5 Anisotropic in-plane expansion and through-thickness contraction of a PFC.
- Figure 2-6 DUF model geometric input parameters.
- Figure 2-7 Application of plane stress assumptions to the laminate.
- Figure 2-8 Global coordinate frame of laminate.
- Figure 2-9 Representation of coordinate transformation.
- Figure 2-10 Linear strain continuity assumption—strain field in cross-section is described by displacement of plane section to dashed line.
- Figure 2-11 Force and moment convention and laminate geometry.
- Figure 2-12 Areas representing the principal and complimentary electrical and mechanical energy.
- Figure 2-13 8-point quadrature example.

- Figure 2-14 Method for the elimination of spatial dependence from area integrals.
- Figure 2-15 Five cantilevered plate shape functions; Upper: T1, T2, C1; Lower: B1, B2.
- Figure 2-16 Comparison of deflections for cantilevered plates with two PFC actuators in two modes of operation (end view and planform view).
- Figure 2-17 Comparison of predicted twist for various laminates.
- Figure 2-18 Adaptive plate with electrode connections.
- Figure 2-19 Optimal fiber spacing for twist actuation of plate.
- Figure 3-1 Electric field distribution in quarter model of fiber and matrix, $x_2=0.9$, $x_3=0.9$, $\epsilon_f/\epsilon_m=10$.
- Figure 3-2 Etched electrode patterns with end flaps for upper (light) and lower (dark) layers.
- Figure 3-3 Mold for PFC prepreg assembly.
- Figure 3-4 Photograph of PZT fiber bundles prepared for transfer to mold.
- Figure 3-5 Completed mold assembly containing fibers ($x_2=0.5$).
- Figure 3-6 Matrix material being added to mold assembly containing fibers.
- Figure 3-7 Vacuum bag assembly for degassing matrix.
- Figure 3-8 Mold containing fibers, matrix, and electrodes.
- Figure 3-9 Prepreg compression and staging assembly.
- Figure 3-10 Conformable PFC prepreg.
- Figure 3-11 Adaptive plate laminae.
- Figure 3-12 Cure assembly cross section and top view with electrode flaps extended.
- Figure 3-13 Cure plate assembly in autoclave.

- Figure 3-14 Photomicrograph of adaptive plate edge (50x).
- Figure 4-1 Experimental set-up for adaptive plate testing.
- Figure 4-2 Typical operating curves for a free PFC in longitudinal and transverse directions at 1 Hz: a. low field, b. high field.
- Figure 4-3 PFC stiffness tests: a. bending, b. extension.
- Figure 4-4 Tensile strength tests of AS4/3501-6 laminate coupons, [15/0/-15]_S and [60/0/-60]_S.
- Figure 4-5 Bend and twist operation of adaptive plate 2, 0.01 Hz.
- Figure 4-6 Transfer function data for plate 1 from voltage input to the +45° ply to bend and twist rate.
- Figure 4-7 Transfer function data for plate 2 from voltage input to the +45° ply to bend and twist rate.
- Figure 4-8 Comparison of data and model predictions for the bending and twisting of adaptive plate 1.
- Figure 4-9 Comparison of data and model for single ply actuation in adaptive plate 2.
- Figure 4-10 Comparison of data and model for in-phase operation of adaptive plate 2.
- Figure 4-11 Comparison of data and model for out-of-phase operation of adaptive plate 2.
- Figure 4-12 High field tests of a free PFC at 0.01 Hz.
- Figure 4-13 High field tests of adaptive plate 1.
- Figure 4-14 Frequency dependence of maximum free strain for a PFC.
- Figure 4-15 Polarization and butterfly curves for a free PFC: a. 0.001 Hz, b. 0.01 Hz, c. 0.1 Hz.
- Figure 4-16 Polarization and butterfly curves for a free PFC: a. 1 Hz, b. 10 Hz, c. 100 Hz.

- Figure 4-17 Transfer function from applied voltage to current for an active ply and model.
- Figure A-1 M-file hierarchy in MATLAB adaptive plate model.
- Figure D-1 Coordinates for sound power level calculations.
- Figure D-2 Preliminary design for experimental set-up.

List of Tables

Table 2-1	In-Plane Polynomial Shape Functions.
Table 2-2	Out-of-Plane Polynomial Shape Functions.
Table 2-3	Geometric Boundary Conditions Along an Edge ($x=0$).
Table 2-4	Comparison of Models and Data for Symmetric Laminates.
Table 2-5	Optimization Input Properties.
Table 3-1	PZT5H Properties.
Table 3-2	Properties of Epon 9405/Epi-Cure 9470 Resin System.
Table 3-3	Coefficients of Thermal Expansion for the Adaptive Plate Laminae.
Table 4-1	Component Property Evaluation Strategy.
Table 4-2	PFC Stiffness Data (GPa) and Predicted Fiber Compliance Relative to Bulk.
Table 4-3	Matrix Dielectric Measurements.
Table 4-4	Comparison of Predicted and Experimental Relative Dielectric.
Table 4-5	Summary of Inputs and Outputs of DUF Model for Two Adaptive Plates.
Table 4-6	Material Properties of Graphite/Epoxy and Polyester Plies.
Table 4-7	Comparison of Predicted and Experimental Natural Frequencies (Hz).
Table 4-8	Perfect Composite Properties.

- Table 4-9** **Comparison of Actuation Capabilities for Current PFC and Perfect Composite.**
- Table C-1** **Comparison of Data and Model Predictions for Free Aluminum Plate.**
- Table C-2** **Comparison of Data and Model predictions for Cantilevered Aluminum Plate.**

Nomenclature

a	Length of plate
b	Width of plate
c^E	Stiffness
c	Wave speed
d	Fiber diameter
d	Piezoelectric strain constant
e	Piezoelectric stress constant
f	External forces
j	Imaginary number
$\hat{\mathbf{k}}$	Unit vector in 3-direction
k	Wavenumber
k₃₁	Transverse piezoelectric coupling coefficient
l	Sound field position
l₀	Position on plate surface
l	Sound field distance
$\hat{\mathbf{n}}$	Unit normal vector
n	Number of plies
n_A	Number of actuators
n_q	Number of electrodes
p	Eigenvectors representing mode shapes in generalized coordinates
q	Charge on electrodes
r	Generalized displacement coordinates
s^E	Compliance (constant-field)
t_p	Thickness of PFC
t	Time
u	Displacement vector
u_n	Normal surface velocity
u,v,w	Displacements
v	Generalized potential coordinates

w_f	Space between fibers
w_i	Gauss weights
\mathbf{x}	Position vector
x, y, z	Laminate axes
x_2	Width line fraction of fibers
x_3	Through-thickness line fraction of fibers
x_i, y_i	Gauss points
z_1, z_2	Tip displacements
A_S	Surface area
$\mathbf{A}, \mathbf{B}, \mathbf{D}$	Laminate stiffness coefficients
\mathbf{B}_f	External force matrix
\mathbf{B}_q	External charge coupling matrix
\mathbf{C}	Capacitance matrix
\mathbf{D}	Electric displacement
\mathbf{E}	Electric field
E_c	Coercive electric field
E_L	Longitudinal Young's modulus
E_T	Transverse Young's modulus
G_{LT}	Shear modulus
G_ω	Frequency domain Green's function
K	Kinetic energy
\mathbf{K}	Generalized stiffness matrix
L_u	Differential operator matrix (displacement)
L_ϕ	Differential operator matrix (potential)
L	Free length of plate to laser sensors
L_0	Average sound field distance
\mathbf{M}	Generalized mass matrix
\mathbf{M}, \mathbf{N}	Moment and force stress resultants
$\mathbf{M}^A, \mathbf{N}^A$	Actuator induced moment and force resultants
\mathbf{P}	Polarization
P	Sound pressure
\mathbf{R}_E	Rotation matrix (electrical)
\mathbf{R}_S	Rotation matrix (strain)
\mathbf{R}_T	Rotation matrix (stress)
\mathbf{S}	Strain

S^0	Centerline strain
T	Stress
U_1^E	Principal electrical potential energy
U_2^E	Complimentary electrical potential energy
U_1^M	Principal mechanical potential energy
U_2^M	Complimentary mechanical potential energy
U_p	Energy density
V	Volume
W	Distance between laser sensors
W_1^E	Principal electrical work
W_1^M	Principal mechanical work
α	Coefficient of thermal expansion
ϵ^S	Dielectric permittivity (clamped)
ϵ^T	Dielectric permittivity (free)
ϵ_0	Permittivity of free space
ϵ_m	Matrix dielectric
κ	Curvature
ν_{LT}	Poisson ratio
θ	Ply angle
ρ	Density
ϕ	Electrical potential
ω	Frequency
Ψ_r	Displacement shapes
Ψ_v	Potential shapes
Δ_T	Temperature change
Λ	Eigenvalues
Λ_1, Λ_2	Maximum free strains
Θ	Electromechanical coupling matrix
$(\cdot)_A$	Actuator or active
$(\cdot)^f$	Property of fibers
$(\cdot)^m$	Property of matrix
$(\cdot)^D$	Values measured at constant electric displacement (e.g. open circuit)

- (·)^E Values measured at constant electrical field (e.g. short circuit)
- (·)^S Values measured at constant strain (e.g. clamped)
- (·)^T Values measured at constant stress (e.g. free strain)
- (·)^{*} Reduced plane stress constants
- (·)_t Matrix transpose
- (·) Lamina coordinates
- (·) Unit vector

CHAPTER 1

Introduction

Engineering designs often need to include a controlled means for manipulating the geometry or mechanical properties of structures in order to meet variations in external conditions or to reduce unwanted disturbances. For instance, the shape of a structure can be modified to achieve some desired performance. An example of this is altering the geometry of an airfoil to increase or decrease lift. A mechanical property such as the stiffness may be modified to change the dynamic characteristics of a structure under certain conditions. In other applications, structural vibrations which create undesirable acoustic noise or disturb sensitive equipment may be reduced through mechanical cancellation or some form of isolation or damping.

Adaptive structures possess integrated actuators which enable controlled changes in the geometry and physical properties of the structures [Wada *et al*, 1989]. Integration of the actuators within the structure allows for a more efficient means of adapting. The adaptive structure is designed as a complete package with advantages in reduced size, weight, and mechanical complexity in comparison with a comparable passive structure. Only a command signal is required to achieve the desired structural modifications.

Smart or active materials are a common form of actuator that can be integrated easily into an adaptive structure. In general, smart materials possess a mechanical functionality which is useful for both actuating and sensing [Newnham and Ruschau, 1993]. In an active material, the mechanical response is controlled using an applied electrical, magnetic, or thermal variation. In many cases, this form of actuator offers the same capabilities as do more complex actuation mechanisms such as electromagnetic coils or hydraulics.

Piezoelectric ceramics are one type of active material that exhibits a strong electromechanical coupling. In short, a piezoelectric material produces a charge when

mechanically strained, and conversely, produces a mechanical strain when a charge is applied. Piezoceramics can be used as structural actuators by controlling the charge or electric field developed across the thickness of a thin, planar-type geometry of ceramic. This form is referred to as a monolithic piezoceramic or a piezo patch.

1.1 MOTIVATION

Monolithic piezoceramic actuators and other similar materials such as electrostrictors have inherent performance limitations resulting from the extremely brittle nature of the ceramic. Great care must be taken during the manufacture of piezoceramic actuators, the application to structures, and the operation of the active structure. The brittleness makes the processing of piezoceramic wafers costly and can significantly limit the size and shape of available actuators. These wafers must then be bonded to the surface of the planar structure. The wafers could also be embedded within a laminated plate-type structure [Crawley and de Luis, 1987]; however, this manufacturing process is difficult and tedious. This is because the host composite plies must be cut to fit around actuators, and electrical connections, high cure pressures, and thermal stresses threaten to fracture the delicate wafers. In addition, the discontinuous nature of the embedded ceramics may lead to reduced structural integrity in these laminates.

A fairly recent alternative to the monolithic piezoceramic is the piezoelectric fiber composite (PFC). This particular composite form is referred to as a 1-3 composite with transversely aligned fibers since the fibers have connectivity in only one direction and the matrix is continuous in all three directions [Smith, 1989]. The PFC concept is illustrated in Figure 1-1. The combination of piezoceramic fibers and a polymer matrix results in several attractive advantages for PFC's over the monolithic actuator materials. The compliant matrix protects the piezoceramic fibers, reducing the brittleness in the actuator. Thus, PFC's are conformable and can be used in structures with curvature. The matrix also enables load sharing between the fibers which benefits the structural integrity of the actuator. The stiff piezoelectric fibers lay in the plane of the structure for efficient transfer of forces from the actuator.

PFC's are easily embedded in composite laminates and can be made in large sizes. The conductive surface of the electrode layers delivers the electric field to the piezoelectric fibers while the polymer film backing electrically insulates the rest of the structure.

A monolithic piezoceramic actuator is transversely isotropic, developing equal strains in every in-plane direction. In contrast, PFC's are anisotropic actuators, which enable larger strains along the fibers than in the direction perpendicular to them. While a

monolithic actuator can only expand or contract uniformly, a PFC can preferentially expand

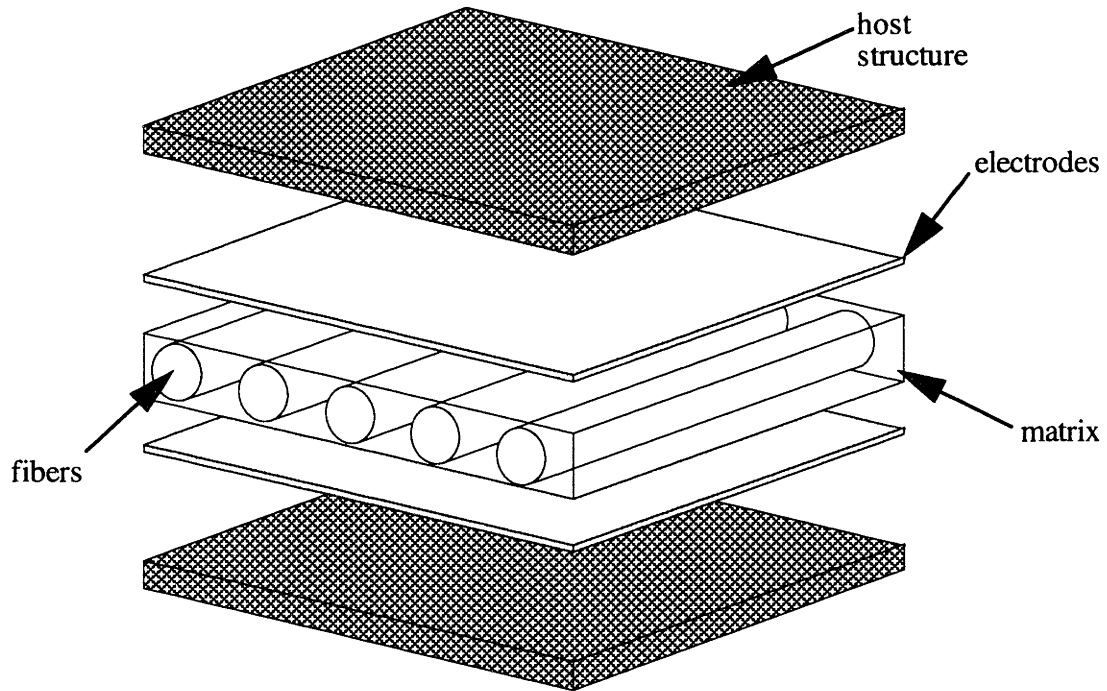


Figure 1-1. Piezoelectric fiber composite embedded in laminated plate structure.

or contract in a certain direction. Thus a PFC actuator can induce shear strains and stresses in a structure. This piezoelectric free-strain anisotropy along with the stiffness anisotropy results in a tailorable actuator which can be oriented to control specific modes within a structure. For example, consider the actuation capabilities of an unconstrained piezoceramic wafer. The actuator either expands or contracts, to an equal extent, in both in-plane directions, as shown in Figure 1-2a. Figure 1-2b shows some actuation possibilities for an anisotropic PFC actuator, with the anisotropy somewhat exaggerated.

Fibers in a PFC actuator can be oriented to induce extension in either the 0° or 90° direction, or the fibers can be rotated to an intermediate angle to induce shear deformation. It is the shearing capability that makes the PFC so attractive as an actuator. Shear forces are a primary means of directly inducing twist in structures.

PFC's can be manufactured in a prepreg tape form in which a special epoxy matrix is able to remain in an uncured, flexible state during the structural integration process. Typical structural composites are also manufactured in a prepreg tape. This form offers the advantage of greater conformability for the active ply. All plies in the laminate can then be cocured; i.e. they can be cured simultaneously to complete the manufacture of the adaptive structure.

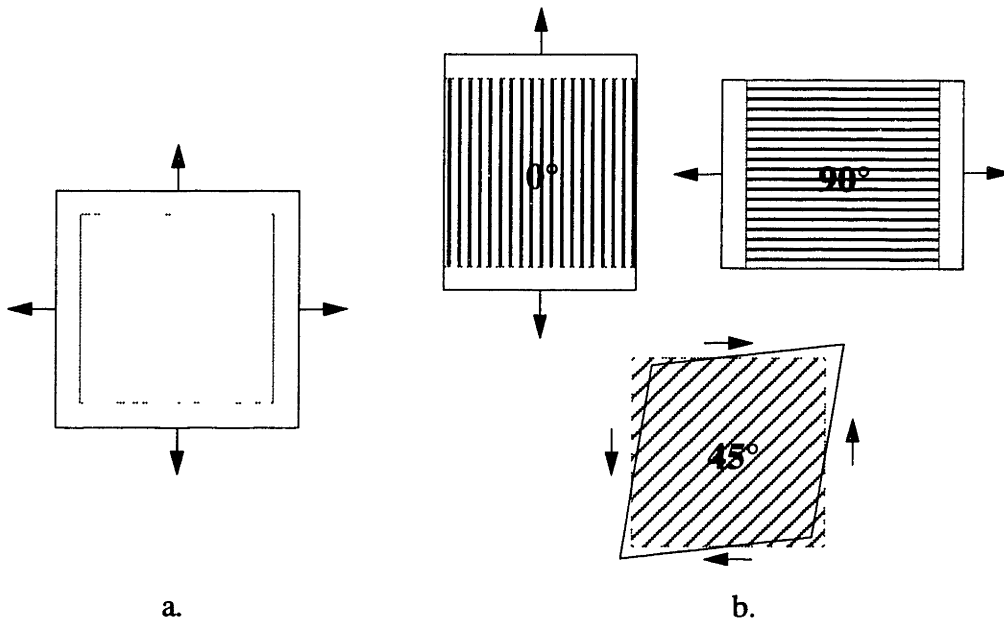


Figure 1-2. Comparison of actuation capabilities (exaggerated) between a monolithic piezoceramic and a PFC at various orientations.

PFC's also lend themselves to highly distributed control applications. The actuators can be widely spread throughout a structure, with electrodes divided into discrete sections. Local feedback processing electronics may eventually be embedded along with PFC's to form an intelligent structure. The embedded electronics [Warkentin *et al*, 1992], along with the actuators and sensors, will form local controllers which comprise the lower level of a hierarchical control system [Hall *et al*, 1991] envisioned for intelligent structures. These structures will greatly reduce the need for external processing hardware and driving amplifiers.

Several large scale applications have been investigated for PFC actuators. PFC's may offer performance improvements over piezoceramic wafers that have demonstrated effectiveness in active structural control in several previous studies. The shape and stiffness properties of a fixed-wing aircraft model were controlled to extend its flutter boundary using multiple piezoceramic actuators bonded to a composite main spar [Lin *et al*, 1993]. PFC actuators have been studied as a means of improving the performance of wing shape control applications [Ehlers and Weissnar, 1992]. In a similar aeroelastic application, piezoelectric actuators have been used for helicopter rotor blade control. Studies on the higher harmonic control of rotor blades [Spangler and Hall, 1990] suggest performance enhancements through the reduction of blade vortex interaction. Changing the lift characteristics of a blade, either through an integral change in angle of attack of the blade or a control surface, can enable the blade to maneuver around the wake from the previous

blade. Monolithic piezoceramics have been investigated to actuate a trailing edge flap [Prechtel, 1994] and to directly twist the blades using specialized piezoelectric attachment techniques [Chen and Chopra, 1995, Barrett, 1990]. PFC's are being investigated as a means of inducing twist directly in the blade or to actuate a trailing edge flap in order to control vibrations. Other expected advantages of the blade control include reduced fatigue and acoustic noise levels.

In the area of acoustics, several studies have investigated piezoceramics for controlling noise transmission through structures and sound radiation from structures. Surface mounted piezoceramic actuators have been successfully used to control sound transmission through rectangular plates [Clark and Fuller, 1992f]. Piezoceramic wafers have been bonded to large scale cylinders to control the sound reaching the interior [Lester and Silcox, 1992], simulating an aircraft fuselage in which external turbofan noise creates disturbances in the cabin. PFC's may be embedded directly within the aircraft fuselage to reduce the transmission of structural vibrations into the cabin. Similarly, PFC's can be embedded within a submarine hull to attenuate outgoing sound radiation or to absorb incoming sonar [Newnham and Ruschau, 1993].

1.2 OBJECTIVES

The objectives of this research are to develop the modeling and manufacturing capabilities necessary to design and produce adaptive structures incorporating PFC actuators. Once the composite actuator has been fully characterized and adequate models have been developed, adaptive structures can be designed for many applications. Technologies must also be developed to manufacture PFC prepregs, and then to embed these prepregs in a laminated composite host structure. With production capabilities established, an experimental demonstration of the independent control of bending and twisting in a cantilevered, composite plate can be performed.

Future projects will build on the current work, leading toward demonstrations of actuator effectiveness in specific applications. Ultimately, the development of PFC's and embedded processing hardware will lead to large-scale, intelligent structures with highly distributed actuators and sensors.

1.3 BACKGROUND

Significant background research contributed to this work on PFC's. Research has led to a better understanding of piezoceramics, especially with regard to modeling. Jaffe *et al* provided the foundation for the modeling of piezoceramics [1971]. More recently, attempts have been made to model the nonlinear properties [Chan and Hagood, 1994, Anderson and Crawley, 1993]. Hagood and others developed the modeling theories for describing the complete electromechanical system [1990]. In addition, modeling capabilities have been developed for adaptive plates which utilize surface mounted piezoceramic wafers [Crawley and Lazarus, 1989]. The Rayleigh Ritz modeling techniques used in their research provided a foundation for the development of the adaptive plate model used in this research.

Piezocomposites were developed to enhance the capabilities of piezoceramic-based sensing devices. In particular, 1-3 composites, with fibers oriented through the thickness, were developed for hydrophone sensors and ultrasonic transducers [Newnham *et al*, 1980]. For hydrophones, researchers created a sensor material with low density and low acoustic impedance, while taking advantage of the direct piezoelectric effect along the fibers. The composite form of the sensor enabled this tailoring, resulting in improved sensing capabilities as compared with monolithic piezoceramics. Similarly, ultrasonic transducers for medical imaging are designed using piezocomposites which substantially improve imaging capabilities [Smith, 1989]. The composite allows for tailoring of the material properties to adjust electrical impedance, improve the electromechanical coupling, closely match the acoustic impedance of human tissue, and shape the transducer to focus the beam.

Composites accentuate the positive characteristics of piezoceramics and reduce the drawbacks. In these examples, the matrix enhances the mechanical properties of the composite while maintaining the piezoelectric properties in some desired direction. Tailoring capabilities also benefit the designs of actuators and sensors for specific applications.

Additional research on PZT/polymer composites has been focusing on improved methods for manufacturing fibers of a higher quality and better performance [Yoshikawa *et al*, 1992]. Current fibers are produced in 9 cm lengths with a 130 μm diameter [Parish, 1994]. Improvements in manufacturing using sol-gel processing will enable smaller diameters and greater lengths. In addition, the quality of the ceramic may be improved through a reduction in the grain size, which increases the strength of the fibers. Other researchers have developed relic processing technologies for manufacturing PZT fiber/polymer composites [Waller and Safari, 1992].

Several other types of active materials have also been investigated for structural actuation. Electrostrictive materials offer the advantages of high stiffness and low hysteresis, but lack the actuation capabilities of piezoceramics [Fripp, 1995]. Magnetostrictive materials offer high actuation levels but require more complicated supporting structures to provide the driving magnetic field to the material [Butler, 1988]. Shape memory alloys enable very large strains and have been investigated in the form of embedded fibers in a laminated plate [Rogers *et al*, 1989]. Their drawbacks are the necessary heating elements and the associated low bandwidth problem. Similarly, shape memory ceramics, which are controlled by an electric field, offer high strains but a relatively low bandwidth in their current form [Ghandi, 1995].

Piezoelectric fiber composites are not the sole form of structural, anisotropic actuators under investigation. Barrett has developed Directionally Applied Piezoceramics (DAP) which utilize specialized attachment techniques for bonding monolithic ceramic wafers to structures [1992]. Other researchers have manufactured piezoceramic/polymer composites using thin slices of a PZT plate embedded in an epoxy matrix [Wetherhold and Panthalingal, 1993]. Special electrode patterns can also be used on monolithic piezoceramics to shift the polarization into the plane of the wafer [Hagood *et al*, 1993]. This creates anisotropy because of the stronger piezoelectric effect along the poling direction. Another type of anisotropic piezoelectric material is polyvinylidene difluoride (PVDF) which is a polymer. It has been used primarily as a sensory material because of its low stiffness, though it has been investigated for some structural actuation applications [Ehlers and Weisshaar, 1992, Charon and Baier, 1993].

Hagood and Bent established the groundwork for the current research [Hagood and Bent, 1993] on PFC's. Models were developed to characterize the effective mechanical, electrical, and coupling properties of PFC actuators. In particular, a Discretized Uniform Fields (DUF) model was used for modeling the active plies in this work. Manufacturing techniques were also developed to build small PFC's for characterization tests and model validation. This experience was used to perform design studies of the actuator itself and to illuminate key manufacturing and design issues. Results of hybrid matrix studies were also used in the development of the manufacturing process. In addition, the concept of anisotropic actuation was thoroughly analyzed and induced twist in an isotropic host structure was experimentally demonstrated [Bent *et al*, 1995]. This project builds on the knowledge and experience gained from previous work.

1.4 APPROACH

This thesis details both the modeling and the manufacturing of adaptive plates which contain embedded PFC actuators. In order to characterize the response of adaptive plates incorporating PFC actuators, an adaptive plate model was developed. The preexisting DUF model provided the effective active ply properties, once the component material properties were established. A Rayleigh Ritz plate model was developed which incorporates multiple, embedded, anisotropic actuators or active plies. In addition to helping to characterize the actuator system, the models serve as design tools for optimizing the PFC manufacturing process and fabricating adaptive plates for specific applications.

A PFC prepreg manufacturing process was developed to enable the fabrication of large scale, active prepreg layers to be embedded between structural host plies in a laminated plate. The general concept for PFC manufacturing is outlined in Figure 1-3. The laminate is assembled, or laid up, with the plies in a flexible prepreg form. Then the entire laminate is cured, integrating the plies into a composite structure. The prepreg manufacturing process was developed using current prepreg tape manufacturing processes, such as the Hercules graphite/epoxy process [Wareham, 1993], as a basis. Additional

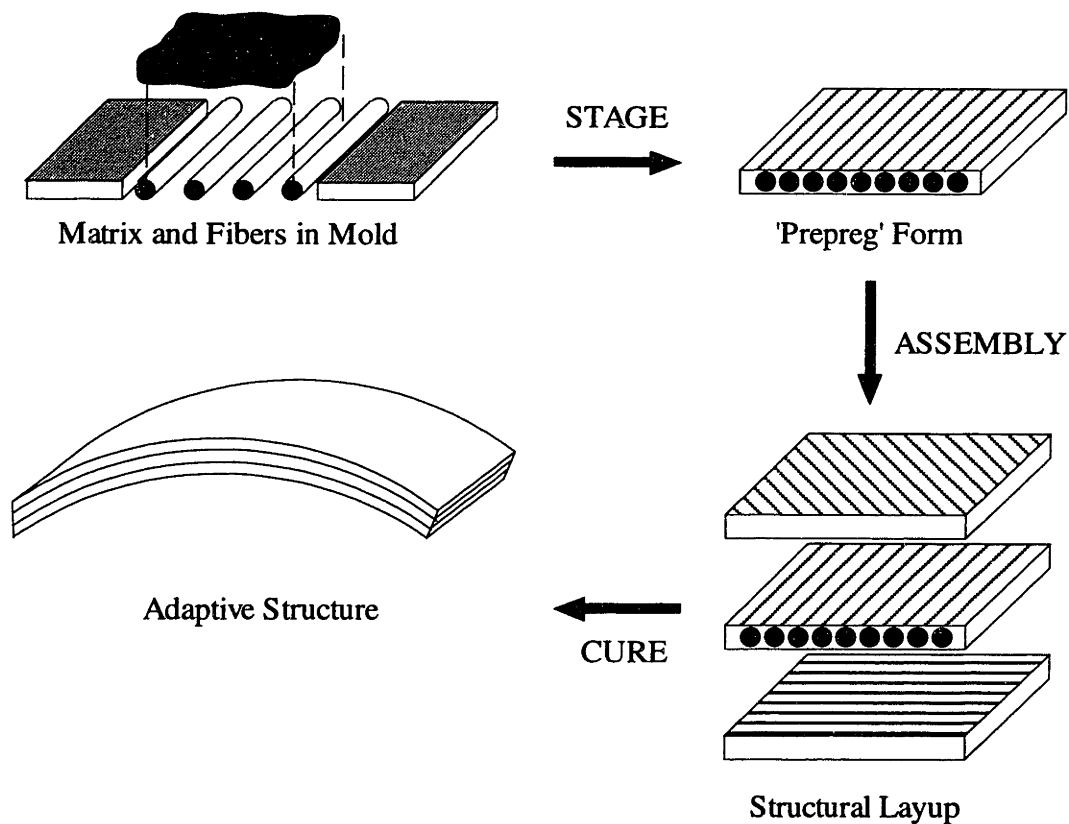


Figure 1-3. Adaptive plate manufacturing concept.

considerations were necessary because of the brittle nature of the ceramic fibers. The problem of manufacturing prepregs using discontinuous, brittle fibers has been previously studied for boron composites [Kane, 1967]. The composition of the special hybrid matrix, which further complicates the manufacturing process, was selected to meet both dielectric and viscosity requirements.

A preliminary investigation into acoustic noise control has been initiated. A model of the sound radiated from a vibrating plate is presented. In addition, a preliminary design for an acoustics experiment intended to actively control sound radiated from a composite plate has been established. The experiment will attempt to improve upon previous work in which monolithic piezoceramics were bonded to the surface of various plate structures [Clark and Fuller, 1990].

The chapters of this thesis are organized in the same order as described in the general approach. Chapter 2 begins with background theory on piezoelectricity, leading up to the linear piezoelectric constitutive relations. Then the Discretized Uniform Fields (DUF) model used for predicting the effective properties of the active composite ply is described. Details of the anisotropy and the remaining PFC modeling concepts complete the lamina level modeling. Next, the properties of the active ply are incorporated into the laminate model of the adaptive plate. Classical Laminated Plate Theory (CLPT) is introduced and used in the Rayleigh Ritz energy analysis. Solutions to the static and dynamic, forced and unforced plate deflection problems are given, along with assumed shape functions used in the comparisons with experiments later in this thesis. A preliminary model validation for model predicted natural frequencies and mode shapes of various composite plates is discussed. The modeling is concluded with a discussion of adaptive plate design considerations. The ramifications of the inherent anisotropy of PFC's are further examined. Finally, an adaptive plate is designed with the goal of maximizing twist using two active plies.

The manufacturing chapter, Chapter 3, begins with a description of the key manufacturing issues followed by an overview of all of the components of PFC actuators. The preparation of the hybrid matrix is also included in the component discussion. Next, the prepreg manufacturing process is fully explained, from the integration of fibers, matrix, and electrodes, through the degassing, compression, and staging, and resulting in a finished prepreg. Then the assembly of active and structural prepreg plies and the cure of the resulting adaptive plate are detailed, along with preparations for testing. Photographs and drawings are used to support the descriptions. Using the procedures described, two adaptive plates were produced. Each contains two PFC plies and three graphite/epoxy structural plies.

The experimental chapter, Chapter 4, includes characterization studies of PFC actuators in addition to tests of the manufactured adaptive plates. The characterization studies illustrate the typical properties of PFC actuators. In addition, they provide data on the mechanical and electrical properties of the component materials used in the active ply model. The data are used to establish upper and lower bounds on the effective properties used in the adaptive plate model. Experimental data from manufactured adaptive plates are used to demonstrate the independent control of bending and twisting. The performance of the adaptive plates is next compared with model predictions over a range of frequencies. Unmodeled nonlinearities are then discussed and further data is provided in support of the explanations. In addition, the performance of the model and the actuators are discussed in relation to a hypothetical perfect composite actuator.

In the final chapter, Chapter 5, conclusions are drawn and recommendations for future improvements are suggested. Applications currently in the design stages will also be discussed. Several appendices complete the thesis with additional details of the implementation and validation of the adaptive plate model as well as the preliminary design for an acoustics experiment.

CHAPTER 2

Adaptive Plate Model

The model for the adaptive plate begins on the microscopic level with the properties of the constituent materials which make up the composite laminae, and builds toward a complete laminate model. First, an overview of piezoelectricity is provided on a microscopic level. Then, the macroscopic effects are discussed for piezoceramic actuators and sensors. A linear model is used to describe the electromechanical coupling in the form of the constitutive relations. Unmodeled nonlinear aspects of piezoelectric materials are also introduced. Next, the distinctions between monolithic piezoceramics and PFC's are pointed out, with an emphasis on the in-plane anisotropy of PFC's.

A model is presented for determining the effective properties are needed to set manufacturing goals for the geometry of the actuator, and for a given design geometry, to evaluate test articles. In addition, the full range of material properties can be estimated from the geometry of a PFC lamina using the composite model. This provides lamina information for the purpose of modeling an adaptive laminate. These composite modeling needs are fulfilled using the Discretized Uniform Fields model of the PFC.

The ply properties of the various laminae comprising the plate are combined to form laminate properties using Classical Laminated Plate Theory. A Rayleigh Ritz energy formulation provides static, dynamic, and forced solutions for the adaptive plate for any standard plate geometric boundary conditions. The boundary conditions are enforced through the selection of assumed shape functions for the deformation of the plate. Model predictions for passive plate solutions are compared with referenced experimental data for validation purposes. Finally, the DUF and Rayleigh Ritz models are used to design an adaptive plate with the goal of maximizing induced twist using PFC plies.

2.1 PIEZOELECTRIC FIBER COMPOSITES

This section provides a brief background on the theory of piezoelectricity. The piezoelectric phenomenon is explained. This discussion leads to the introduction of the piezoelectric fiber composite actuator and its properties along with a linear model for piezoelectricity. Then the properties and characteristics of monolithic piezoceramic actuators are presented. This will complete the modeling of the individual laminae that compose the adaptive plate.

2.1.1 Piezoelectricity

Piezoelectricity is a phenomenon exhibited in certain crystalline materials defined by an inherent electromechanical coupling [Jaffe *et al*, 1971]. The direct piezoelectric effect is the development of an electrical charge proportional to an applied mechanical stress. The converse effect also holds, where an applied voltage results in a mechanical strain. The piezoelectric effect arises from an asymmetry in the unit cell of the crystal lattice. The absence of a center of symmetry results in a net polarization within the crystal which is distributed throughout the volume. This is the defining feature of piezoelectric materials, differentiating them from other types of crystalline materials. Many piezoelectric materials are also ferroelectric. Ferroelectric materials transform to a symmetric, nonpiezoelectric phase above a certain transition temperature known as the Curie point.

Piezoelectric materials were originally thought to be useful only in single crystal form, where all cells in the lattice structure are aligned. This uniformity of alignment enables the polarization in the cells to add so that the net piezoelectric effect of the material is the sum of the individual cell contributions. In contrast, polycrystalline materials have multiple, randomly oriented grains. This results in a zero net polarization. However, the discovery of high dielectric, ferroelectric ceramics with a Perovskite crystal structure enabled a net polarization to be attained. A *poling* process was developed which aligns the dipoles within the multiple grains in the material. After applying a strong electric field at somewhat elevated temperatures, the ferroelectric material attains a strong net polarization. Thus ferroelectric ceramics can be used in place of single crystals, which are more difficult to manufacture.

The poling process is accomplished at electric field levels greater than the specified coercive field of the particular material. A large portion of the dipoles remain aligned once the field is removed, resulting in a remanent polarization. The degree to which a piezoceramic is polarized depends on the poling field, temperature, and time that the field is maintained. Elevated temperatures allow dipoles to align more efficiently during poling;

however, temperatures above the Curie point effectively depole the piezoceramic because of the ferroelectric-paraelectric transition.

The level of polarization achieved directly effects the magnitude of the electromechanical coupling exhibited. Temperature also effects the coupling to widely varying degrees for different compositions [Piezo Systems, 1993]. A poled piezoceramic forms a surface charge when strained. This charge can be collected on conductive electrodes and measured in a sensor arrangement. Conversely, a piezoceramic actuator creates mechanical strain resulting from an applied electric field. The applied field commands the mechanical contraction or expansion of the piezoelectric material.

Figure 2-1 shows a typical “butterfly” curve for PZT5H. A sinusoidal electric field was applied to a piezoceramic wafer and the resulting mechanical strain was measured on the surface of the material. As the field is increased, opposing the remanent polarization, the strain rate suddenly changes sign. This characteristic transition occurs at the coercive field (± 600 V/mm) and illustrates the repoling of the piezoceramic — the polarization is reversed. The Another important feature of the curve is the nearly linear behavior at low field levels. This permits the use of linear models for piezoelectricity which will be described in the next section. There is also a limit to the level of strain the material can reach — the point at which an increase in field no longer increases the strain, called

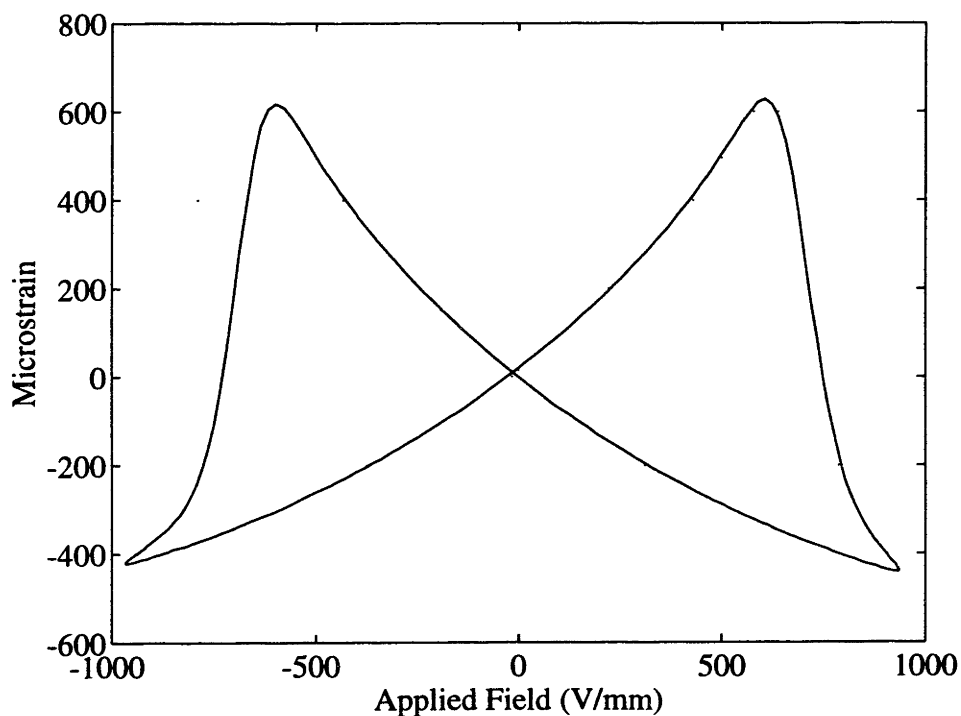


Figure 2-1. Typical transverse strain versus electric field plot for PZT5H [Chan and Hagood, 1994].

saturation. Saturation is evident at the lower corners of the butterfly curve in Figure 2-1, where the magnitude of the slope is decreasing as the applied field approaches ± 1000 V/mm.

For actuating or sensing strains within the plane of the plate or shell-like structures, piezoceramics are often operated in the transverse mode. Figure 2-2 shows the standard coordinate system used to refer to piezoceramics. In the transverse mode, the 3-axis is aligned with the poling direction, \mathbf{P} . Although the primary strains resulting from the piezoelectric effect are oriented in the 3-direction, the transverse strains resulting from a Poisson effect are the most useful for structural actuation and sensing in planar structures. Note that the electric field, \mathbf{E} , is applied through the thickness. An applied field in the poling direction results in an in-plane contraction and an expansion through the thickness, as shown with the dashed lines in the figure.

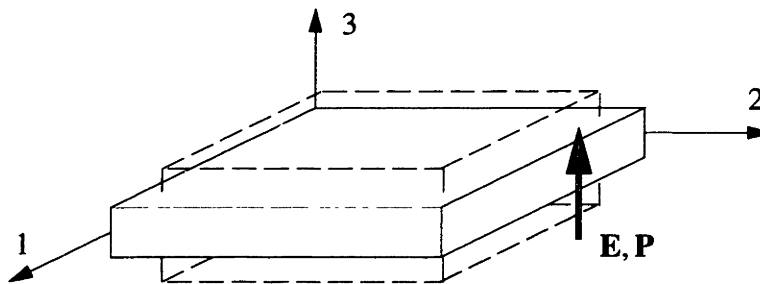


Fig. 2-2. Standard coordinates for a piezoceramic wafer and actuation strains (dashed lines).

2.1.2 Linear Model of Piezoelectricity

Once poled, piezoceramic actuators are generally operated at relatively low electric field levels. This prevents repolarization and takes advantage of the nearly linear strain field relationship. Figure 2-3 shows a typical operating curve for a piezoceramic at slightly higher field levels where hysteretic effects are more evident. An applied electric field aligned with the polarization results in a negative transverse strain in the material, while a field opposing the polarization results in a positive transverse strain.

Modeling of piezoceramic actuators must begin at the lamina level. Before describing the linear model for piezoelectricity, a reference frame must be established for a PFC. In the local coordinate system of the material, the 3-axis is chosen to align with the net polarization vector as shown in Figure 2-4. The 1-axis is along the fibers and the 2-axis is orthogonal to the fibers in the plane. The in-plane axes may be oriented arbitrarily in monolithic piezoceramics. Piezoceramics are transversely isotropic materials in which the net polarization lies along the axis of symmetry (3-axis). It is the electromechanical coupling inherent in the material that creates this anisotropy. The composite form of the

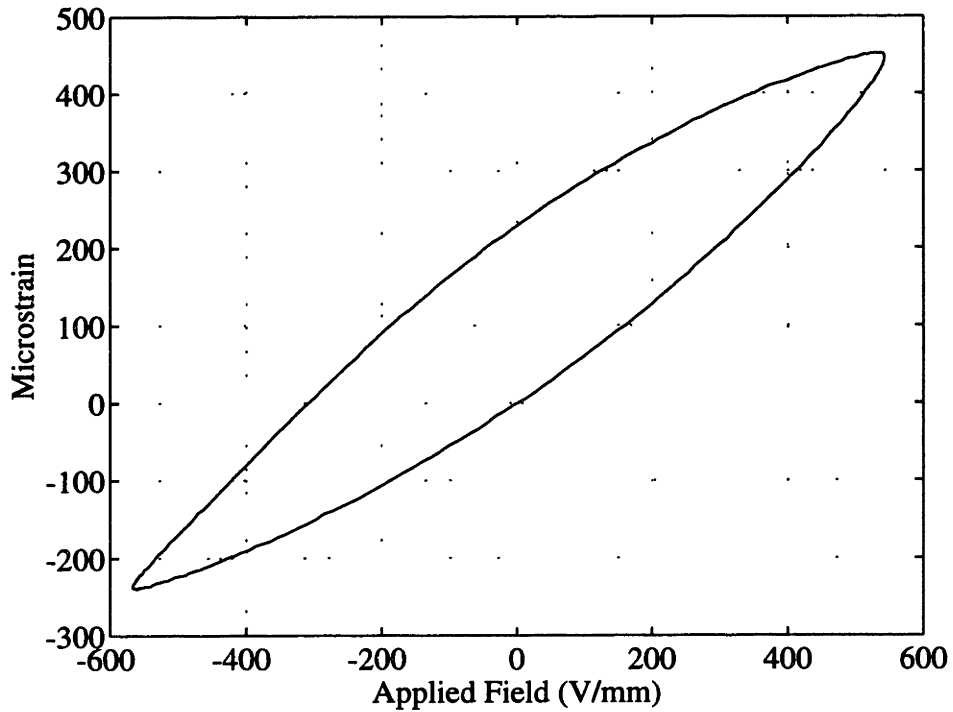


Figure 2-3. Typical transverse piezoceramic operating curve for PZT5H [Chan and Hagood, 1994].

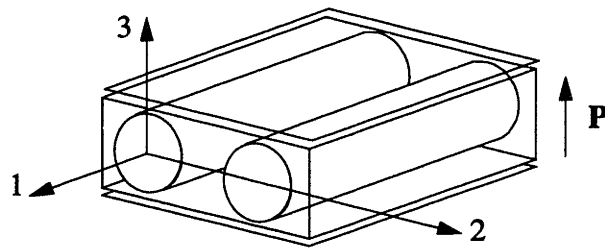


Fig. 2-4. PFC coordinate system and polarization vector.

piezoceramic introduces additional anisotropy which will be discussed in terms of the piezoelectric constitutive relations.

A linear model is used to relate the mechanical and electrical field variables through a matrix of coupling properties which are material specific. The following is a general form of the piezoelectric constitutive relations [IEEE Std., 1978]:

$$\begin{bmatrix} \mathbf{D} \\ \mathbf{S} \end{bmatrix} = \begin{bmatrix} \boldsymbol{\varepsilon}^T & \mathbf{d} \\ \mathbf{d}_t & \mathbf{s}^E \end{bmatrix} \begin{bmatrix} \mathbf{E} \\ \mathbf{T} \end{bmatrix} \quad (1)$$

Equation (1) uses Voigt's notation for the stress, \mathbf{T} , and strain, \mathbf{S} , vectors, which are defined:

$$\mathbf{S} = \begin{bmatrix} S_{11} \\ S_{22} \\ S_{33} \\ 2S_{23} \\ 2S_{13} \\ 2S_{12} \end{bmatrix} = \begin{bmatrix} S_1 \\ S_2 \\ S_3 \\ S_4 \\ S_5 \\ S_6 \end{bmatrix} \quad \text{and} \quad \mathbf{T} = \begin{bmatrix} T_{11} \\ T_{22} \\ T_{33} \\ T_{23} \\ T_{13} \\ T_{12} \end{bmatrix} = \begin{bmatrix} T_1 \\ T_2 \\ T_3 \\ T_4 \\ T_5 \\ T_6 \end{bmatrix} \quad (2)$$

The other variables are the electric field, \mathbf{E} , and electrical displacement, \mathbf{D} , which is a measure of the surface charge density. The square matrix is the matrix of material properties. The compliance coefficients, s^E , represent the purely mechanical relation between stress and strain with a constant electric field boundary condition denoted by the superscript, E. The constant stress dielectric, ϵ^T , relates the electrical variables, electric field and displacement. The piezoelectric d-constants represent the electromechanical coupling in the material. The subscript, t, simply represents the transpose. The d-constants are an important measure of the actuation strain capability of a piezoceramic under stress-free conditions.

A second form of the constitutive relations,

$$\begin{bmatrix} \mathbf{D} \\ \mathbf{T} \end{bmatrix} = \begin{bmatrix} \epsilon^S & \mathbf{e} \\ -\mathbf{e}_t & \mathbf{c}^E \end{bmatrix} \begin{bmatrix} \mathbf{E} \\ \mathbf{S} \end{bmatrix} \quad (3)$$

involves mechanical stiffness, \mathbf{c}^E , under constant electric field boundary conditions and the piezoelectric e-constants. The e-constants are a measure of the actuator induced stress for fully clamped conditions.

Two significant nonlinearities are neglected by this model of piezoelectric materials. In the standard operating regime, shown in Figure 2-3, one significant nonlinear effect is the hysteresis which results from residual strains in the material that remain after the field has been reduced. The other major effect neglected by the linear model is the non-linear field-strain relationship illustrated in the butterfly curve (see Figure 2-1). The error increases with the field level. The piezoelectric field-strain coupling parameter, the d-constant, represents the slope of the strain-field curve only at the origin. For a more complete discussion of piezoelectric nonlinearities, refer to Anderson and Crawley [1993].

For a monolithic piezoceramic wafer poled through the thickness, the general form of the constitutive relations can be simplified because of the in-plane symmetry:

$$c_{11}^E = c_{22}^E, c_{44}^E = c_{55}^E, d_{31} = d_{32}, \epsilon_1^T = \epsilon_2^T \quad (4)$$

Thus, a monolithic piezoceramic will strain equally within the plane as depicted in Figure 2-2. A PFC actuator, however, requires the fully anisotropic relations. The coupling

matrix for a PFC actuator reflects the anisotropy inherent in a 1-3 composite system. The relatively stiff fibers aligned in the 1-direction dominate the effective stiffness parameter c_{11}^E , while the softer matrix controls c_{22}^E . The statement,

$$c_{11}^E \neq c_{22}^E \quad (5)$$

is representative of the mechanical anisotropy of PFC's.

Similarly, the in-plane piezoelectric coupling coefficients are unequal. The continuity of the fibers in the 1-direction enables greater levels of induced stress or strain. In the transverse direction, the inactive matrix material divides the fibers, resulting in less actuation. This is referred to as the piezoelectric free-strain anisotropy and is represented by:

$$d_{31} \neq d_{32} \quad (6)$$

Figure 2-5 illustrates a characteristic longitudinal expansion and a lesser transverse expansion for a PFC driven with an electric field opposing the net polarization.

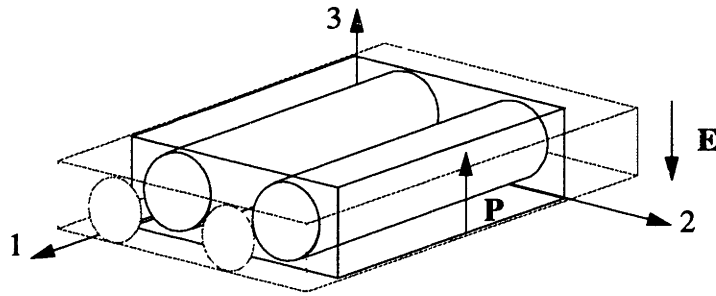


Fig. 2-5. Anisotropic in-plane expansion and through-thickness contraction of a PFC.

A comparison of equations (1) and (3) yields several other useful relations between the electrical, mechanical, and electromechanical coupling coefficients. These are presented here without derivations [Bent *et al*, 1995]:

$$s^E = (c^E)^{-1}, \mathbf{e} = \mathbf{d}c^E, \epsilon^S = \epsilon^T - \mathbf{d}c^E\mathbf{d}_t \quad (7)$$

Both forms of anisotropy contribute to the anisotropic actuation capability because the induced stress capability of a PFC is also greater along the fibers. It is the induced stress that is important in evaluating the actuation authority of a PFC constrained within a host structure. This concept will be fully explained in the laminate modeling section.

2.1.3 Effective Ply Property Model

As previously mentioned, the effective properties of a PFC are a combination of fiber and matrix properties. Several geometric variables are involved, including the

dimensions of the fiber and matrix as well as the distribution of the fibers in the ply. Figure 2-6 depicts a representative cross-section of the fiber/matrix layer perpendicular to the fibers. The fiber spacing parameter or width line fraction is defined as

$$x_2 = \frac{d}{d + w_f} \quad (8)$$

The through-thickness line fraction is defined as

$$x_3 = \frac{d}{t_p} \quad (9)$$

where d is the fiber diameter, t_p is the total thickness, and w_f is the fiber spacing.

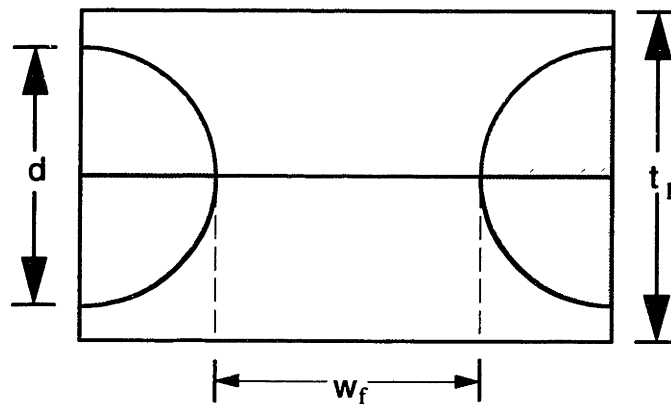


Figure 2-6. DUF model geometric input parameters.

Given the properties of the fiber and matrix materials, as well as the geometric parameter values, the effective three-dimensional properties of the PFC can be approximated. This is accomplished using a Discretized Uniform Fields Model [Hagood and Bent, 1993] which was developed from a generalization of a Mechanics of Materials approach [Jones, 1975]. The major assumption in the latter model is that the longitudinal strains in the fibers and the matrix are equal. Hagood and Bent generalized this to the assumption that the stress, strain, electric field, and electrical displacement in any single phase of the composite are uniform. These assumptions are applied to discretized slices of the fiber and matrix. Then the effective properties of each slice are found using a series combination of the fiber and matrix. The effective properties of each slice are then combined in parallel combinations.

The output of the DUF model includes the effective dielectric permittivity, piezoelectric d -constants, and compliance matrix, which compose the matrix of material properties from equation (1). The full constitutive relation can be expressed as follows:

$$\begin{bmatrix} D_1 \\ D_2 \\ D_3 \\ S_1 \\ S_2 \\ S_3 \\ S_4 \\ S_5 \\ S_6 \end{bmatrix} = \begin{bmatrix} \varepsilon_1^T & 0 & 0 & 0 & 0 & 0 & 0 & d_{15} & 0 \\ 0 & \varepsilon_2^T & 0 & 0 & 0 & 0 & d_{24} & 0 & 0 \\ 0 & 0 & \varepsilon_3^T & d_{31} & d_{32} & d_{33} & 0 & 0 & 0 \\ \hline 0 & 0 & d_{31} & s_{11}^E & s_{12}^E & s_{13}^E & 0 & 0 & 0 \\ 0 & 0 & d_{32} & s_{12}^E & s_{22}^E & s_{23}^E & 0 & 0 & 0 \\ 0 & 0 & d_{33} & s_{13}^E & s_{23}^E & s_{33}^E & 0 & 0 & 0 \\ 0 & d_{24} & 0 & 0 & 0 & 0 & s_{44}^E & 0 & 0 \\ d_{15} & 0 & 0 & 0 & 0 & 0 & 0 & s_{55}^E & 0 \\ 0 & 0 & 0 & 0 & 0 & 0 & 0 & 0 & s_{66}^E \end{bmatrix} \begin{bmatrix} E_1 \\ E_2 \\ E_3 \\ T_1 \\ T_2 \\ T_3 \\ T_4 \\ T_5 \\ T_6 \end{bmatrix} \quad (10)$$

A full description of the experimental characterization methods and values for the material properties and geometric parameters will be presented in the Chapter 4.

2.2 LAMINATE MODEL

With the properties of the individual plies established, the next step in the modeling process is to consider the combination of the plies as a single structure. Classical Lamination Theory is the primary model used to analyze the macro-mechanical behavior of laminated shell structures. For flat plates, simplifications may be introduced. The resulting theory is Classical Laminated Plate Theory (CLPT) which was applied to model the adaptive plates in this study. A rigorous derivation of CLPT may be found in Jones [1975] for passive structures with thermal effects. CLPT has previously been extended to adaptive plates containing isotropic actuators. Crawley and Lazarus [1989] approached the problem as one of actuator induced strains while Jia and Rogers [1989] considered the induced stress. This analysis will consider anisotropic, actuator-induced stress resultants, which consist of the actuator forces and moments applied to the laminate. The first three subsections present the necessary assumptions, property rotation tools, and some notation which contribute to the CLPT in the fourth subsection.

Next, a Rayleigh Ritz plate analysis is developed to predict the response of the adaptive plate to actuator forces and moments. This involves a minimum energy formulation for the plate, including kinetic energy, strain potential energy, and work terms. Solutions are described as is the implementation. Assumed shaped functions are presented and the results of a preliminary evaluation of the accuracy of the model in predicting natural frequencies of laminated plates are discussed. Additionally, a sound radiation prediction is provided in Appendix D.

2.2.1 Plane Stress Simplification

First, the matrix of material properties described in the previous section can be simplified using plane stress assumptions. The local lamina axes are defined in Figure 2-4, with the 1- and 2-axes aligned with the principal material directions. For a thin plate, it can be assumed that the stress through the thickness is negligible, as are the out-of-plane shear stresses.

$$T_3 = T_4 = T_5 \cong 0 \quad (11)$$

The additional constraint that the applied electric field and poling are restricted to the through-thickness or 3-direction allows for a further reduction because

$$E_1 = E_2 = 0 \quad (12)$$

These assumptions are summarized in Figure 2-7, which shows a planar structure with the remaining stresses and electric field.

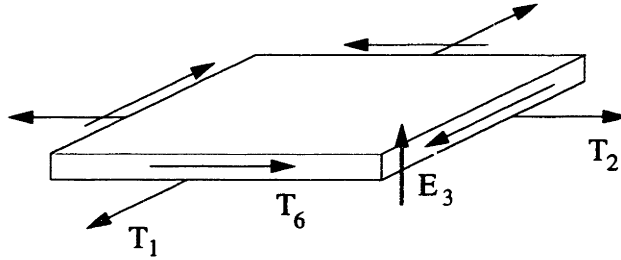


Figure 2-7. Application of plane stress assumptions to the laminate.

These assumptions apply to each ply in the laminate and therefore the material properties in each ply can be reduced. The reduction must be performed with the piezoelectric constitutive relations in the form where stress is an independent variable, as in equation (10). The uncommon d_{24} is more usually approximated as being equal to d_{15} when applied to monolithic piezoceramics. The matrix columns multiplying T_3 , T_4 , T_5 , E_1 , and E_2 can be dropped as well as the corresponding rows as a result of symmetry, resulting in the following reduced constitutive relation for orthotropic materials:

$$\begin{bmatrix} D_3 \\ S_1 \\ S_2 \\ S_6 \end{bmatrix} = \begin{bmatrix} \epsilon_3^T & d_{31} & d_{32} & 0 \\ d_{31} & s_{11}^E & s_{12}^E & 0 \\ d_{32} & s_{12}^E & s_{22}^E & 0 \\ 0 & 0 & 0 & s_{66}^E \end{bmatrix} \begin{bmatrix} E_3 \\ T_1 \\ T_2 \\ T_6 \end{bmatrix} \quad (13)$$

The eliminated dependent variables are zero except for the strain through the thickness,

$$S_3 = d_{33}E_3 + s_{13}^E T_1 + s_{23}^E T_2 \quad (14)$$

which was not considered in the model.

It is important to note that the value of the plane stress stiffness (c^{E*}) is not equivalent to the three-dimensional stiffness (c^E). The plane stress values are denoted with a superscript, '*'. The plane stress values can be found from the compliance using the relations from equation (7).

$$\begin{bmatrix} c_{11}^{E*} & c_{12}^{E*} & 0 \\ c_{12}^{E*} & c_{22}^{E*} & 0 \\ 0 & 0 & c_{66}^{E*} \end{bmatrix} = \begin{bmatrix} s_{11}^E & s_{12}^E & 0 \\ s_{12}^E & s_{22}^E & 0 \\ 0 & 0 & s_{66}^E \end{bmatrix}^{-1} \quad (15)$$

In future references to material properties, it will be assumed that all values are for plane stress, and that the asterisk will be omitted. Other relations between the plane stress constants and the full 3-dimensional constants can be found in [Bent *et al*, 1995].

The final calculation required for the material properties before the rotations is the application of equation (7) to find the piezoelectric induced stress coefficients:

$$\begin{bmatrix} e_{31} \\ e_{32} \\ 0 \end{bmatrix} = \begin{bmatrix} d_{31} & d_{32} & 0 \end{bmatrix} \begin{bmatrix} c_{11}^E & c_{12}^E & 0 \\ c_{12}^E & c_{22}^E & 0 \\ 0 & 0 & c_{66}^E \end{bmatrix} \quad (16)$$

The e-constants are required in the rotation section as are the stiffness values. Note that these constants do not have the same values as the full 3-dimensional constants.

2.2.2 Property Rotations

In order to account for the varied orientations of the laminae, the material properties specific to each lamina must be rotated in-plane to the global laminate axes. The global coordinate system defined in Figure 2-8 has the in-plane axes aligned with the geometry of the plate structure.

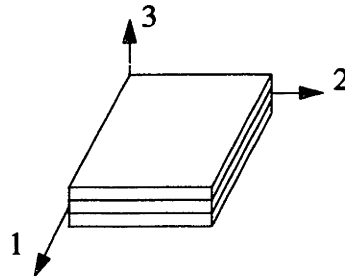


Figure 2-8. Global coordinate frame of laminate.

In general, the ply properties will be rotated through an angle θ from the local ($\tilde{1}$, $\tilde{2}$) system to the global (1, 2) system as shown in Figure 2-9 for a $+\theta$ ply. A positive rotation is defined in a clockwise direction.

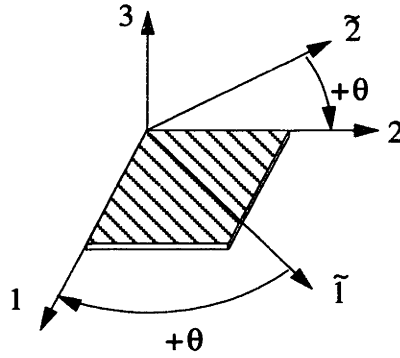


Figure 2-9. Representation of coordinate transformation.

For the purpose of later calculations in the solution procedure, the material properties will be rotated in the form having electric field and strain as the independent variables. The in-plane rotation will require a first order tensor transformation for the electrical properties and a second order transformation for the mechanical properties. The transformations are described in Voigt notation which results in different rotation matrices for stress and strain variables. The rotation matrices relate the field variables in engineering notation as follows:

$$\tilde{\mathbf{D}} = \mathbf{R}_E \mathbf{D}, \quad \tilde{\mathbf{E}} = \mathbf{R}_E \mathbf{E}, \quad \tilde{\mathbf{S}} = \mathbf{R}_S \mathbf{S}, \quad \tilde{\mathbf{T}} = \mathbf{R}_T \mathbf{T} \quad (17)$$

The transformation matrices can be defined using direction cosines [Chia, 1980]. \mathbf{R}_S is called the engineering strain rotation while \mathbf{R}_T is the engineering stress rotation.

$$\mathbf{R}_E = \mathbf{1} \quad (18)$$

$$\mathbf{R}_S = \begin{bmatrix} \cos^2 \theta & \sin^2 \theta & \cos \theta \sin \theta \\ \sin^2 \theta & \cos^2 \theta & -\cos \theta \sin \theta \\ -2 \cos \theta \sin \theta & 2 \cos \theta \sin \theta & \cos^2 \theta - \sin^2 \theta \end{bmatrix} \quad (19)$$

$$\mathbf{R}_T = \begin{bmatrix} \cos^2 \theta & \sin^2 \theta & 2 \cos \theta \sin \theta \\ \sin^2 \theta & \cos^2 \theta & -2 \cos \theta \sin \theta \\ -\cos \theta \sin \theta & \cos \theta \sin \theta & \cos^2 \theta - \sin^2 \theta \end{bmatrix} \quad (20)$$

The factor of two in the rotation matrices arises from the fact that the engineering shear strain is twice as large as the corresponding tensor shear strain by definition. The rotation matrix for the electrical properties, \mathbf{R}_E , is simply a result of the reductions of the variables to scalars in the previous subsection. For passive structural plies, only the stiffness property rotation is required.

The constitutive relations in the local coordinate system can be written as

$$\begin{bmatrix} \tilde{\mathbf{D}} \\ \tilde{\mathbf{T}} \end{bmatrix} = \begin{bmatrix} \mathbf{R}_E \mathbf{D} \\ \mathbf{R}_T \mathbf{T} \end{bmatrix} = \begin{bmatrix} \tilde{\epsilon}^S & \tilde{\mathbf{e}} \\ -\tilde{\mathbf{e}}_t & \tilde{\mathbf{c}}^E \end{bmatrix} \begin{bmatrix} \mathbf{R}_E \mathbf{E} \\ \mathbf{R}_S \mathbf{S} \end{bmatrix} = \begin{bmatrix} \tilde{\epsilon}^S & \tilde{\mathbf{e}} \\ -\tilde{\mathbf{e}}_t & \tilde{\mathbf{c}}^E \end{bmatrix} \begin{bmatrix} \tilde{\mathbf{E}} \\ \tilde{\mathbf{S}} \end{bmatrix} \quad (21)$$

Multiplying by the appropriate inverse rotation matrices yields the new constitutive relations in global coordinates:

$$\begin{bmatrix} \mathbf{D} \\ \mathbf{T} \end{bmatrix} = \begin{bmatrix} \mathbf{R}_E^T \tilde{\epsilon}^S \mathbf{R}_E & \mathbf{R}_E^T \tilde{\mathbf{e}} \mathbf{R}_S \\ -\mathbf{R}_T^{-1} \tilde{\mathbf{e}}_t \mathbf{R}_E & \mathbf{R}_T^{-1} \tilde{\mathbf{c}}^E \mathbf{R}_S \end{bmatrix} \begin{bmatrix} \mathbf{E} \\ \mathbf{S} \end{bmatrix} \quad (22)$$

The global laminate material properties can now be defined in terms of the lamina properties as follows:

$$\epsilon^S = \mathbf{R}_E^T \tilde{\epsilon}^S \mathbf{R}_E, \quad \mathbf{e} = \mathbf{R}_E^T \tilde{\mathbf{e}} \mathbf{R}_S, \quad \mathbf{c}^E = \mathbf{R}_T^{-1} \tilde{\mathbf{c}}^E \mathbf{R}_S \quad (23)$$

Following the rotation into laminate coordinates, the matrix of material properties may no longer contain the zero terms that were present in the local coordinates.

2.2.3 Strain-Displacement Relations

In order to model variations in stress and strain through the thickness of a laminate, several assumptions are made. The assumptions are consistent with those of Classical Laminated Plate Theory [Jones, 1975]. First, the bonds between plies are assumed to be perfect and infinitesimally thin. The bonds are non-shear-deformable so that displacements are continuous and plies cannot slip as shown in Figure 2-10. The shaded region represents the strain in the laminate, which is bounded by the dashed line. In addition, the Kirchhoff hypotheses for thin plates are assumed. Thus a line normal to the middle surface of the laminate remains straight and normal when the laminate is deformed. The length of the normal is also held constant. This is equivalent to ignoring out-of-plane shear strains and the through-thickness strain.

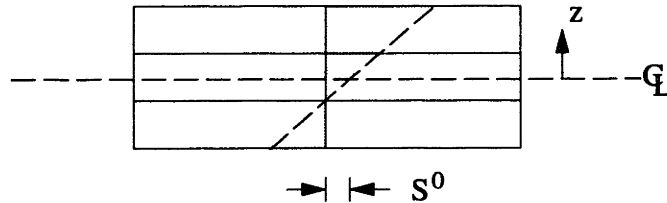


Figure 2-10. Linear strain continuity assumption—strain field in cross-section is described by displacement of plane section to dashed line.

The deformation of the plate resulting from loading can be described in terms of the centerline or midplane displacements ($u_0(x,y)$, $v_0(x,y)$, $w_0(x,y)$). The x -, y -, and z -directions correspond to the previously described laminate axes, 1, 2, and 3. The relationships between displacements and the centerline displacements, denoted with a '0',

are

$$\begin{aligned}
 u &= u_0 - z \frac{\partial w_0}{\partial x} \\
 v &= v_0 - z \frac{\partial w_0}{\partial y} \\
 w &= w_0
 \end{aligned} \tag{24}$$

Note that any reference plane can be chosen in place of the centerline. Figure 2-10 also shows the linear z -dependence of the strains which are functions of x and y .

The midplane strain is the strain level at the centerline. The midplane strains are defined as

$$\begin{bmatrix} S_1^0 \\ S_2^0 \\ S_6^0 \end{bmatrix} = \begin{bmatrix} \frac{\partial u_0}{\partial x} \\ \frac{\partial v_0}{\partial y} \\ \frac{\partial u_0}{\partial y} + \frac{\partial v_0}{\partial x} \end{bmatrix} \tag{25}$$

and the midplane curvatures are

$$\begin{bmatrix} \kappa_1 \\ \kappa_2 \\ \kappa_6 \end{bmatrix} = \begin{bmatrix} -\frac{\partial^2 w_0}{\partial x^2} \\ -\frac{\partial^2 w_0}{\partial y^2} \\ -\frac{2\partial^2 w_0}{\partial x \partial y} \end{bmatrix} \tag{26}$$

The general form for the strains in terms of the midplane strains and curvatures is then

$$\begin{bmatrix} S_1 \\ S_2 \\ S_6 \end{bmatrix} = \begin{bmatrix} S_1^0 \\ S_2^0 \\ S_6^0 \end{bmatrix} + z \begin{bmatrix} \kappa_1 \\ \kappa_2 \\ \kappa_6 \end{bmatrix} \tag{27}$$

The strain-displacement relations are an essential component of the CLPT model.

2.2.4 Classical Laminated Plate Theory

The fundamental element of CLPT is the consideration of a multilayer composite as a single, unified structure. In order to model the laminate, both the in-plane loads and the mechanical stiffnesses for each ply must be lumped to form the overall laminate stress resultants and stiffness properties. The internal force and moment resultants may be

actuator-induced or thermally induced. Externally applied normal and shear stresses may also be considered. The positive orientations for the stress resultants are defined for the n -ply laminate in Figure 2-11. The ply numbering and thickness conventions are also shown.

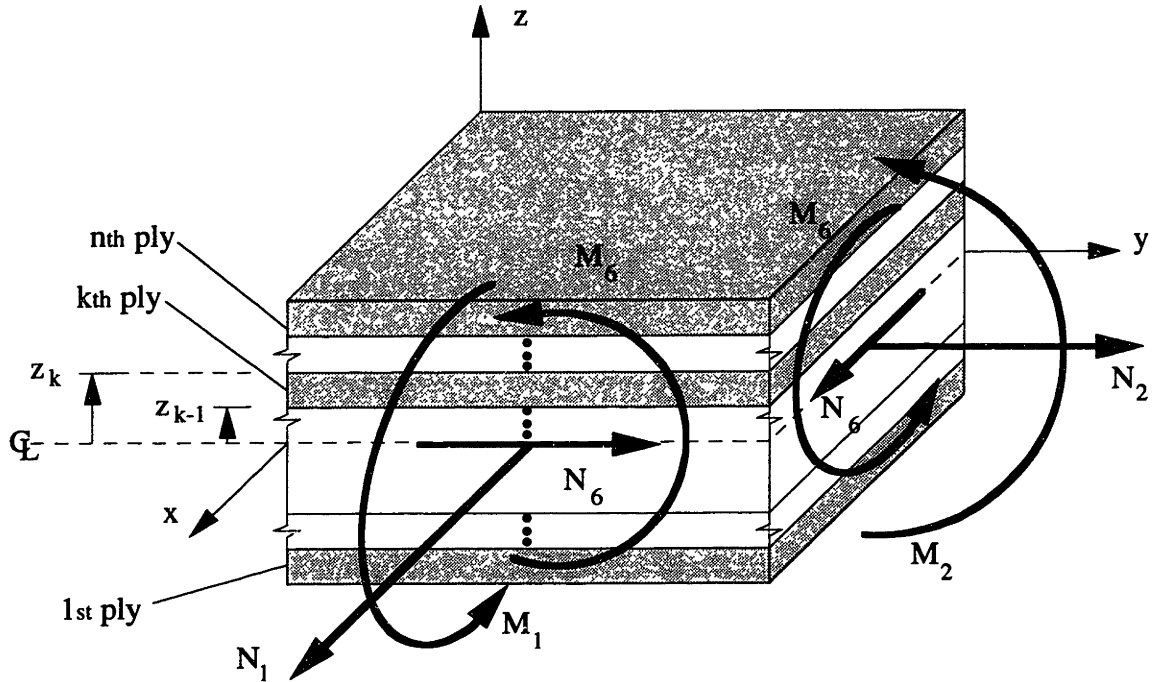


Figure 2-11. Force and moment convention and laminate geometry.

The resultant forces and moments are defined,

$$\begin{bmatrix} \mathbf{N} \\ \mathbf{M} \end{bmatrix} = \sum_{k=1}^n \int_{z_{k-1}}^{z_k} \begin{bmatrix} \mathbf{T} \\ z\mathbf{T} \end{bmatrix} dz \quad (28)$$

where the thickness of the k th ply is given by $(z_k - z_{k-1})$ and,

$$\begin{bmatrix} \mathbf{N} \\ \mathbf{M} \end{bmatrix} = \begin{bmatrix} N_1 \\ N_2 \\ N_6 \\ M_1 \\ M_2 \\ M_6 \end{bmatrix} \quad \text{and} \quad \mathbf{T} = \begin{bmatrix} T_1 \\ T_2 \\ T_6 \end{bmatrix} \quad (29)$$

The stresses can result from either external or internal sources. For an adaptive structure, the stresses can be related from equation (3):

$$\mathbf{T} = \mathbf{c}^E \mathbf{S} - \mathbf{eE} \quad (30)$$

In this equation, \mathbf{eE} is the actuator induced stress, which can be expressed more precisely,

$$\mathbf{eE}_3 = \begin{bmatrix} \mathbf{e}_{31} \\ \mathbf{e}_{32} \\ \mathbf{e}_{36} \end{bmatrix} \mathbf{E}_3 \quad (31)$$

The actuator induced forces and moments can be defined from equation (28):

$$\begin{bmatrix} \mathbf{N}^A \\ \mathbf{M}^A \end{bmatrix} = \sum_{k=1}^{n_A} \int_{z_{k-1}}^{z_k} \begin{bmatrix} \mathbf{eE}_3 \\ \mathbf{eE}_3 z \end{bmatrix} dz \quad (32)$$

where n_A is the number of actuators or active laminae.

Next, the laminate stiffnesses must be defined from the ply properties. The stiffness coefficients are divided into extensional (**A**), bending (**D**), and coupling (**B**) terms. The extensional stiffnesses relate applied forces to resulting strains. Bending stiffnesses relate applied moments to resulting curvatures. The coupling terms relate applied forces to curvatures and applied moments to strains. The CLPT stiffness coefficients are:

$$\begin{aligned} \mathbf{A} &= \sum_{k=1}^n (\mathbf{c}^E)_k (z_k - z_{k-1}) \\ \mathbf{B} &= \frac{1}{2} \sum_{k=1}^n (\mathbf{c}^E)_k (z_k^2 - z_{k-1}^2) \\ \mathbf{D} &= \frac{1}{3} \sum_{k=1}^n (\mathbf{c}^E)_k (z_k^3 - z_{k-1}^3) \end{aligned} \quad (33)$$

In general, the stress resultants and the stiffness can be related using equation (30) as follows:

$$\begin{bmatrix} \mathbf{N}_1 \\ \mathbf{N}_2 \\ \mathbf{N}_6 \\ \mathbf{M}_1 \\ \mathbf{M}_2 \\ \mathbf{M}_6 \end{bmatrix} = \begin{bmatrix} \mathbf{A}_{11} & \mathbf{A}_{12} & \mathbf{A}_{16} & \mathbf{B}_{11} & \mathbf{B}_{12} & \mathbf{B}_{16} \\ \mathbf{A}_{12} & \mathbf{A}_{22} & \mathbf{A}_{26} & \mathbf{B}_{12} & \mathbf{B}_{22} & \mathbf{B}_{26} \\ \mathbf{A}_{16} & \mathbf{A}_{26} & \mathbf{A}_{66} & \mathbf{B}_{16} & \mathbf{B}_{26} & \mathbf{B}_{66} \\ \mathbf{B}_{11} & \mathbf{B}_{12} & \mathbf{B}_{16} & \mathbf{D}_{11} & \mathbf{D}_{12} & \mathbf{D}_{16} \\ \mathbf{B}_{12} & \mathbf{B}_{22} & \mathbf{B}_{26} & \mathbf{D}_{12} & \mathbf{D}_{22} & \mathbf{D}_{26} \\ \mathbf{B}_{16} & \mathbf{B}_{26} & \mathbf{B}_{66} & \mathbf{D}_{16} & \mathbf{D}_{26} & \mathbf{D}_{66} \end{bmatrix} \begin{bmatrix} \mathbf{S}_1^0 \\ \mathbf{S}_2^0 \\ \mathbf{S}_6^0 \\ \kappa_1 \\ \kappa_2 \\ \kappa_6 \end{bmatrix} - \begin{bmatrix} \mathbf{N}_1^A \\ \mathbf{N}_2^A \\ \mathbf{N}_6^A \\ \mathbf{M}_1^A \\ \mathbf{M}_2^A \\ \mathbf{M}_6^A \end{bmatrix} \quad (34)$$

The stress resultants and effective laminate stiffnesses will be used to define the potential energy and work terms in the formulation of the minimum energy solution described in the next section.

2.2.5 Exact Solution

For one special case, an exact solution for the static plate deformation due to applied forces can be found. For a free plate, which has no geometric boundary conditions at the edges, it can be assumed that the laminate stress resultants are zero.

$$\begin{bmatrix} \mathbf{N} \\ \mathbf{M} \end{bmatrix} = \begin{bmatrix} 0 \\ 0 \end{bmatrix} \quad (35)$$

Thus, from equation (34), the strains and curvatures at any point on the plate can be determined exactly.

$$\begin{bmatrix} \mathbf{S}^0 \\ \boldsymbol{\kappa} \end{bmatrix} = \begin{bmatrix} \mathbf{A} & \mathbf{B} \\ \mathbf{B} & \mathbf{D} \end{bmatrix}^{-1} \begin{bmatrix} \mathbf{N}^A \\ \mathbf{M}^A \end{bmatrix} \quad (36)$$

The exact solution can be useful as a check on the approximate solution procedure. In addition, it can serve as an analysis tool in the design of adaptive plates as described in a later section.

For simple laminates, the exact solution can be expressed in detail in order to evaluate the effects of certain parameters on the actuation of a plate. In particular, a simple twist-extension coupled laminate consisting of 2 PFC plies bonded to an isotropic center ply was studied previously [Bent *et al*, 1995]. The expression for the twist curvature was used to determine the optimal characteristics for an anisotropic active ply. The twist curvature was maximized for large piezoelectric free strain anisotropy (d_{31}/d_{32}) and large stiffness anisotropy (c_{11}^E/c_{22}^E).

In the current study, the exact solution was used to determine the optimal lay-up for an adaptive plate. The properties of the anisotropic active plies, except for the fiber spacing, were already established through the selection of PFC's for the actuators. The design of the adaptive plates is described in Section 2.3.

2.2.6 Rayleigh Ritz Method

Energy methods are a solution procedure often applied to problems in mechanics. The methods are based on the Calculus of Variations applied to formulations of the kinetic and potential energy as well as the work involved in a given system. The general premise is that a function relating the various forms of energy in the structural system can be minimized to determine the state of the system. Hamilton's Principle, a variational principle based on Newton's equations of motion, describes the basis of the method. A complete development of variational principles applied to mechanics can be found in Lanczos [1949]. The generalized Hamilton's Principle for a coupled electromechanical system [Crandall, 1968] is

$$\int_{t_1}^{t_2} (\delta K - \delta U_1^M + \delta U_1^E + \delta W_1^M - \delta W_1^E) dt = 0 \quad (37)$$

where K is the kinetic energy, U represents the mechanical (M) and electrical (E) potential energy, and W represents the mechanical and electrical work. The subscript '1', refers to the principal energy, rather than the complimentary form, denoted '2'. The application of this principle to active structures using piezoelectric materials was developed by Hagood *et al* [1990].

The particular form of the variational principle chosen depends upon which field variables are independent. For this actuator problem, an applied electric field and strain distribution are assumed, and are therefore the independent variables. Figure 2-12 illustrates the principal and complimentary electrical and mechanical energy. The definition of \mathbf{DdE} as the principal electrical energy arises from the choice of the independent variables. This fact is also responsible for the opposite signs on the electrical energy terms.

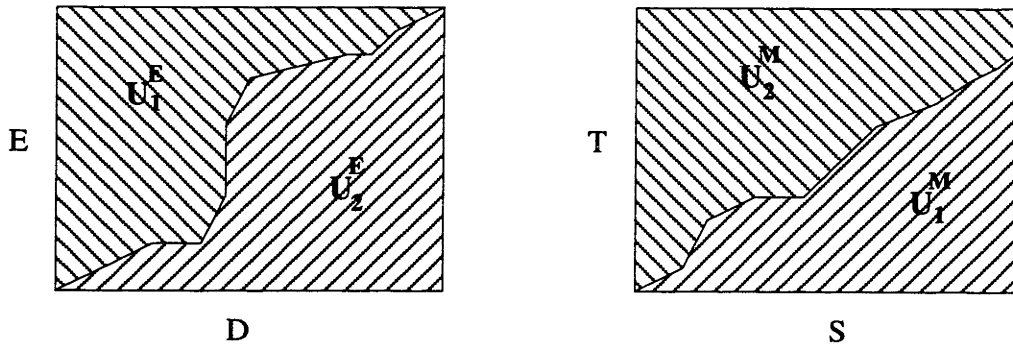


Figure 2-12. Areas representing the principal and complimentary electrical and mechanical energy.

The energy exhibited in any structural motion is the kinetic energy, K , defined

$$\delta K = \int_V \rho \dot{\mathbf{u}}_t \delta \dot{\mathbf{u}} dV \quad (38)$$

The potential energy stored in the mechanical strain, U_1^M , has the variation

$$\delta U_1^M = \int_V \delta \mathbf{S}_t \mathbf{T} dV \quad (39)$$

while the electrical potential energy, representing energy stored in the variation of electric field, has the variation

$$\delta U_1^E = \int_V \delta \mathbf{E}_t \mathbf{D} dV \quad (40)$$

Considering a distributed external force, \mathbf{f} , applied over the surface of the plate (A_S), the variation of mechanical work is:

$$\delta W_1^M = \int_{A_S} \delta \mathbf{u}_t \mathbf{f} dA_S \quad (41)$$

This expression also accounts for any applied point forces. The electrical work from a discrete set of electrodes bounding the active layers is:

$$\delta W_1^E = \delta \phi_t \mathbf{q} \quad (42)$$

where \mathbf{q} is the vector of n_q discrete electrode charges and ϕ is the electrical potential of each. Substitution of these expressions into the variational principle, equation (37), yields,

$$\int_{t_1}^{t_2} \left\{ \left(\int_V \rho \dot{\mathbf{u}}_t \delta \dot{\mathbf{u}} dV \right) - \left(\int_V \delta \mathbf{S}_t \mathbf{T} dV \right) + \left(\int_V \delta \mathbf{E}_t \mathbf{D} dV \right) + \left(\int_{A_S} \delta \mathbf{u}_t \mathbf{f} dA_S \right) - (\delta \phi_t \mathbf{q}) \right\} dt = 0 \quad (43)$$

This equation can be used to define the equations of motion in matrix form for the electromechanical system once the Rayleigh Ritz assumptions have been applied.

The Rayleigh Ritz method is a useful application of Hamilton's Principle for solving static and dynamic structural problems. A complete explanation of the Rayleigh Ritz technique can be found in Meirovitch [1980]. This is an approximate solution based on assumed modes which are used to evaluate the energy terms comprising the specified variational principle. Rayleigh Ritz can be thought of as a method of discretizing an infinite dimensional problem with finite degrees of freedom selected through the choice of assumed mode shapes. The variational principle can also be used to obtain a set of partial differential equations in space and time which may be solved to obtain a spatially continuous description of the system; however, this latter method is more difficult and complicated, and is unnecessary for this application. Another possible approximate solution technique is a finite element model, which can be thought of as Rayleigh Ritz using nodal values for displacements and electrical potential and assumed shape functions within the elements.

The first step in a Rayleigh Ritz solution is to define the displacements and potential as a sum of spatial shape functions scaled by time-varying generalized coordinates or modal amplitudes:

$$\begin{aligned} \mathbf{u}(\mathbf{x}, t) &= \Psi_r(\mathbf{x}) \mathbf{r}(t) = \begin{bmatrix} \psi_{r_1}(\mathbf{x}) \cdots \psi_{r_n}(\mathbf{x}) \end{bmatrix} \begin{bmatrix} r_1(t) \\ \vdots \\ r_n(t) \end{bmatrix} \\ \phi(\mathbf{x}, t) &= \Psi_v(\mathbf{x}) \mathbf{v}(t) = \begin{bmatrix} \psi_{v_1}(\mathbf{x}) \cdots \psi_{v_m}(\mathbf{x}) \end{bmatrix} \begin{bmatrix} v_1(t) \\ \vdots \\ v_m(t) \end{bmatrix} \end{aligned} \quad (44)$$

The n displacement shapes and m potential shapes scaled by generalized coordinates \mathbf{r} and \mathbf{v} , respectively, are used to approximate the solution. The displacement shapes, Ψ_r , must satisfy the geometric boundary conditions of the specific problem, while the potential shapes, Ψ_v , must be consistent with voltage boundary conditions and equipotential at conductors. All shape functions must be sufficiently differentiable.

Before applying the variational principle, the strains and curvatures must be related to the generalized coordinates. From the strain displacement relations, equations (25) and (26):

$$\begin{bmatrix} \mathbf{S}^0 \\ \boldsymbol{\kappa} \end{bmatrix} = \mathbf{L}_u \mathbf{u} = \mathbf{L}_u \Psi_r(\mathbf{x}) \mathbf{r}(t) \quad (45)$$

where \mathbf{L}_u is a differential operator matrix defined [Crawley and Lazarus, 1989]:

$$\mathbf{L}_u = \begin{bmatrix} \frac{\partial}{\partial x} & 0 & 0 \\ 0 & \frac{\partial}{\partial y} & 0 \\ \frac{\partial}{\partial y} & \frac{\partial}{\partial x} & 0 \\ 0 & 0 & -\frac{\partial^2}{\partial x^2} \\ 0 & 0 & -\frac{\partial^2}{\partial y^2} \\ 0 & 0 & -\frac{2\partial^2}{\partial x \partial y} \end{bmatrix} \quad (46)$$

This matrix will have as many columns as there are shape functions. The electric field can be defined similarly,

$$\mathbf{E} = \mathbf{L}_\phi \phi = \mathbf{L}_\phi \Psi_v(\mathbf{x}) \mathbf{v}(t) \quad (47)$$

For this plate actuation problem, the electric field and poling direction are aligned through the thickness, and are only defined within the active laminae. In addition, the assumption of no internal charge distribution simplifies the possible electrical shape function to a linear function through the thickness of the actuator. Therefore the only assumed electrical distribution required is:

$$\mathbf{E} = E_3(t) \hat{\mathbf{k}} \quad (48)$$

Now the variational principle in equation (43) can be restated in terms of the generalized coordinates after incorporating the modal assumptions [Fripp, 1995] from equations (45) and (47). In addition, the stress and electrical displacement can be

expressed in terms of the generalized coordinates using the constitutive relations from equation (3). The kinetic energy term was integrated by parts in time, so that the variations would not involve any time derivatives. The resulting equation is:

$$\int_{t_1}^{t_2} \left\{ \int_V \delta \mathbf{r}_t \left(-(\boldsymbol{\Psi}_r)_t \rho \boldsymbol{\Psi}_r \ddot{\mathbf{r}} - (\mathbf{L}_u \boldsymbol{\Psi}_r)_t \mathbf{c}^E \mathbf{L}_u \boldsymbol{\Psi}_r \mathbf{r} \right) dV + \int_V \delta \mathbf{v}_t (\mathbf{L}_\phi \boldsymbol{\Psi}_v)_t \boldsymbol{\varepsilon}^S \mathbf{L}_\phi \boldsymbol{\Psi}_v \mathbf{v} dV + \int_{A_S} (\boldsymbol{\Psi}_r \delta \mathbf{r})_t \mathbf{f} dA_S - (\boldsymbol{\Psi}_v \delta \mathbf{v})_t \mathbf{q} \right\} dt = 0 \quad (49)$$

Allowing for the arbitrary variations of the generalized coordinates, \mathbf{r} and \mathbf{v} , yields the equations of motion in matrix form:

$$\mathbf{M} \ddot{\mathbf{r}} + \mathbf{K} \mathbf{r} = \mathbf{B}_f + \boldsymbol{\Theta} \mathbf{v} \quad (50)$$

$$\boldsymbol{\Theta}_t \mathbf{r} + \mathbf{C} \mathbf{v} = \mathbf{B}_q \mathbf{q} \quad (51)$$

The first equation is the actuator equation, which will be used here; the second equation is the sensor equation, which is also used for piezoelectric charge control and other applications. \mathbf{M} is the generalized mass matrix, \mathbf{K} the generalized stiffness matrix, $\boldsymbol{\Theta}$ the electromechanical coupling matrix, and \mathbf{C} the capacitance matrix. \mathbf{B}_f represents the externally applied forces and \mathbf{B}_q relates applied charges (\mathbf{q}) to the generalized coordinates.

The generalized mass is defined as

$$\mathbf{M} = \int_V (\boldsymbol{\Psi}_r)_t \rho \boldsymbol{\Psi}_r dV = \int_{A_S} (\boldsymbol{\Psi}_r)_t \left(\int_t \rho dz \right) \boldsymbol{\Psi}_r dA_S \quad (52)$$

where A_S is the planform area of the plate and t is the thickness. The stiffness is expressed using the CLPT terms from equation (33) for the laminate,

$$\mathbf{K} = \int_{A_S} (\mathbf{L}_u \boldsymbol{\Psi}_r)_t \begin{bmatrix} \mathbf{A} & \mathbf{B} \\ \mathbf{B} & \mathbf{D} \end{bmatrix} \mathbf{L}_u \boldsymbol{\Psi}_r dA_S \quad (53)$$

The fully expanded expression for the generalized stiffness can be found in Whitney [1987]. The electromechanical coupling matrix is defined:

$$\boldsymbol{\Theta} = \int_V (\mathbf{L}_u \boldsymbol{\Psi}_r)_t \mathbf{e} \mathbf{L}_\phi \boldsymbol{\Psi}_v dV \quad (54)$$

For actuation of the adaptive plate, the piezoelectric coupling term, $\boldsymbol{\Theta} \mathbf{v}$, can be written as the actuator forcing term,

$$\Theta \mathbf{v} = \int_{A_S} (\mathbf{L}_u \psi_r)_t \begin{bmatrix} \mathbf{N}^A \\ \mathbf{M}^A \end{bmatrix} dA_S \quad (55)$$

where the actuator stress resultants are defined as in equation (32). The capacitance matrix for the sensor equation can be defined:

$$\mathbf{C} = \int_V (\mathbf{L}_\phi \psi_v)_t \epsilon^S \mathbf{L}_\phi \psi_v dV \quad (56)$$

Any applied forces and electrode charges are included using \mathbf{B}_f and $\mathbf{B}_q \mathbf{q}$, respectively, where

$$\begin{aligned} \mathbf{B}_f &= \int_{A_S} (\psi_r)_t \mathbf{f} dA_S \\ \mathbf{B}_q &= \left[\left(\psi_v(\mathbf{x}_{q_1}) \right) \cdots \left(\psi_v(\mathbf{x}_{q_{n_q}}) \right) \right] \end{aligned} \quad (57)$$

If point forces are to be considered, the vector of shape functions in equation (57) would be evaluated at the point of application for each force vector included.

Solutions

Next, the solutions for the actuator equation will be provided for some special cases. Equation (49) can be solved for the generalized displacement, \mathbf{r} , using linear algebra. The vector \mathbf{r} describes the relative contribution of each assumed shape to the motion of the structure. First, for a static problem with no external forces, the actuator-induced deflections can be determined:

$$\mathbf{r} = \mathbf{K}^{-1} \Theta \mathbf{v} \quad (58)$$

This is the simplest case where \mathbf{v} is the amplitude of the applied electric field.

For the dynamic solutions, a harmonic time dependence is assumed,

$$\mathbf{r}(t) = \mathbf{r} e^{i\omega t} \quad (59)$$

This expression may be substituted into equation (49), resulting in,

$$-\omega^2 \mathbf{M} \mathbf{r} + \mathbf{K} \mathbf{r} = \Theta \mathbf{v} \quad (60)$$

for the case of no external forcing. The unforced dynamic solution, which will determine the natural modes and resonant frequencies of the adaptive plate, is found from:

$$\mathbf{K} \mathbf{p} = \Lambda \mathbf{M} \mathbf{p} \quad (61)$$

where Λ is a diagonal matrix of n eigenvalues and \mathbf{p} is a matrix of the n associated eigenvectors. The square roots of the eigenvalues yield the natural frequencies, while the

corresponding eigenvectors represent the modes. Each eigenvector is a generalized coordinate vector, \mathbf{r} . This results from the finite degrees of freedom in the approximate solution to an infinite-dimensional problem. Adequate selection of assumed shape functions will enable an accurate solution for the first n modes of the plate.

Finally, the forced dynamic solution for a sinusoidal applied force, i.e. an AC-electric field, is

$$\mathbf{r} = (\mathbf{K} - \omega^2 \mathbf{M})^{-1} \Theta \mathbf{v} \quad (62)$$

where ω is the excitation frequency. In each case, the resulting generalized coordinate vector corresponding to a natural mode of the structure or a response to forcing can be converted to displacements over the plate area using equation (44). The sum of the contributions of the assumed shape functions, scaled by the generalized coordinates, determines the approximate deformation of the plate:

$$\mathbf{u} = \sum_{i=1}^n \Psi_{r_i} r_i \quad (63)$$

where n is the number of assumed displacement shape functions.

2.2.7 Implementation

The entire adaptive plate model was implemented using MATLAB¹. The complete code is provided in Appendix A. Inputs include the dimensions, lay-up, material, actuators and location, applied field, type and number of shape functions, and level of accuracy for numerical integration routines. Some common material properties are referenced from a look-up table, also shown in the appendix.

The integrals defined in equations (52), (53), and (55) are evaluated using a 2-dimensional Gaussian Quadrature. In this method, the integral is evaluated at a finite number of points over the area. The contribution of each of the points is included in a weighted sum to approximate the complete integral. The 2-dimensional quadrature is a nesting of two single integral approximations. The inner integral is approximated using a Gauss-Legendre integration [Press *et al*, 1986],

$$\int_{-1}^1 f(x) dx = \sum_{i=1}^n w_i f(x_i) \quad (64)$$

where the x_i are the Gaussian abscissas and the w_i are the Gaussian weights.

This sum represents the contribution of a given row. Then the rows must be

¹ MATLAB 4.2, The MathWorks, Inc., Natick, MA.

summed using a second Gauss-Legendre integral. The double integral is then expressed

$$\int_{-1}^1 \int_{-1}^1 f(x,y) dA = \sum_{j=1}^m \left(w_j \sum_{i=1}^n \left(w_i f(x_i, y_j) \right) \right) \quad (65)$$

The grid for an 8-point quadrature is shown in Figure 2-13. The abscissas and weights for any number of points can be derived [Press *et al*, 1986] or referenced from a table [Abramowitz and Stegun, 1964]. Increasing the number of points used in the numerical approximation improves the accuracy of the method. The disadvantage is increased run time. The total number of points evaluated is mn . An 8-point by 8-point quadrature was used in model simulations unless otherwise specified. The code can handle up to a 96-point quadrature, which has 9216 grid points. The number of points can be increased to test the convergence of the solutions obtained.

In order to increase the efficiency of the integration process, the spatial dependence of the laminate stiffness properties ($\mathbf{A}, \mathbf{B}, \mathbf{D}$) was eliminated from the routine. First, the stiffness integral was evaluated for the structure with all active elements eliminated. Then

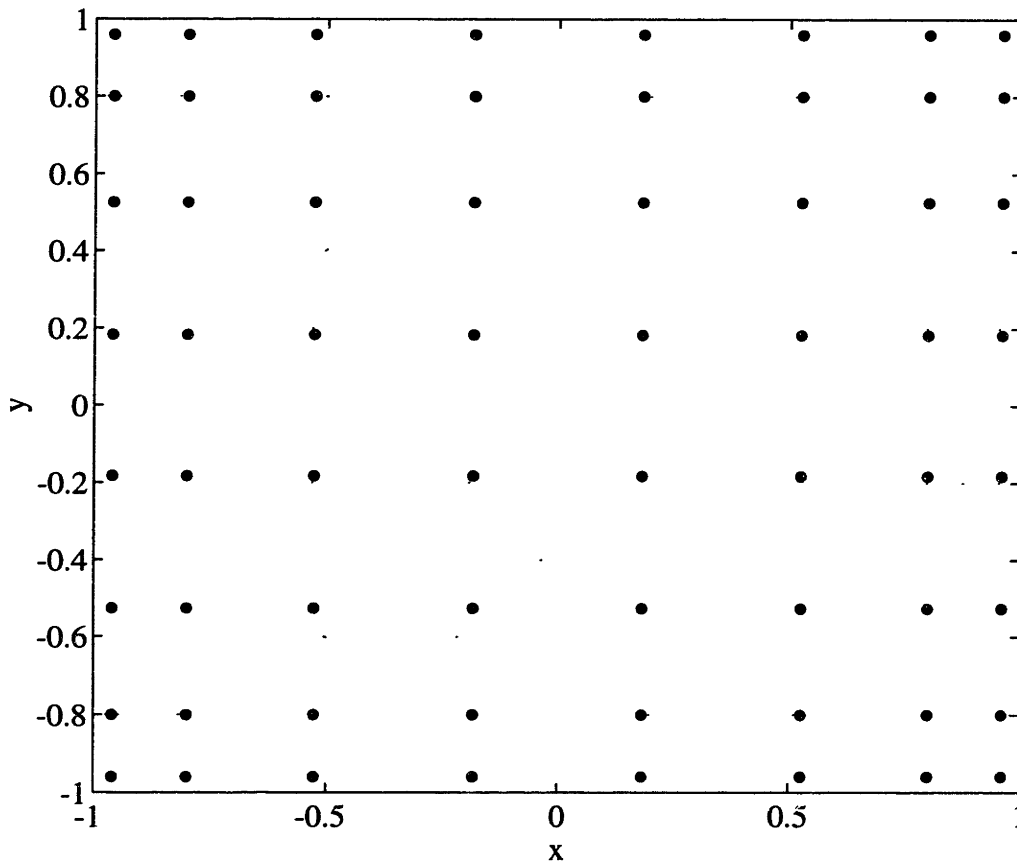


Figure 2-13. 8-point quadrature example.

the integral was re-evaluated for each individual actuator or active ply. The effects were then combined to obtain the true laminate stiffness. Figure 2-14 illustrates the procedure. The linear superposition principle allows for this simplification which greatly reduced run time with an increase of accuracy since the points are distributed over each element with no discontinuities.

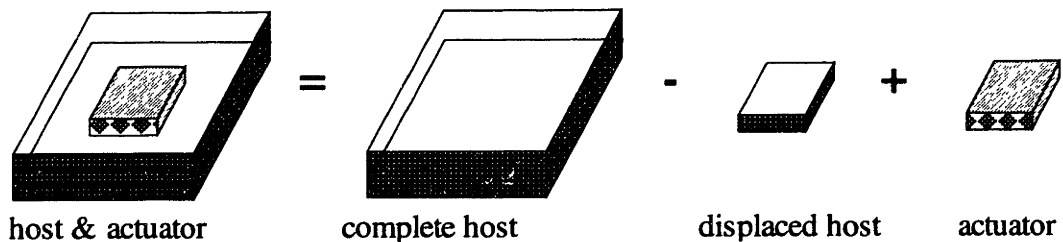


Figure 2-14. Method for the elimination of spatial dependence from area integrals.

2.2.8 Assumed Shape Functions

The selection of the assumed displacement modes for a plate is the determining factor for the accuracy of model predictions. The shapes must satisfy the boundary conditions of the plate in order to constrain the solutions equivalently. In addition, the shapes must provide enough degrees of freedom to adequately represent the true motion of the plate in some combination. Increasing the number of shape functions increases the modal degrees of freedom in the problem and reduces the error. However, it is desirable to have fewer shape functions which more accurately represent the modes of the structure in order to improve efficiency. Often, the number of shape functions can be reduced once unnecessary shape functions have been identified.

Assumed shapes must be considered for each direction in the structure, u , v , and w . For a typical plate, the out-of-plane modes tend to dominate the low frequency response, though some in-plane deformation may be involved. The in-plane shape functions are therefore rather simple, while the out-of-plane functions must be more detailed in representing the plate deformation.

In-Plane Shapes

The in-plane deflection shapes can usually be modeled with simple linear polynomials as shown in Table 2-1 [Lazarus and Crawley, 1989]. These represent the uniform transverse and longitudinal expansion of the plate, as well as shear deformations. More complicated shape functions may be required for plates with discontinuous actuators, where the deformation is limited to the actuated sections. The selection of the shapes must

reflect the boundary conditions of the plate as well.

Table 2-1. In-Plane Polynomial Shape Functions

Extension Shapes	$u = \frac{x}{a}, \quad v = \frac{y}{b}$
Shear Shapes	$u = \frac{y}{b}, \quad u = \frac{xy}{ab}; \quad v = \frac{x}{a}, \quad v = \frac{xy}{ab}$

Out-of-Plane Shapes

In some cases, it is possible to represent out-of-plane deflections with simple polynomials. For example, a plate expected to have constant curvatures can be well modeled using no greater than second order polynomials, as shown in Table 2-2 for a cantilevered plate. The selection of these shapes depends on the edge geometric boundary conditions. Higher order polynomials may be used to represent the higher modes of the plate.

Table 2-2. Out-of-Plane Polynomial Shape Functions

Bending Shapes	$w = \left(\frac{x}{a}\right)^2, \quad w = \left(\frac{y}{b}\right)^2, \quad w = \frac{x}{a}\left(\frac{y}{b}\right)^2, \quad w = \left(\frac{x}{a}\right)^2 \frac{y}{b}$
Twisting Shapes	$w = \frac{xy}{ab}$

More complicated shape functions may better represent the modes of the plate. One possibility is to use the standard beam deflection shapes found in Blevins [1987]. The beam functions are the exact solutions for the natural modes of beams, which can be combined to form approximate plate deflection shapes. Another option is to use a set of orthogonal polynomials such as Bessel Functions [Arfken, 1985]. These may not represent the true modes of the plate individually, but a combination of several orthogonal functions can eventually achieve a suitable level of accuracy in cases where the true modes are not known. Some sets of shape functions have been specifically developed for certain classes of composite laminates, such as those found in Jensen *et al* [1982] for bend-twist coupled laminates. These functions more accurately model the natural modes of the laminates, allowing for fewer shape functions to be used in the analysis. The Jensen functions will be described below.

The shape functions included in the Rayleigh Ritz model supports the basic

geometric boundary conditions. These include free (F), simply-supported (SS), and clamped (C). They can be applied in any combination for the four edges. Table 2-3 describes the conditions for out-of-plane displacement for various geometries at an edge. The boundary conditions may be applied to any edge, though they are shown for $x=0$. When opposite edges are free (F-F), rigid body translation and rotation modes are included along that particular axis. The rigid body rotation is also included for the simply-supported-free (SS-F) case.

Table 2-3. Geometric Boundary Conditions Along an Edge ($x=0$).

Geometry	Conditions
Free	$w''(0,y) = 0$
Simply-Supported	$w(0,y) = 0; w''(0,y) = 0$
Clamped	$w(0,y) = 0; w'(0,y) = 0$

In general, both the type of shape functions and the number of shape functions required must be determined for the specific problem. Simple polynomials and products of beam functions may be sufficient for isotropic plates; however, plates exhibiting strong mechanical couplings may require special shape functions. Usually, several solutions involving different types of shape functions can be compared for relative accuracy in predicting mode shapes. In addition, the number of shapes used will depend on the complexity of the modes being modeled. Adding more shape functions to the analysis reduces any possible unintended constraints on the problem, making the solutions more accurate. Unnecessary shapes can then be cut out to improve the solution time.

The cantilevered plate which was manufactured as described in the next chapter was modeled using the special out-of-plane shape functions developed by Jensen *et al* for bend-twist coupled laminates. A comparison of model predictions using each of the classes of out-of-plane shapes described above concluded that the beam functions and other polynomial functions overconstrained the plate. Increasing the number and complexity of these functions resulted in a convergence of the solutions toward the predictions using the Jensen functions. These included two bending modes (B1, B2), two torsional modes (T1, T2), and a chordwise bending mode (C1). Figure 2-15 illustrates the five shape functions. The equations for the shapes are listed in Appendix B. The bending modes are simple cantilever beam modes. The torsional modes were derived from St. Venant torsion theory for a beam. Although the torsional modes do not satisfy the slope boundary conditions at the root or account for cross-sectional warping, an experimental investigation described in

the reference has shown that more complicated plate mode shapes did not significantly improve model predictions.

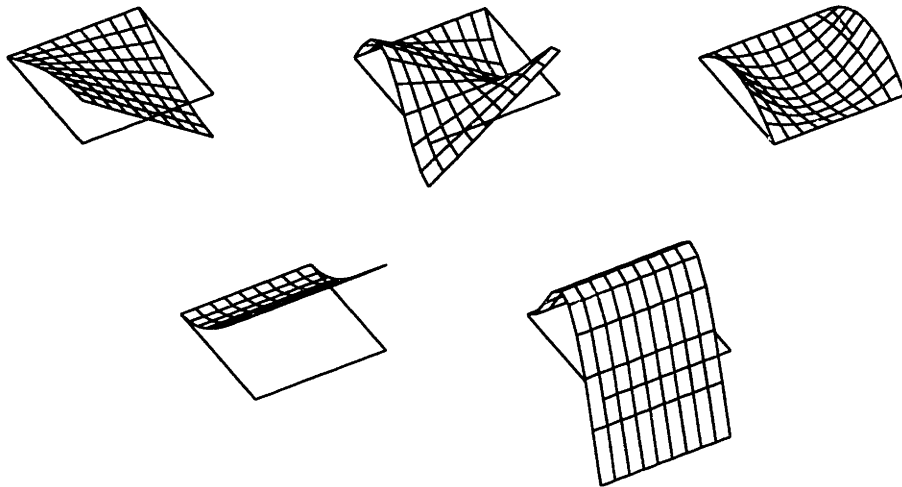


Figure 2-15. Five cantilevered plate shape functions; Upper: T1, T2, C1; Lower: B1, B2.

2.2.9 Preliminary Model Validation

Comparisons were made for the predicted modes of bend-twist coupled graphite/epoxy laminates [Jensen *et al*, 1982]. These laminates reflect the more complicated plates which were used to model the experiments in this thesis. Results are shown in Table 2-4 for several different lay-ups. The table presents the current Rayleigh Ritz model predictions along with values for experimental, Ritz, and FEM natural frequencies from the reference. The error for the various model predictions is given in parentheses. The material properties used in the referenced models accounted for differences in the extensional and flexural moduli. The current model was not able to use the two sets of values, so only the stiffer extensional values were used. The FEM used a 365 degree of freedom solution.

In general, the 5 shape functions predicted the correct mode shapes with natural frequencies within 20% of the experimental values. The FEM was more accurate, but much more computationally intensive. The Rayleigh Ritz model did not perform as well as the referenced model as a result of the less accurate stiffness values used. However, it is expected that these shape functions should adequately model the bending and twisting actuation of the experimental adaptive plate.

Additionally, predictions for the static deflection of a free plate actuated with PFC's were compared with the exact solution described in equation (34). Correlation was perfect for these constant curvature problems. The model predictions for the natural frequencies of

free and cantilevered, isotropic plates were compared with referenced values from Blevins [1987]. A table summarizing these comparisons is provided in Appendix C.

Table 2-4. Comparison of Models and Data for Symmetric Laminates [Jensen *et al*, 1982].

Lay-up	Mode	Experiment	Ritz-ref		FEM-ref		Ritz	
[0 ₂ /90] _s	B1	11.2	11.1	(1)	11.1	(1)	12.7	(13)
	B2	70.5	69.3	(-2)	69.5	(-1)	79.8	(13)
	T1	42.4	39.6	(-7)	39.5	(-7)	35.5	(-16)
[15 ₂ /0] _s	B1	9.4	8.7	(-7)	8.9	(-5)	9.0	(-4)
	B2	66.2	59.9	(-10)	62.7	(-5)	65.1	(-2)
	T1	45.8	48.2	(5)	42.9	(-6)	47.8	(4)
[30 ₂ /0] _s	B1	6.6	6.2	(-6)	6.3	(-5)	6.2	(-6)
	B2	40.0	42.0	(5)	37.3	(-7)	44.3	(11)
	T1	59.1	60.7	(3)	56.9	(-4)	64.6	(9)
[45 ₂ /0] _s	B1	4.8	4.8	(0)	4.9	(2)	5.1	(6)
	B2	29.8	32.6	(9)	30.1	(1)	35.4	(19)
	T1	51.3	56.3	(10)	49.4	(-4)	58.7	(14)
[60 ₂ /0] _s	B1	4.3	4.2	(-2)	4.2	(-2)	4.6	(7)
	B2	27.1	26.8	(-1)	26.1	(-4)	29.9	(10)
	T1	47.7	47.1	(-1)	41.7	(-13)	47.8	(1)
[75 ₂ /0] _s	B1	3.8	3.9	(3)	3.9	(3)	4.4	(16)
	B2	25.1	24.4	(-3)	24.3	(-3)	27.9	(11)
	T1	38.9	39.2	(1)	36.7	(-6)	39.1	(1)
[90 ₂ /0] _s	B1	3.7	3.8	(3)	3.8	(3)	4.4	(19)
	B2	24.3	23.9	(-2)	23.9	(-2)	27.5	(13)
	T1	38.2	35.1	(-8)	35.1	(-8)	34.5	(-10)

Note: Natural frequencies are in Hz and errors in (%).

2.3 ADAPTIVE PLATE DESIGN

Using the combination of predicted PFC properties from the DUF model and the solution for the static deformation from the Ritz model, an adaptive plate was designed. The primary design objective was to maximize twist by direct twist actuation, M_6^A , using a pair of active laminae. The secondary objective was to demonstrate independent bending

and twisting actuation. It was also desirable to have the active plies completely embedded between the composite host laminae in order to demonstrate a fully integrated actuator system.

The actuation capabilities of the laminate depend upon the passive coupling created by the stiffness properties of the particular plate lay-up. The coupling between the induced forces and moments and the resulting centerline strains and curvatures in the laminate can be shown in the CLPT stiffness matrix. The passive couplings can be easily evaluated in a stress-free laminate, where an exact solution is possible. From equation (34), the exact solution is:

$$\begin{bmatrix} S_1^0 \\ S_2^0 \\ S_6^0 \\ \kappa_1 \\ \kappa_2 \\ \kappa_6 \end{bmatrix} = \begin{bmatrix} A_{11} & A_{12} & A_{16} & B_{11} & B_{12} & B_{16} \\ A_{12} & A_{22} & A_{26} & B_{12} & B_{22} & B_{26} \\ A_{16} & A_{26} & A_{66} & B_{16} & B_{26} & B_{66} \\ B_{11} & B_{12} & B_{16} & D_{11} & D_{12} & D_{16} \\ B_{12} & B_{22} & B_{26} & D_{12} & D_{22} & D_{26} \\ B_{16} & B_{26} & B_{66} & D_{16} & D_{26} & D_{66} \end{bmatrix}^{-1} \begin{bmatrix} N_1^A \\ N_2^A \\ N_6^A \\ M_1^A \\ M_2^A \\ M_6^A \end{bmatrix} \quad (66)$$

By choosing an antisymmetric lay-up for the entire laminate, both bend-twist (D_{16} , D_{26}) and extension-shear (A_{16} , A_{26}) couplings are eliminated because the laminae are generally orthotropic [Jones, 1975]. Extension-twist (B_{16} , B_{26}) coupling remains and can be exploited when both active laminae are actuated in-phase. Figure 2-16 compares the simplified out-of-plane and in-plane deflections of the free edges of a cantilevered plate. For an antisymmetric lay-up, twisting and bending can be separated into two distinct operating modes.

In contrast, a symmetric laminate (including symmetric active plies) would eliminate extension-twist coupling and the twist stress resultant, but would allow bend-twist coupling. In-phase operation would result in in-plane extension and shear deflections, while out-of-phase operation would result in a combination of bending and twisting. The antisymmetric laminate was chosen for this design in order to attempt to independently actuate twisting and bending.

In order to achieve the primary design objective of maximizing twist, several geometric parameters were selected. In this simple design, the number and location of structural host plies and the ply orientations, both active and passive, were considered. In addition, the fiber spacing within the active plies was selected .

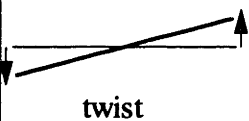



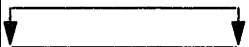



operation	Antisymmetric Lay-up		Symmetric Lay-up	
	out-of-plane	in-plane	out-of-plane	in-plane
in-phase				
out-of-phase				

Figure 2-16. Comparison of deflections for cantilevered plates with two PFC actuators in two modes of operation (end view and planform view).

Previous studies have considered optimal size and placement algorithms for piezoceramic actuators [Masters and Jones, 1993]. In addition, twist actuation with PFC's was demonstrated for actuators bonded to an isotropic plate [Bent *et al*, 1995]. In that experiment, a $+45^\circ$ and a -45° PFC were selected to maximize the twist stress resultant. The twist stress resultant,

$$M_6^A = \frac{1}{2} \sum_{k=1}^n (e_{36} E_3)_k \left((z_3)_k^2 - (z_3)_{k-1}^2 \right) \quad (67)$$

is maximized with large values of e_{36} and a large moment arm ($|z|$) from the neutral axis. The piezoelectric induced shear constant,

$$e_{36} = \sin \theta \cos \theta (\tilde{e}_{31} - \tilde{e}_{32}) \quad (68)$$

results from the stiffness and piezoelectric anisotropies of the active ply. The values of the piezoelectric induced stress constants in lamina coordinates were calculated in equation (16). The value of e_{36} is maximized at $\pm 45^\circ$ ply angles, which were the selected active ply orientations for the adaptive plate design.

In general, the actual twist for a clamped plate does not have an exact solution, and as a result, the optimal lay-up cannot be explicitly determined. Therefore, a design study was performed to find lay-ups which maximized twist in 4-, 5-, and 6-ply antisymmetric laminates. All ply angles were varied in 15° increments to find the best combination for each number of plies. In all cases, the outer plies were graphite/epoxy, followed by the active plies, and then either 0, 1, or 2 inner graphite/epoxy plies. The variation in the number of inner plies tested the effect of the increased moment arm for the twist stress

resultant. The inner and outer ply angles were varied between -90° and $+90^\circ$. The active ply properties used for the Rayleigh Ritz model in this design are listed in Table 2-5.

Table 2-5. Optimization Input Properties [Bent, 1994]

s_{11}^E	s_{12}^E	s_{22}^E	s_{66}^E	d_{31}	d_{32}
111	-36.2	297	697	-14.6	-10.2

Units: compliance (pm^2/N), d-constants (pm/V)

Some results of the study are plotted in Figure 2-17. The predicted twist for 4-, 5-, and 6-ply laminates is shown as a function of the outer graphite ply angles. The inner ply orientation had a much smaller effect on the twist. Therefore it was held constant in the figure. With the addition of more inner plies, the larger actuator moment arm was outweighed by the increased stiffness of the laminate. A $[90/45_A/90/-45_A/90]$ laminate was found to exhibit the most twist, with a $[90/45_A/0/-45_A/90]$ laminate being the next best. These designs exhibited the least torsional stiffness. The latter was chosen for the design

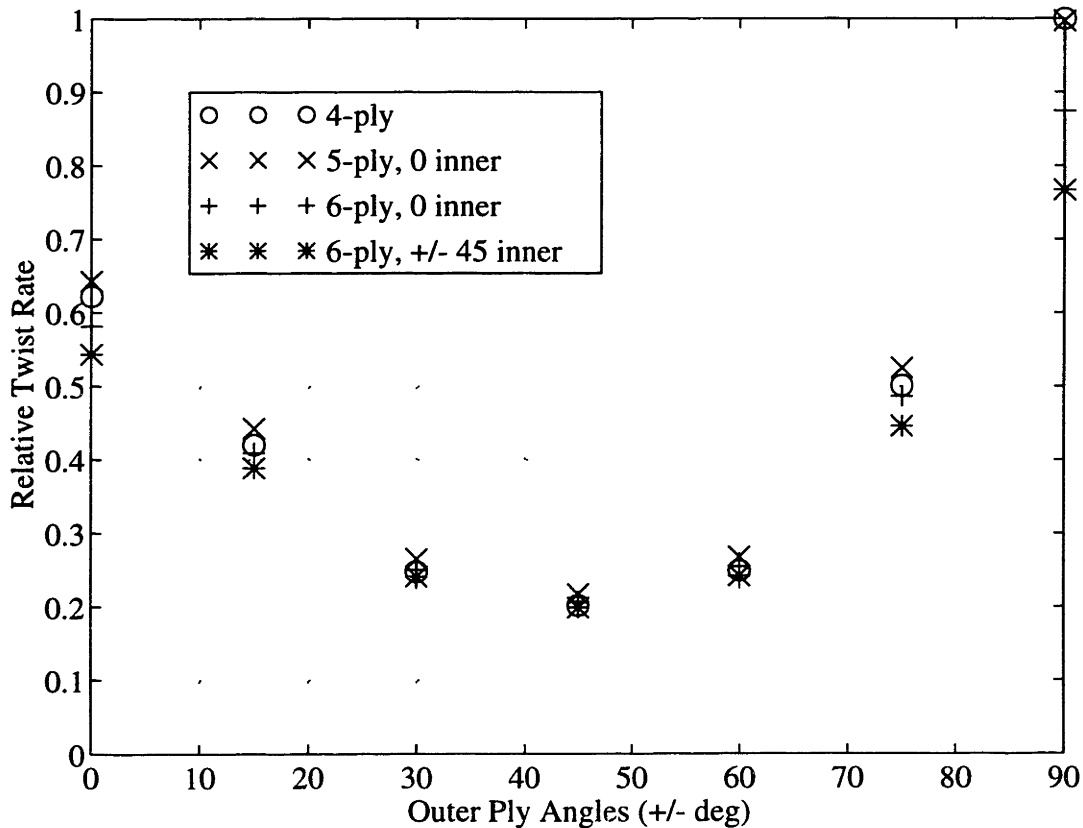


Figure 2-17. Comparison of predicted twist for various laminates.

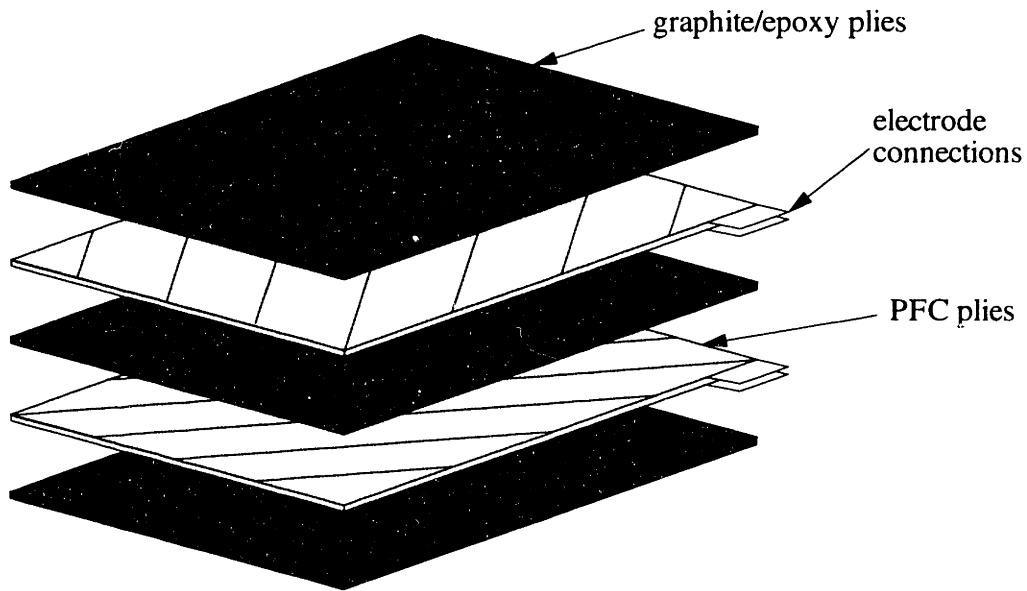


Figure 2-18 Adaptive plate with electrode connections.

for more balanced stiffness properties, because of the larger longitudinal stiffness afforded by the 0° ply. The adaptive plate design is pictured in Figure 2-18. The best 4-ply laminate was roughly 3% less effective, while the best 6-ply laminate was 10% less effective. This was a result of the trade-off between increasing the actuator-induced stress resultant while also increasing the torsional stiffness with the addition of inner plies.

An additional design study was performed at the ply level using the DUF model in conjunction with the adaptive plate model. The fiber spacing or piezoceramic volume fraction was selected to maximize the twist obtained in the laminate. Maximizing the piezoelectric induced shear stress coefficient, e_{36} , will maximize the twist stress resultant, as shown in equation (67). In general, the passive coupling properties of the laminate must also be considered in the design. The fiber spacing effects the stiffness properties of the laminate in addition to the induced shear capabilities of the active lamina. Figure 2-19 shows the normalized values for the induced twist in the laminate as a function of the x_2 line fraction of fibers. The maximum occurs for a 0.75 line fraction, which is equivalent to a volume fraction of 0.56. In this particular design in which the structural host plies were either 0° or 90° plies, the optimal fiber spacing for twist was the same as the optimal for induced shear within the active ply.

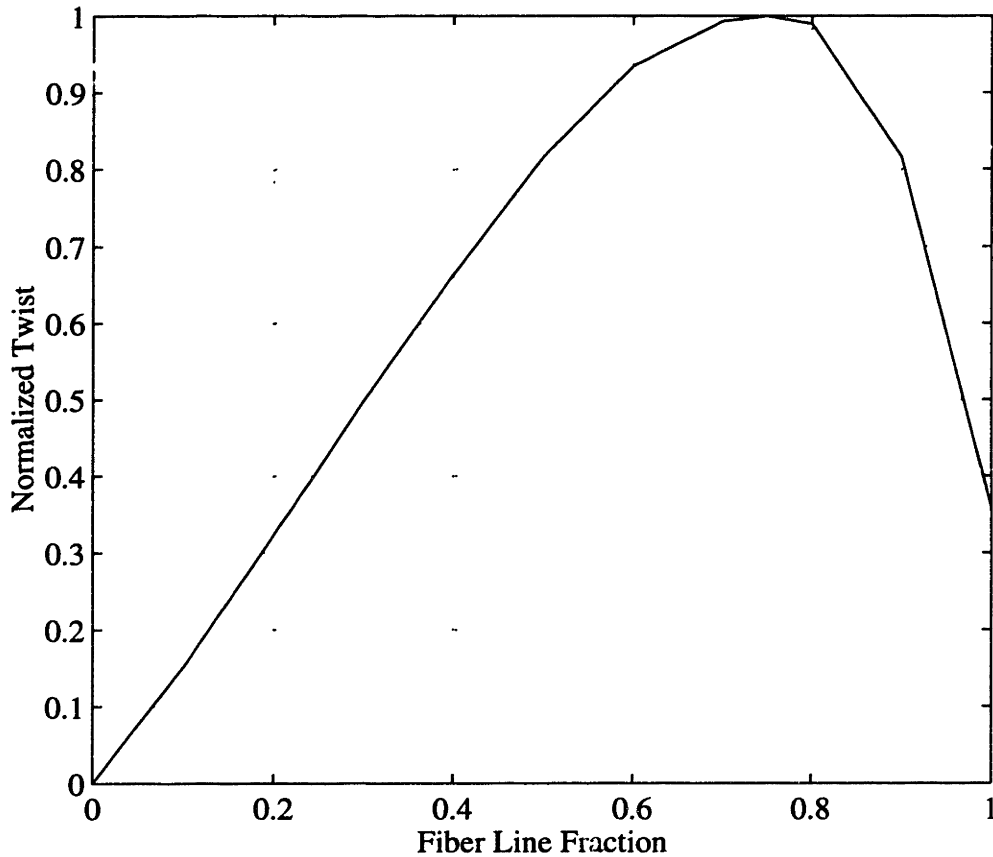


Figure 2-19. Optimal fiber spacing for twist actuation of plate.

2.4 SUMMARY

This chapter has provided a detailed explanation of the models used to predict the response of an adaptive plate to internal actuator forces. Beginning with a background description of piezoelectricity, the anisotropic PFC actuator was introduced. The linear model for piezoceramic actuators was discussed and the constitutive relations were expressed. A micro-electromechanical model was presented for predicting the effective properties of the PFC lamina. Then CLPT was implemented to model the active ply as a part of the greater composite laminate. An exact solution was given for a plate with free boundary conditions. A Rayleigh Ritz solution procedure using assumed shape functions was implemented. Finally, an adaptive plate experiment was designed using these models. An adaptive plate was constructed with a lay-up chosen to maximize the twist actuation. The following chapter will describe the manufacture of this plate as well as the component active plies.

CHAPTER 3

Adaptive Plate Manufacture

This chapter describes the manufacture of adaptive composite plates with embedded PFC active plies. First, the driving requirements in the development of the PFC prepreg manufacturing process are discussed. This includes previous work on the micromodeling of the PFC's. Next, each of the components of the PFC prepreg is described in detail, and preparations for assembly into an active ply are presented. The prepreg manufacturing process follows, covering the integration of the components and preparation for embedding. Finally, the embedding process, laminate lay-up, and cure are described, along with some preparations for experimental investigation into the actuation of the adaptive plate.

Two adaptive plates were manufactured, each containing two active plies. In the first plate, the fiber spacing parameter, x_2 , was 0.5. In the second plate, the fiber volume fraction was increased using a width line fraction of 0.75. This latter value was near the predicted optimal level for maximizing the piezoelectric induced shear constant of the ply. One additional difference between the plates was the incorporation of a degassing stage in the prepreg manufacturing process. This step was added to improve the quality of the actuators for the second plate. Further detail is provided in the following sections.

3.1 KEY MANUFACTURING ISSUES

The most significant factor effecting the geometry of the PFC is the dielectric mismatch between the fibers and matrix. The relative dielectric of the unmodified epoxy is a factor of one thousand less than that of the piezoceramic fibers. In a typical PFC, a thin layer of matrix will separate the fibers from the electrode surface. The result is that for any applied voltage across the electrodes, there is a large voltage drop across the thin layer of

matrix between the fiber and electrodes. A low field in the fiber results in less actuation at any given voltage, while the high field in the matrix limits the applied voltage levels due to dielectric breakdown. In general, this can be related to a series capacitance problem. The voltage drop across the fiber is a function of the ratio of the capacitances of fiber and matrix. The electric field in the fiber will be greatest when the matrix dielectric is high and the thickness of the matrix layer is very small. This is an extremely simple model of the phenomenon, but it is useful for gaining physical intuition into the problem.

A more detailed analysis was performed by Bent and Hagood [1994] using a finite element model. A quarter model of the fiber/matrix system was analyzed using the

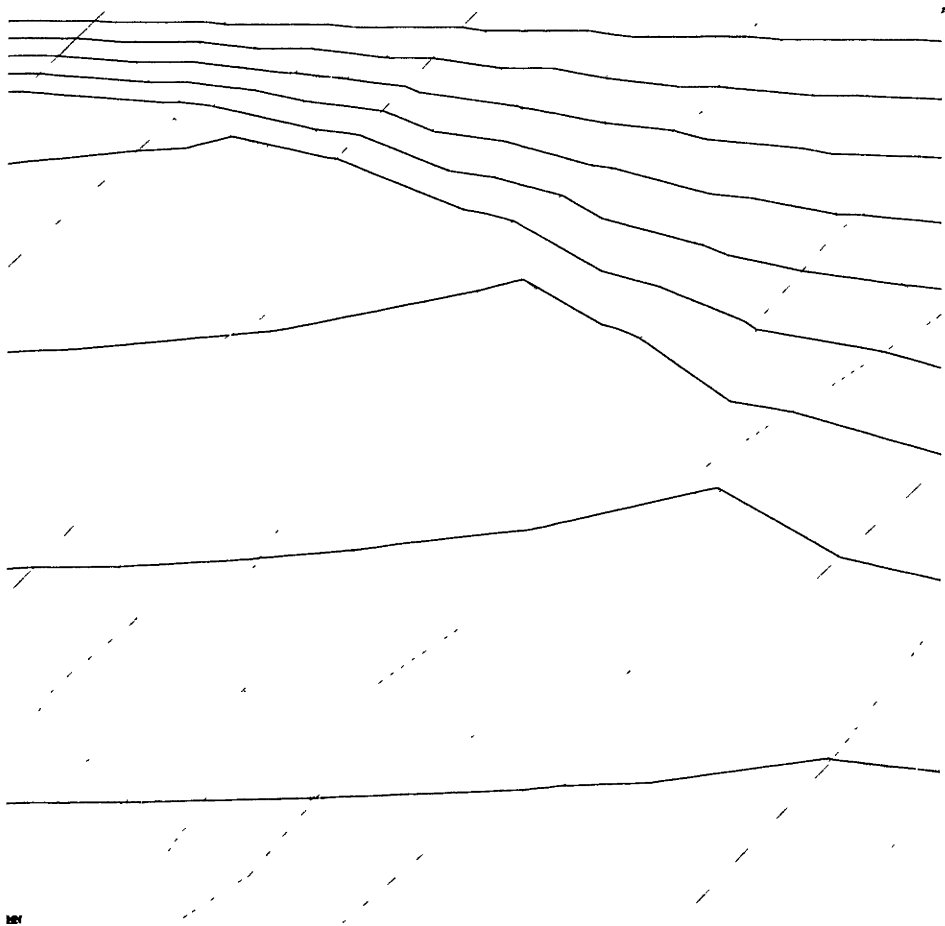


Figure 3-1. Electric field distribution in quarter model of fiber and matrix , $x_2=0.9$, $x_3=0.9$, $\epsilon_f/\epsilon_m=10$ [Bent and Hagood, 1994].

ANSYS² software package which supports multi-field elements and electromechanically-coupled materials. Tetrahedral elements were used. The resulting equipotential pattern is

² ANSYS 4.4, Swanson Analysis Systems, Houston, PA

shown in Figure 3-1 for a representative geometry. The gray lines are the finite element grid. As expected, the dark equipotential lines are very dense between the fiber and electrode, in the upper left region of the plot. The lines are more widely spaced in the fiber. Thus the electric field is higher in the matrix than in the fiber. In the distribution shown in the figure, the dielectric mismatch was 10. In actuality, the mismatch between the fibers and matrix is about 100. Thus the actual electric field distribution may be much more severe.

This analysis led to two manufacturing goals for the PFC prepreg. First, a high dielectric matrix was desired to reduce the dielectric mismatch and in turn improve the electric field distribution in the fibers. The second was to minimize the thickness between the fibers and electrodes. This compression minimizes the undesirable effects of the mismatch. In previous studies, the PFC was first manufactured without electrodes so that the top and bottom surfaces of the cured fiber/matrix layer could be sanded to remove the unwanted matrix layer [Hagood and Bent, 1993].

A second issue in the manufacturing process development was the void content of the matrix. Voids, or small pockets of air trapped in the matrix, can limit actuator performance and create reliability concerns. The low dielectric breakdown level in air (approximately 2400 V/mm) can limit the achievable field levels in the PFC. If this level is reached within a void, arcing can occur which damages the surrounding matrix and electrode. A possible consequence of this is that an electrical short circuit can occur, rendering the actuator inoperable. Laboratory experience has demonstrated that a slight reduction in performance results from most arcing, mostly due to electrode damage. Short circuits are more rare; however, the prevention of voids in the manufacturing process is a major goal for maintaining the integrity and reliability of the PFC actuators.

Another concern affecting the development of the adaptive plate manufacturing process is the method for embedding the active plies between the structural plies. Previous research has shown that the electrical insulation around the active components is critical [de Luis *et al.*, 1989]. De Luis embedded piezoceramic wafers in a graphite/epoxy laminate. The actuators and electrical leads were isolated from the surrounding structure because the graphite fibers were found to cause electrical shorts otherwise. The interlaminar electrodes used for the current manufacturing process were designed to address the electrical isolation and electrical leads required.

3.2 PFC COMPONENTS

The three major elements of the PFC prepreg are the piezoceramic fibers, the epoxy-based matrix, and the interlaminar electrodes. Each has been developed specifically for this application. An outside contractor developed the fibers to meet size and quality requirements. A standard epoxy resin system was modified with several additives in order to raise the relative dielectric while maintaining the manufacturability of the prepreg system. The electrodes were selected from existing materials, and then the conductive surface was patterned for the PFC application.

3.2.1 Fibers

The piezoceramic fibers were obtained from Cera Nova Company³. PZT5H-type fibers were selected to maximize the performance of the PFC actuators. The fibers are extruded in the green ceramic form, and are then cut in 3 to 4 inch lengths. Next, they are sintered. The diameter of the fibers was approximately 130 μm . Within each batch of fibers used in the manufacture of the PFC prepregs, the diameter was found to vary with a standard deviation of 4 μm . The grain size in the ceramic is on the order of 5 to 10 μm . Efforts have been made to avoid porosity in the ceramic and reduce grain size. The goal is to achieve bulk ceramic stiffness and strength properties in the fibers. Typical properties of bulk PZT5H are provided in Table 3-1. The actual stiffness properties for the fibers were experimentally determined and are provided in the next chapter.

Table 3-1. PZT5H Properties [Berlincourt *et al*]

Property	Value
s_{11}^E	16.5 pm ² /N
$\epsilon_{33}^T / \epsilon_0$	3400
d_{31}	-273 pm/V
coercive field	650 V/mm
Curie temperature	195 °C
density	7500 kg/m ³
maximum strain	0.03 %
bandwidth	1000 Hz
hysteresis	10 %
k_{31}	-0.39
energy density	820 J/m ³

³ Cera Nova Corp., Hopedale, MA

Values for the coercive field level and maximum performance metrics were calculated using data from previous studies of PZT5H [Chan and Hagood, 1994]. The hysteresis of the piezoceramic is an important measure of efficiency in energy usage. The coupling factor describes the ratio of electrical work in to the sum of the electrical work and the resulting mechanical strain. It is defined:

$$k_{31}^2 = \frac{d_{31}^2}{\epsilon_3^T \delta_{11}} \quad (69)$$

The energy density represents the energy stored in the applied field which can be converted to mechanical strain:

$$U_p = \frac{1}{2} \epsilon_3^T (k_{31} E_{\max})^2 \quad (70)$$

where E_{\max} is the maximum applied electric field for typical operation (~600 V/mm).

3.2.2 Hybrid Matrix

The first step in the development of the matrix material for the PFC prepreg was the selection of the epoxy resin system. In order to enable maximum conformability during the laminate lay-up procedure for composite structures, a prepreg form was desired. This required a B-staged epoxy, which may be held in an uncured, intermediate stage of the thermosetting reaction process [Skeist, 1962]. At this stage, the resin may be tacky, but maintains a solid form at room temperature. The goal was to manufacture a PFC prepreg with the epoxy in a B-stage or prepreg form to be laid-up with structural host prepreg plies and then cocured. Thus the cure cycle of the resin was required to be compatible with the common Hercules graphite/epoxy prepreg resin, 3501-6, cure cycle [Hercules]. This consists of one hour at 115 °C followed by two hours at 176 °C.

The desire for a high dielectric matrix placed a further constraint on the epoxy resin system. In order to raise the relative dielectric of the epoxy, a high dielectric particulate filler was to be added. The doped matrix would then be added to the fibers to form the prepreg; however, the addition of the filler greatly increases the viscosity of the matrix, which creates significant difficulties in the manufacturing process. Thus a low viscosity epoxy was desired to enable greater volume fractions of filler to be added while maintaining a final viscosity low enough to allow for integration with the brittle ceramic fibers.

A common composite filament winding resin system was selected for the PFC prepreps [Boll, 1994]. Shell Epon 9405 resin with Epi-Cure 9470 curing agent⁴ was

⁴ Shell Chemical Co., Short Hills, NJ

obtained and evaluated. This is a modified bisphenol-A epoxy resin with an amine curative. It is a structural epoxy with high stiffness, low viscosity, high gel temperature, and B-stage capability. The properties of the unmodified epoxy with a 100:37 mix ratio are listed in Table 3-2.

Table 3-2. Properties of Epon 9405/Epi-Cure 9470 resin system [Shell].

Young's modulus	2.95 GPa
viscosity	1100 cps
pot life	34 hours
gel temperature	176 °C
density	1050 kg/m ³
relative dielectric	5

In order to alleviate the problem of dielectric mismatch between the high dielectric fibers and low dielectric epoxy matrix, a high dielectric powder was added to the epoxy. The powder used was a 1 μm PZT5H powder⁵. The properties of the powder are nearly identical to those listed for the PZT5H in Table 3-1. To aid in the uniformity of particle dispersion, a dispersing agent called Hypermer⁶ was also added. This dispersant is a form of surfactant which deters particles from conglomerating in the mixture. The amount of powder added was limited by the maximum workable viscosity of the matrix. This was heuristically determined to be approximately 1000 cps at 100°C. At room temperature, the viscosity was roughly two orders of magnitude larger. A fraction of 83% of PZT powder by mass of the total matrix (42% by volume) was the maximum powder content in acceptable samples. Higher volume fractions and viscosity prevented adequate compression during manufacture and increased the incidence of broken or misaligned fibers. This mixture included dispersant, which was 2% of the powder mass. The amount of dispersant was selected from experimental data to optimize the viscosity and dielectric properties while maintaining adequate stiffness. A second form of surfactant, an air release additive⁷, was also added to the mixture. It lowers the surface tension of the epoxy, allowing trapped bubbles to escape more easily. It was incorporated in the amount of 2% of the epoxy mass, which was the recommended concentration.

The matrix for the prepreg was prepared in batches starting with 4 g of epoxy each. Each batch was mixed in two stages to obtain the best dispersion results. First, a mixture

⁵ Morgan Matroc, Inc., Bedford, OH

⁶ ICI Surfactants, KD-2, Wilmington, DE

⁷ BYK-Chemie A530, Wallingford, CT

containing 80% of PZT powder by mass of the total mixture was made. Then, additional powder and dispersant were added to attain the 83% content. The first step in the mixing process was to combine parts A and B of the epoxy in the ratio of 100:37, and then stir in the dispersant and air release additive for one minute. The powder was added and mixed in with a mortar and pestle for three minutes at 63°C. The elevated temperature helped to reduce the viscosity of the mixture, enabling easier and more effective distribution of components. The mixture was then ultrasonically excited⁸ for 5 minutes at 100°C to disperse the powder. The remainder of the PZT powder was next added along with the remaining 2% dispersant. This was mixed for 3 minutes with the mortar and pestle, and 5 minutes with the sonicator. The experimental value of the relative dielectric of the doped matrix was 23, which was a factor of five improvement over the pure epoxy.

Another issue with the matrix is the B-stage consistency, sometimes referred to as the tack and drape of the prepreg. The B-stage is not a specific point in the polymerization process; the properties of the B-stage can vary significantly depending on the time and temperature history of the epoxy. For a typical prepreg, the epoxy should be pliable and somewhat tacky at room temperature. Since the PFC prepreg is surrounded by electrode material, the tack is not important. An experimental investigation was used to determine that an adequate B-stage was obtained after 90 to 100 minutes at 95°C. The same consistency could be achieved after roughly a week at room temperature as was recommended by Shell, but the faster schedule was preferable. The matrix adhered fairly well to the electrodes in this condition, although the electrodes could be peeled.

3.2.3 Interlaminar Electrodes

Two types of interlaminar electrode materials have been used in the manufacture of PFC's. Initially, a Kapton⁹ electrode material with a copper layer sputtered on one side was used. This copper/Kapton electrode was 12.5 μm thick and was obtained from Southwall Technologies¹⁰. A problem arose with the current Epon resin system selected for the prepreg manufacture. The amine curing agent was chemically incompatible with the copper: the reaction of the copper and the amine forms a brittle compound which inhibits adhesion. One possible solution under investigation is the pretreatment of the copper surface to form an oxide layer [Wegman, 1989]. The epoxy would bond to this intermediate layer, avoiding the copper reaction.

⁸ Sonics and Materials, Vibracell VC-50, Danbury, CT

⁹ DuPont Kapton Polyimide Film, Wilmington, DE

¹⁰ Southwall Technologies, copper/Kapton, Palo Alto, CA

A short-term solution to the problem was to switch to a silver/polyester electrode material¹¹. A 25 mm thick material was selected. This material is thicker which is a disadvantage in that load transfer between the actuator and the host structure is less effective. In addition, the polyester and silver may not withstand the high cure temperatures as well. All experiments in this thesis utilize the silver/polyester electrodes.

In order to prevent possible short circuit paths from forming between the various electrode layers in the laminate, a special electrode pattern was developed. The conductive graphite plies tend to migrate over the edges of the laminate during the cure. In addition, high voltage differences exposed to open air create dielectric breakdown risks at the edges. A ferric chloride solution was used to etch the silver from the electrode around the edges, leaving a 3 mm border. At the shorter sides (the ends) of the electrode, a single conductive strip was left to serve as electrical leads for establishing connections in the finished laminate. Four isolated leads were required for the four embedded electrodes. The etch pattern used is diagrammed in Figure 3-2 for an upper and lower electrode pair. Dashed lines show the extent of the laminate, while shading denotes the upper and lower conductive flaps at the ends. A conductive path was left at both ends for redundancy.

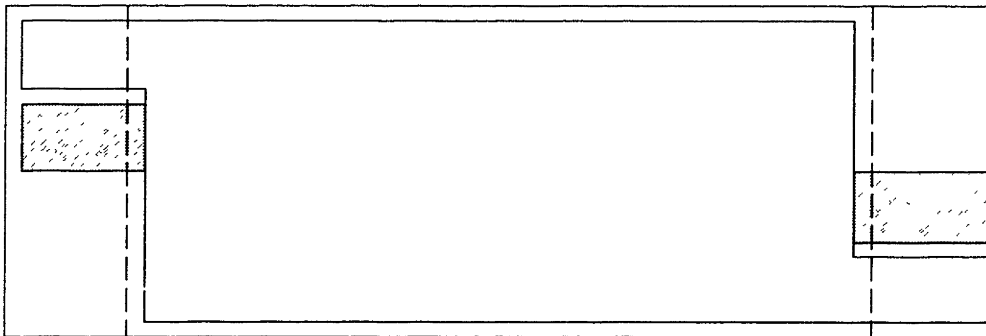


Figure 3-2. Etched electrode patterns with end flaps for upper (light) and lower (dark) layers.

3.3 PREPREG MANUFACTURING PROCEDURE

The procedure for PFC prepreg manufacture can be divided into four major steps:

1. Mold Construction
2. Fiber Preparation and Alignment
3. Matrix Addition
4. Compression and Staging

¹¹ Southwall Technologies, Silver Reflector II, Palo Alto, CA

First the mold must be prepared. Then the fibers must be prepared and aligned in the mold. Next the matrix is added to the mold and the electrodes are affixed. Finally, the prepreg is compressed and staged to achieve the desired qualities. The entire procedure was developed through heuristic studies using more advanced prepreg tape manufacturing methods as a model.

3.3.1 Mold Construction

The first step in the procedure for prepreg assembly was to affix the lower electrode to a flat aluminum plate using flash tape¹² and a light coat of spray adhesive¹³. The adhesive helps to keep the lower electrode from wrinkling which can disturb the fiber layout procedure. This adhesive can be dissolved in Methyl Ethyl Ketone (MEK) solvent when removing the finished prepreg from the plate. Contact with the uncured epoxy in the prepreg is avoided during this removal process. Next, two 1.5 cm strips of 0.375 mm Teflon (or 0.125 mm stainless steel) were attached along the sides of the electrode using double-sided Kapton tape¹⁴. The strips, which were 30 cm long, were spaced 6.7 cm apart to allow for excess matrix to escape along the edges of the 6.35 cm wide top plate during the compression stage. The strips were taped over with flash tape, and alignment marks were made at a 45° angle for each of the bundles of 50 fibers. Since the fibers were aligned at 45°, both ends of the mold had fibers extending beyond the 15.2 cm length of the prepreg as shown in Figure 3-3.

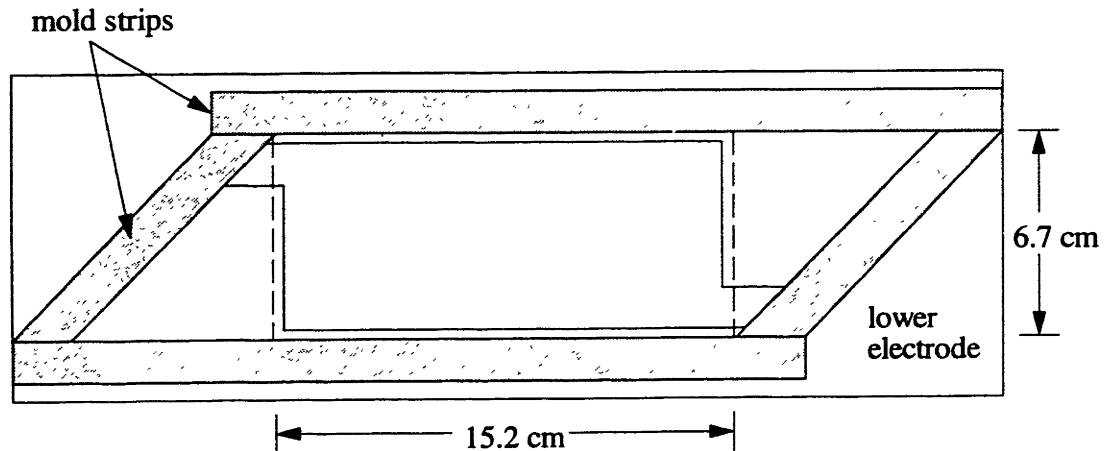


Figure 3-3. Mold for PFC prepreg assembly.

¹² Northern Fiberglass Co. Inc., flash tape, Hampton, NH

¹³ 3M, Spray Mount, St. Paul, MN

¹⁴ Northern Fiberglass Co. Inc., double-sided Kapton tape, Hampton, NH

3.3.2 Fiber Lay-Out

The fibers were first trimmed to 7.62 cm lengths. The total number of fibers for a prepreg with a 0.5 line fraction (x_2) of fibers is about 600. A 0.75 line fraction requires about 900 fibers. The fibers were separated into groups of 50 for transfer to the mold. The fibers bundles used for one of the PFC prepreps is shown in Figure 3-4. Each fiber

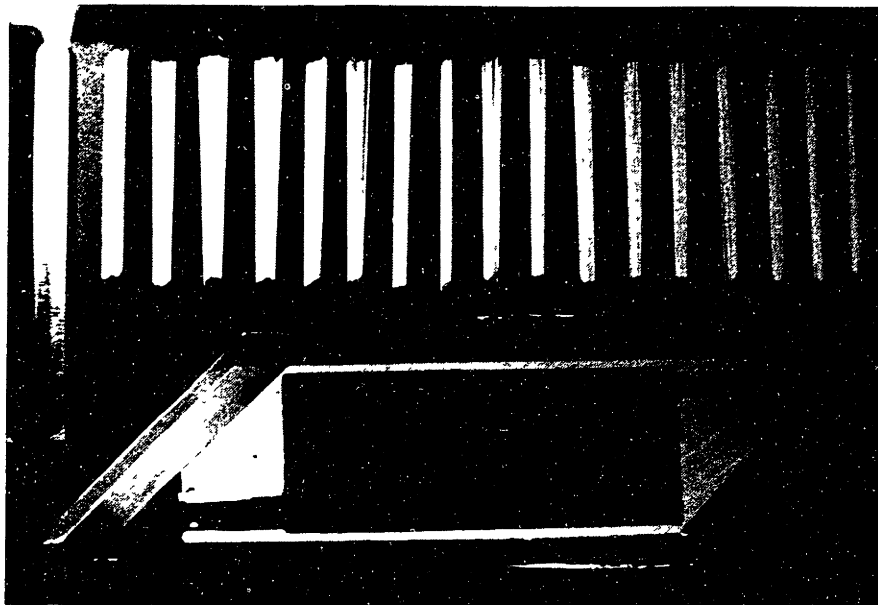


Figure 3-4. Photograph of PZT fiber bundles prepared for transfer to mold.

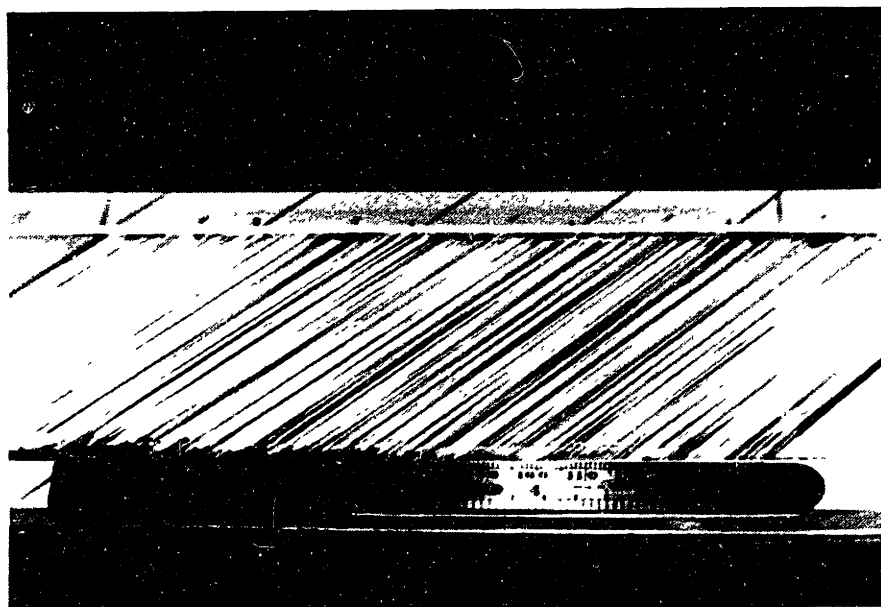


Figure 3-5. Completed mold assembly containing fibers ($x_2=0.5$).

bundle was transferred to the mold, rotated to the proper angle, and then spread evenly between the alignment marks. The completed mold assembly with aligned fibers is illustrated in Figure 3-5. The entire fiber preparation and alignment procedure was completed in about one hour.

3.3.3 Prepreg Assembly

Once the mold has been constructed and filled with the fibers and the matrix has been mixed, the components can be brought together to form the PFC prepreg. In order to reduce the matrix viscosity for the integration process, the premixed matrix and the mold were preheated to 95°C. The low viscosity is essential for attaining uniform matrix distribution over the fibers. In addition, viscous forces may misalign the fibers. The mold temperature was maintained on a hot plate. Once heated, the matrix was poured slowly into the mold, making stripes along the length as shown in Figure 3-6. The goal was to add as little matrix as necessary to completely cover all the fibers. Total coverage was not achieved immediately; the matrix was allowed to distribute itself slowly over a period of 10 to 15 minutes. A thin strip of teflon (0.375 mm) was used to gently assist in the spreading process, pushing the matrix material in a direction parallel to the fibers.

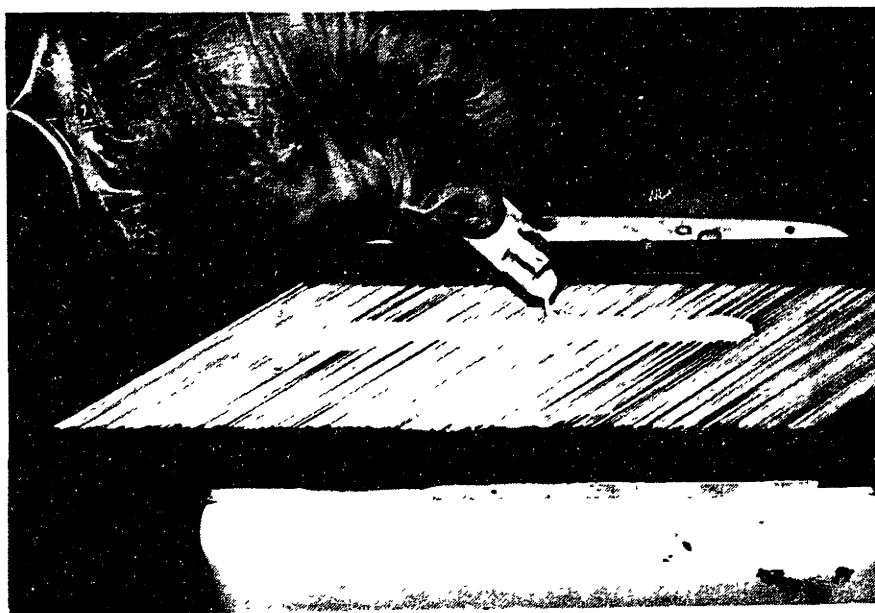


Figure 3-6. Matrix material being added to mold assembly containing fibers.

With the matrix fairly uniformly distributed, the mold was transferred to a small cure plate for a degassing procedure. This procedure was intended to release any gases which may have been trapped in the matrix during the mixing process or bubbles which may have been trapped around the fibers. The removal of these gases was essential for

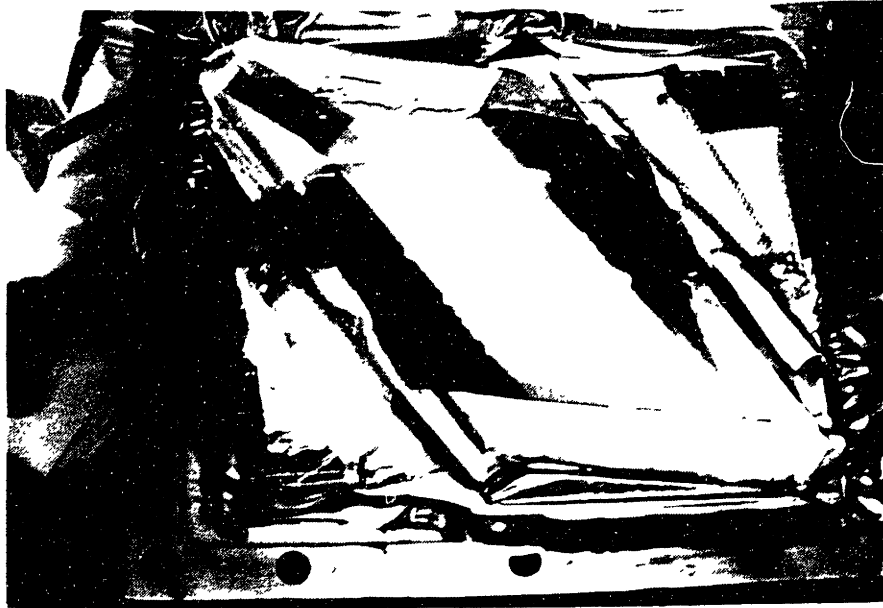


Figure 3-7. Vacuum bag assembly for degassing matrix.

avoiding voids in the completed PFC. In lieu of a bell jar, a standard vacuum bag was used to attain a 100 kPa vacuum (30 in. Hg). This was accomplished using a 2 cm stack of cork strips around the perimeter of the mold covered with a 1.27 cm thick plexiglass plate. This allowed the degassing process to be monitored through the bag in addition to preventing any contact with the fibers and matrix. Figure 3-7 shows the degassing arrangement. The entire cure plate was maintained at 95°C with the vacuum for 15 minutes. During this time, bubbles rose to the surface and eventually broke.

Next, the mold was removed from the vacuum bag and returned to the hot plate. The thin teflon strip was then used to slowly and carefully scrape excess matrix over the sides of the mold. The excess was pushed in a direction parallel to the fibers to maintain the fiber alignment. The removal of excess matrix helps to maintain fiber alignment during the compression stage, where excess matrix is pushed out, possibly taking fibers with it. Just enough matrix is left to completely cover all of the fibers.

Finally, the top electrode was applied to the fiber/matrix layer in the mold. The electrode was lightly brushed onto the fiber/matrix layer from the center outward, with care taken to avoid trapping any air on the surface. A thicker teflon strip (0.625 mm thick) was then used to gently push out any remaining excess matrix, moving slowly along the fibers and from the center outward. The top etched pattern on the top electrode was also aligned with the lower electrode pattern. A photograph of the mold with the top electrode in place is shown in Figure 3-8. The edges of the top electrode were fixed with flash tape to

prevent movement during the compression stage. Then the 12.7 mm thick aluminum top cover, with dimensions of 15.2 cm by 6.35 cm, was aligned with the top electrode pattern and placed on top of it.

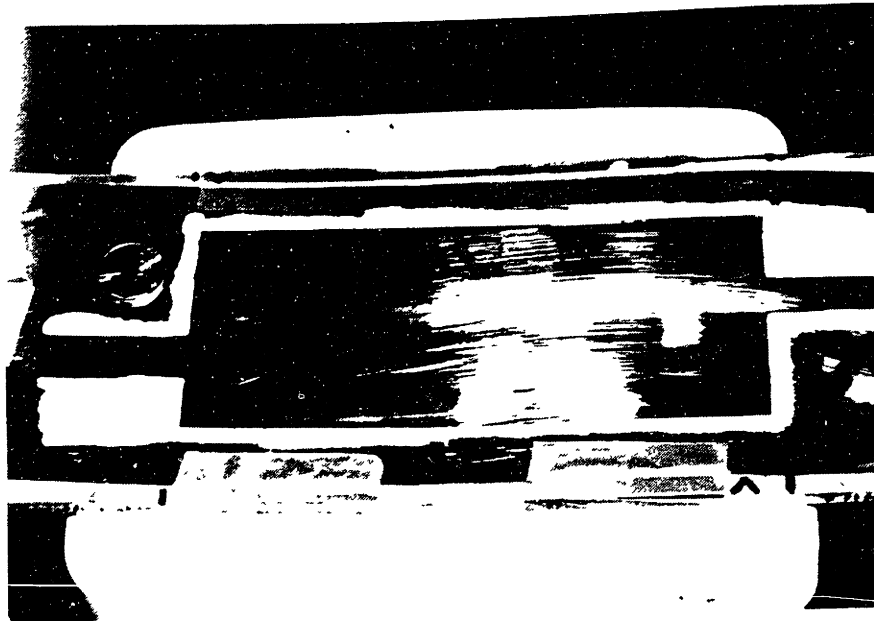


Figure 3-8 Mold containing fibers, matrix, and electrodes.

3.3.4 Compression and Staging

The compression stage of the PFC prepreg manufacturing process consists of gradually applying uniform pressure to the top cover while maintaining the temperature at 95°C. In order to apply uniform pressure to the top cover, two layers of 12.7 mm silicon rubber were stacked on top, followed by an additional aluminum top plate. Then six 7.6 cm C-clamps were positioned around this top plate and light pressure was applied, as shown in Figure 3-9. The entire assembly was transferred to a 95°C oven to complete the compression and B-staging processes.

The clamps were tightened after 10 minutes, and then tightened again after another 10 minutes. The final pressure achieved was about 275 kPa (40 psi). This was determined from a calibration test of the compression assembly using a force transducer. The prepreg was left in the oven long enough to complete the staging process. This required a total of 100 minutes at 95°C, starting with the filling of the mold. When this time limit was reached, the assembly was removed from the oven and then cooled to room temperature. The sides were trimmed so that the prepreg had a width of 6.35 cm. The electrodes were peeled back from the triangular ends to uncover the excess fiber/matrix area previously

described. This section was scored and removed. The electrode flaps at the ends were trimmed to a length of 2.5 cm. Figure 3-10 is a photograph of a finished prepreg.

For some of the PFC characterization tests described in the next chapter, unconstrained PFC's were manufactured. Rather than laying-up the prepreg to form a laminate, it is cured by itself using the same compression/staging set-up shown in Figure 3-9. In order to protect the conductive surfaces of the electrode flaps from being covered

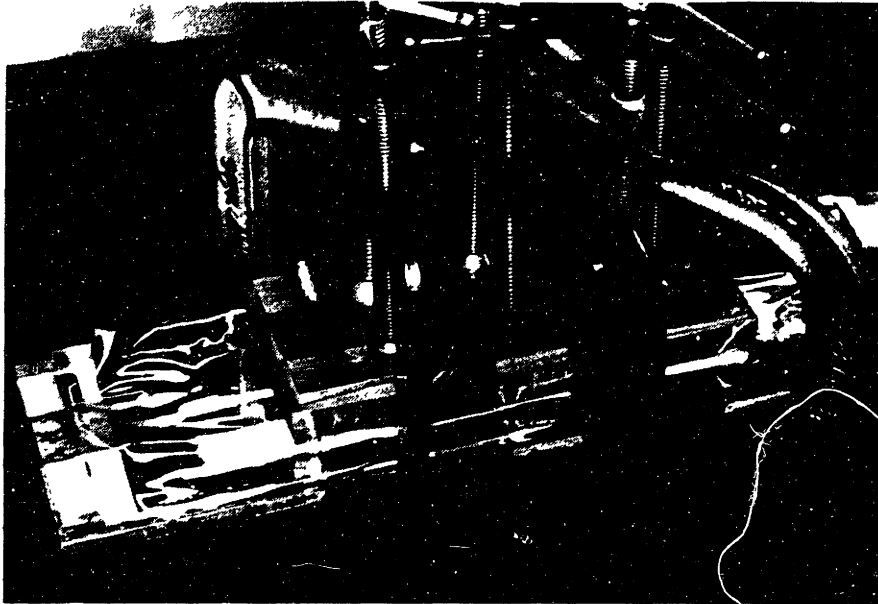


Figure 3-9. Prepeg compression and staging assembly.

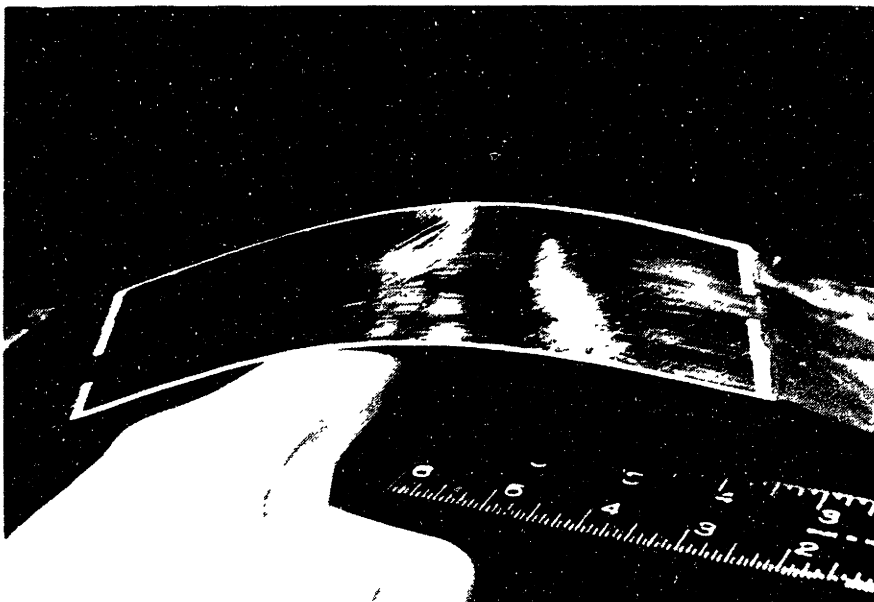


Figure 3-10. Conformable PFC prepreg.

with excess matrix, the surfaces are covered with Kapton tape before the cure. Then the entire assembly is cured at 275kPa, with no vacuum bag, following a cure schedule of one hour at 115°C followed by two hours at 177°C. This is similar to the cure for the adaptive plates described in the next section.

3.4 ADAPTIVE PLATE MANUFACTURE

The PFC prepregs were stored until the adaptive plate manufacturing process began. The prepregs remained flexible during this period of several days. The lay-up procedure and cure used for the adaptive plate were based on standard techniques developed for graphite/epoxy laminates. Several modifications required for the active laminae will be described.

3.4.1 Lay-Up

The adaptive plates manufactured were 5-ply laminates containing a pair of PFC actuators and three host plies. Graphite/epoxy AS4/3501-6 prepreg tape¹⁵ from Hercules was used for the host material. The prepreg contained 39% resin. The lay-up selected was $[90/45_A/0/-45_A/90]_T$, as described in the previous chapter. The graphite plies were cut from the prepreg tape. The 5 plies of the laminate are shown in Figure 3-11 prior to the actual lay-up.

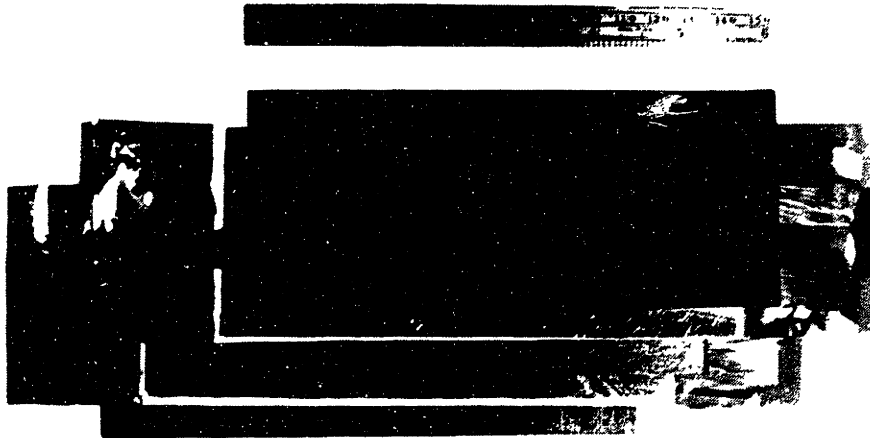


Figure 3-11. Adaptive plate laminae.

¹⁵ Hercules Inc., Wilmington, DE

In preparation for the lay-up, the outer surfaces of the electrodes on the active plies were cleaned with MEK. Then the plies were assembled beginning with the bottom 90° ply. Each ply was aligned and then pressed and smoothed firmly to remove any air trapped between the plies. The laminate was then sandwiched between two sheets of release film¹⁶, cut to extend 2.5 cm beyond each side.

3.4.2 Cure

In order to protect the electrode flaps from the 3501-6 resin during the cure, 0.049 mm Kapton tape¹⁷ was applied over each conductive area. Small pieces of 0.083 mm thick guaranteed non-porous teflon (GNPT) with dimensions of 6.35 cm by 2.5 cm were placed between each of the four electrode flaps at each end. This is illustrated in the enlarged view of the cure assembly in Figure 3-12. The GNPT was used to prevent the electrode flaps from adhering to each other. The flaps and GNPT sheets were completely sealed with the Kapton tape.

Preparations were made for a standard net resin cure. This type of cure was selected because of the relatively low resin content of the graphite prepreg. The intent of the cure assembly was to contain all resin. The release film surrounding the laminate was non-porous; all other layers in the assembly were GNPT. A cross section and top view of the cure assembly are illustrated in Figure 3-12. The sealed electrode flaps at the ends of the laminate were allowed to remain extended rather than being folded into the outer GNPT package. The ends of the GNPT package were sealed with flash tape. The top plate was again 6.35 mm thick aluminum. The cure assembly was constructed on a standard aluminum cure plate. Cork strips were used to frame the laminate and hold the top cover in place. At the ends, the cork strips were placed over the electrode flaps, which were already sealed in kapton tape.

The autoclave cure was accomplished in the Technology Laboratory for Advanced Composites (TELAC) at MIT. The cure plate was covered with porous teflon and fiberglass cloth. A vacuum bag was applied. The vacuum pressure was 30 inches of mercury. A photograph of the cure plate in the autoclave is shown in Figure 3-13.

The standard 3501-6 cure cycle was used to cure the laminate. The cycle consisted of 1 hour at 115°C and 2 hours at 177°C, which is also sufficient for curing the Epon resin. The heating and cooling rates were $\pm 3^\circ\text{C}$ per minute. During the first stage, the pressure was held at 585 kPa (85 psig) with the vacuum. Then the vacuum was released and the pressure was raised to 690 kPa (100 psig). This was recommended to allow any

¹⁶ Northern Fiberglass Co. Inc., FEP A5000 release film, Hampton, NH

¹⁷ Northern Fiberglass Co. Inc., Kapton tape, Hampton, NH

trapped bubbles to collapse to a smaller volume. Then the temperature was raised to 177°C. Following this cure cycle, the laminate was removed from the cure plate and placed in another oven for a 6 hour postcure at 177°C to ensure a complete cure was achieved.

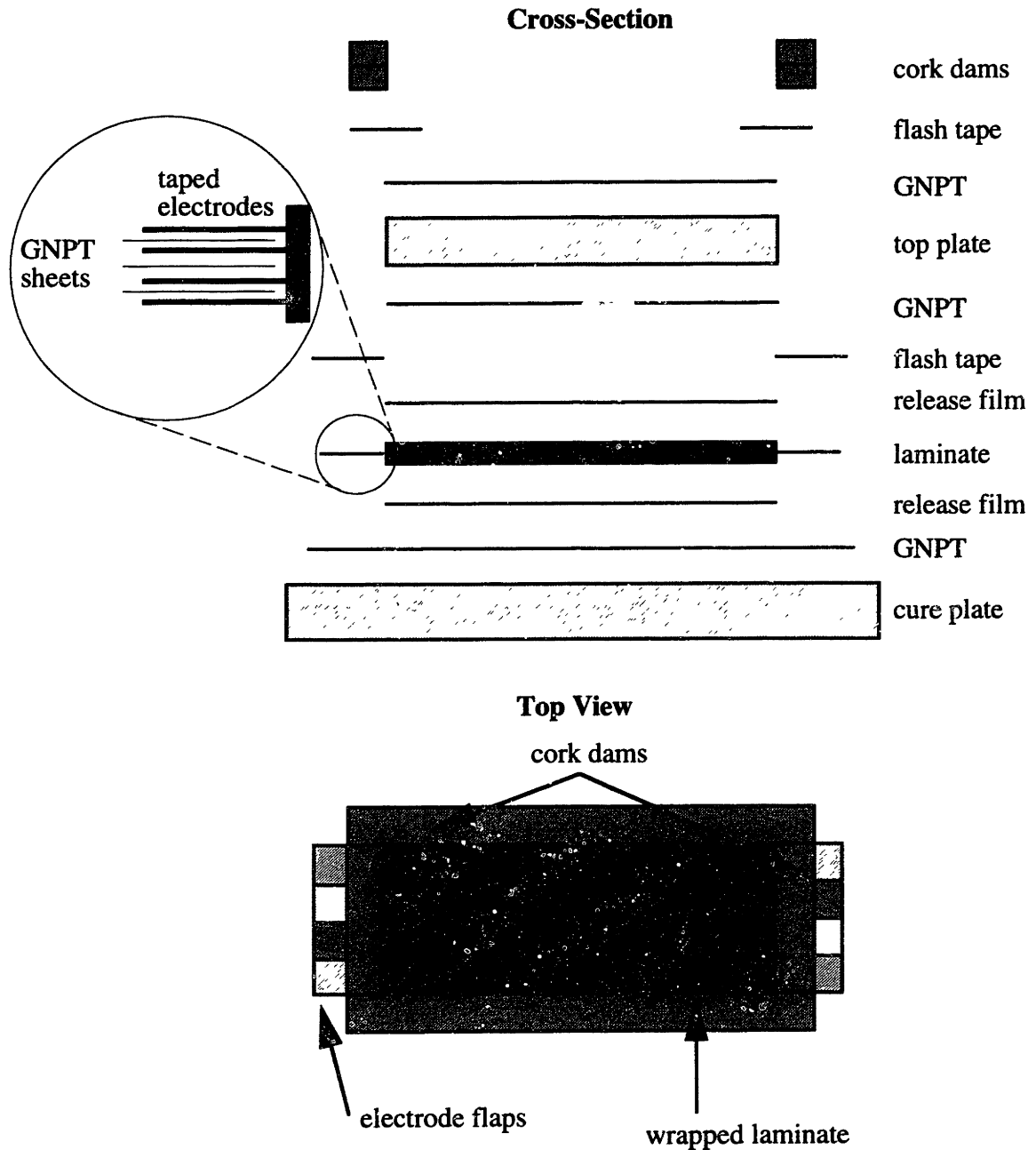


Figure 3-12. Cure assembly cross section and top view with electrode flaps extended.

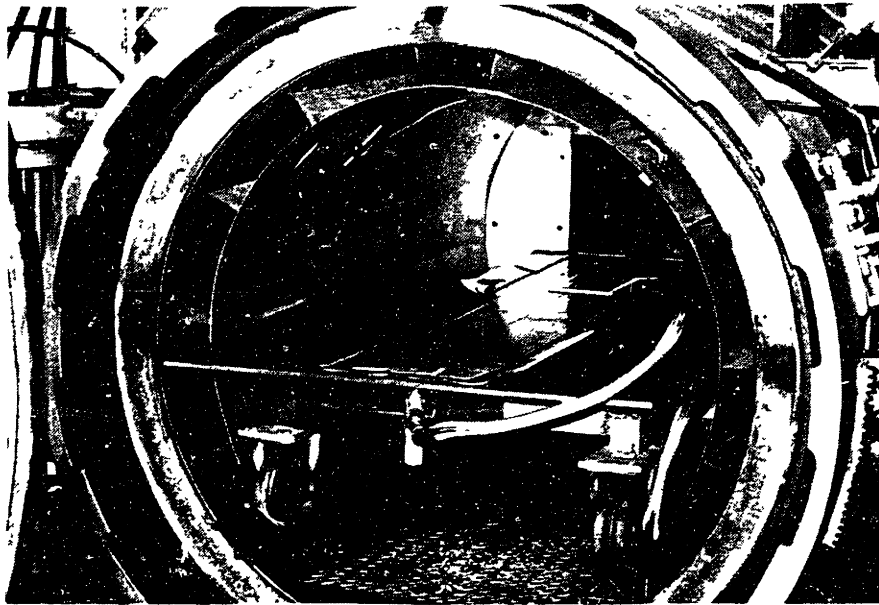


Figure 3-13. Cure plate assembly in autoclave

3.4.3 Thermal Stresses

Because the laminate was cured at 177°C, but will be operated at room temperature (20°C), thermal stresses are developed within the laminae. For the antisymmetric laminates manufactured for this research, the thermal stresses result in an initial deformation of the plate. The $\pm 45^\circ$ active plies create a twist in the laminate. In addition, any slight imbalance between plies above and below the centerline of the plate result in bending, most notably along the longitudinal axis. Both adaptive plates manufactured have a significant "pretwist" and also a slight "prebend" as a result of the thermal stresses. The twist resulted from the antisymmetric lay-up, while the bending resulted from some slight asymmetry in ply thickness or other property.

The thermal stresses in the adaptive plate create stresses in the piezoceramic fibers within the active plies. Since the fibers are composed of a brittle ceramic, the stress levels need to be estimated in order to evaluate the state of the fibers. Significant stress levels may create fractures in the fibers which will alter the effective properties of the active plies.

In order to find the stresses in the active fibers, the adaptive plate model was used to simulate the thermal deformation of the plate. In the model, the piezoelectric d-constants were replaced with coefficients of thermal expansion, α_1 and α_2 , for each ply, including the graphite/epoxy plies. The applied electric field was replaced with the change in temperature, ΔT . The temperature change was -155°C, assuming that the epoxy cured in the laminate at 177°C in a stress-free condition. The values of the coefficients are provided in Table 3-3 [Hercules, Piezo Systems]. The transverse coefficient for the active plies was

initially estimated from referenced values for the piezoceramic and an unmodified epoxy. The transverse coefficients are rather large due to the epoxy properties. The calculation was performed for the second plate although the first plate has similar values. The bending curvature was assumed to have a negligible contribution.

Table 3-3. Coefficients of Thermal Expansion for the Adaptive Plate Laminae.

	Gr/E	PFC
α_1 ($^{\circ}\text{C}^{-1}\cdot 10^{-6}$)	-0.09	4.0
α_2 ($^{\circ}\text{C}^{-1}\cdot 10^{-6}$)	27	12

The actual plate had a measured twist curvature of approximately 30 deg/m while the model predicted 28.5 deg/m. The distance from the laminate centerline to the center of the +45° active ply is 0.16 mm. The strain in the laminate resulting from the thermal stresses was found from the plate model. These are the strains in the laminate coordinates. A rotation to the lamina coordinates can be used to find the strains along the fibers:

$$\tilde{S}_1 = S_1 \cos^2 \theta + S_2 \sin^2 \theta + 2S_6 \sin \theta \cos \theta \quad (71)$$

where θ is -45° for a clockwise rotation. The calculated strain along the fibers was -390 microstrain. The stress in the fibers was then be approximated as

$$\tilde{T}_1 = (\tilde{S}_1 - \alpha_1 \Delta_T) / s_{11}^E \quad (72)$$

The resulting stress was 13.9 MPa. This is significantly less than the failure stress for pure PZT; however, the strength of the fibers may not be the same as the bulk value, which is 63 MPa in static tensional tests [Piezo Systems].

3.4.4 Preparation for Testing

The edges of the cured laminate were lightly sanded to remove excess resin. The electrode flaps were separated and a small conductive area was exposed on each flap. Electrical connections were established using 34 gage wire connected with Epotek 410E conductive epoxy¹⁸. The conductive epoxy was cured at 100°C for one hour. Leads were attached only at one end of the plate; the flaps at the other end remained sealed for back-ups. One portion of the plate edge was polished and then photographed through a microscope. A photomicrograph of the edge of the plate is shown in Figure 3-14.

¹⁸ Epoxy Technology, Inc., Billerica, MA

The PZT fibers appear elliptical because the cross-section is at a 45° angle with respect to the fibers. Transverse cross-sections of the small graphite fibers are visible in the outer plies.

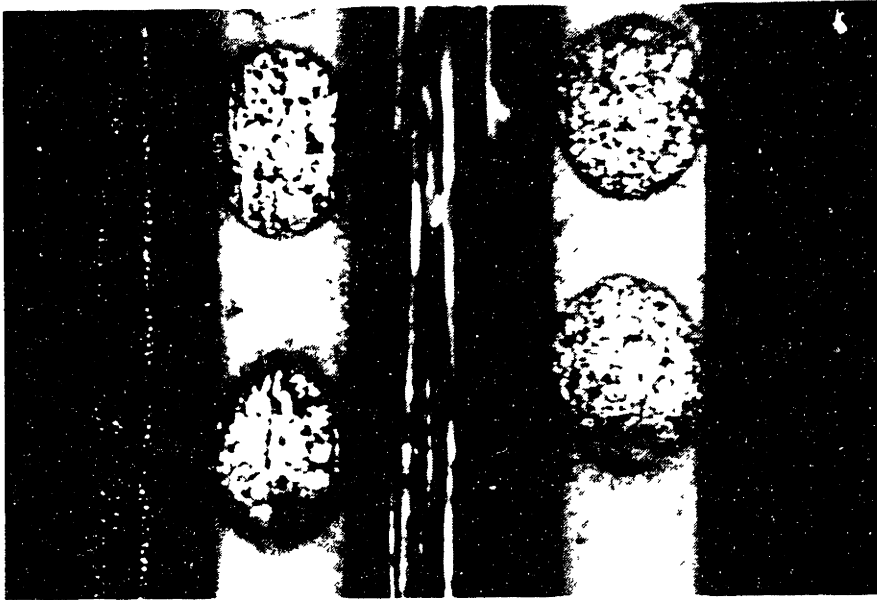


Figure 3-14 Photomicrograph of adaptive plate edge (50x)

3.5 SUMMARY

This completes the description of the adaptive plate manufacturing process. First, the major manufacturing process requirements were presented, from which the methods described were developed. The preparation of the fiber, matrix, and electrodes was presented. The components were then integrated in the prepreg manufacturing section. Finally, the active prepreg plies were embedded in a graphite laminate to form the adaptive plate. Two adaptive plates were manufactured using this procedure. The plates were then tested as is described in the next chapter.

CHAPTER 4

Experimental Results

The adaptive plates were tested in order to demonstrate actuation capabilities and to evaluate the models. First, data from free PFC actuators were used to characterize the properties of the active plies. Several unknown properties of the component materials were measured experimentally. In addition, error bounds were placed on the DUF model predictions for the effective properties of the PFC's. Mechanical stiffness and dielectric tests served these purposes.

Next, independent control of bend and twist actuation of an adaptive plate was demonstrated. Transfer functions from an input voltage to the plate response were measured to determine natural vibration modes for comparison to the model. Then, the actuator-induced deflections of the adaptive plates were compared to model predictions in single ply, bending, and twisting operating modes.

Unmodeled, nonlinear trends evident in the adaptive plate data are characterized from plate data and free PFC data. First, the typical high electric field nonlinearity in piezoceramics is demonstrated. Then the frequency dependence is addressed through an analysis of the phase relationship between the electric field applied to a PFC and the resulting electrical displacement.

Finally, a comparison with a hypothetical, perfect composite actuator is used to evaluate the performance of the PFC actuator. The perfect actuator has fibers with the ideal properties of PZT5H bulk ceramic embedded in an unconstraining, high dielectric matrix. The DUF and Rayleigh Ritz models are used to predict the actuation capabilities for the perfect composite for comparison with the adaptive plate data.

4.1 EXPERIMENTAL PROCEDURES

Once the manufacture of a free PFC or adaptive plate was completed, its dimensions and capacitance were recorded. Next, each PFC was wired and then poled. Actuation experiments for free PFC's generally involve measuring strain,. For the adaptive plates, the tip displacements are measured. Additionally, both the voltage and the current delivered to the PFC's were monitored. A function generator provided the periodic waveform for the voltage applied to the PFC's. A high voltage amplifier was used to magnify this signal. Transfer function data was acquired using a random noise signal. The following subsections will describe the details of the major experimental set-ups.

4.1.1 PFC Testing

Unconstrained PFC's were tested in order to better characterize their actuation. The PFC's were manufactured in a 2.54 cm square size using prepreg tape which was cured as described in Section 3.3.4. Longitudinal (along the fibers) and transverse (perpendicular to the fibers) strains were measured using surface mounted strain gages. T-gages¹⁹ were applied using a cyanoacrylate adhesive²⁰ to the center of each PFC tested. The output of a Vishay 2120A dual-channel signal conditioner²¹, which was proportional to the strain, was measured with a data acquisition system. Each strain gage channel was configured in a wheatstone bridge with an active gage on the sample being tested, and a second dummy gage in the test environment. This served to cancel out any environmental effects on the measurements.

The data acquisition system used for all measurements consisted of LabView 3 software²² and a National Instruments NB-MIO-16 data acquisition card²³ connected to a Macintosh Quadra 950 computer²⁴. The software was used to configure a virtual instrument which controlled up to 16 channels from the input card. Output channels were also available. The virtual instrument included oversampling and a fourth order butterworth filter to reduce high frequency noise in the data. The maximum sampling rate of 50 kHz was used for most data collection.

A Philips function generator²⁵ was generally used to provide the voltage signal for actuating the PFC's. This signal was fed through either a Trek high voltage amplifier²⁶ or

¹⁹ Measurements Group, type CEA-06-125UT-120, Raleigh, NC

²⁰ Measurements Group, M-Bond Adhesive, Raleigh, NC

²¹ Measurements Group, Model 2120A, Raleigh, NC

²² National Instruments, Austin, TX

²³ National Instruments, Austin, TX

²⁴ Apple Computer, Quadra 950, Cupertino, CA

²⁵ Philips PM5138, Hamburg, Germany

²⁶ Trek Model 664, Medina, NY

a Kepco amplifier²⁷. The Trek amplifier was used for most experiments. The bandwidth of both amplifiers was limited in driving the capacitive piezoelectric load. The capacitive load was approximately 5 nF for the free PFC's and 100 nF for the active plies in the adaptive plates. The Kepco amplifier was used in experiments requiring 1 kHz bandwidth, but less than 1 kV. The Trek amplifier was limited to 100 Hz and 10 kV. The bandwidths were experimentally established using a Tektronix Fourier Analyzer²⁸.

Free PFC's were poled and tested in a thermally controlled silicon oil bath²⁹. The silicon oil³⁰ was selected to reduce dielectric breakdown effects at the edges of the electrodes. First, each PFC was tested at high electric field levels with a 0.1 Hz sinusoidal voltage signal in order to determine the coercive field (E_c). The onset of polarization reversal could be clearly established from a plot of strain versus electric field, as was described in Chapter 2, Section 2.1. In a PFC, the effective coercive field of the composite is much higher than that of pure PZT5H. At room temperature, the coercive field level for a typical PFC is about 2400 V/mm, while the coercive field for PZT5H is 800 V/mm [Bent and Castro, 1993]. In order to enable more effective poling, the temperature of the oil bath was raised. The higher temperature reduces the coercive field level of the piezoceramic. Data from Bent and Castro show a nearly linear decrease in the coercive field of PZT5H from the initial 800 V/mm at 30°C to 680 V/mm at 60°C, and to 600 V/mm at 80°C. PFC samples were typically poled at approximately 6000 V/mm and 60°C for 20 minutes. The sample was cooled before the field was removed.

Once poled, samples were allowed to age for at least 24 hours so that piezoelectric properties would settle to near steady-state values. Then low field actuation tests, with the applied electric field less than $\pm E_c$, could be accomplished. All data were collected at room temperature, or approximately 20°C.

4.1.2 Adaptive Plate Testing

The adaptive plates were tested in a different manner than the PFC's. Instead of strain gages, a pair of Keyence laser displacement sensors³¹ were used to measure the tip displacements of the free end of the horizontally mounted, cantilevered plate, as shown in Figure 4-1. Small white targets were affixed to the corners. A 1.27 cm length of the plate was clamped. The coercive field level for each ply was estimated from displacement versus electric field data as with free PFC's. Then the active plies were poled simultaneously at

²⁷ Kepco BOP1000M amplifier, Flushing, NY

²⁸ Tektronix 2630 Fourier Analyzer, Campbell, CA

²⁹ Neslab Instruments Exacal Ex-250HT, Newington, NH

³⁰ Dow Corning 200 Fluid, Midland, MI

³¹ Keyence Corp., LB11/70, LB12/72, Fair Lawn, NJ

approximately 5000 V/mm in an 80°C environmental chamber³². The voltage was held for 20 minutes. Then the plate was cooled, and the voltage was removed.

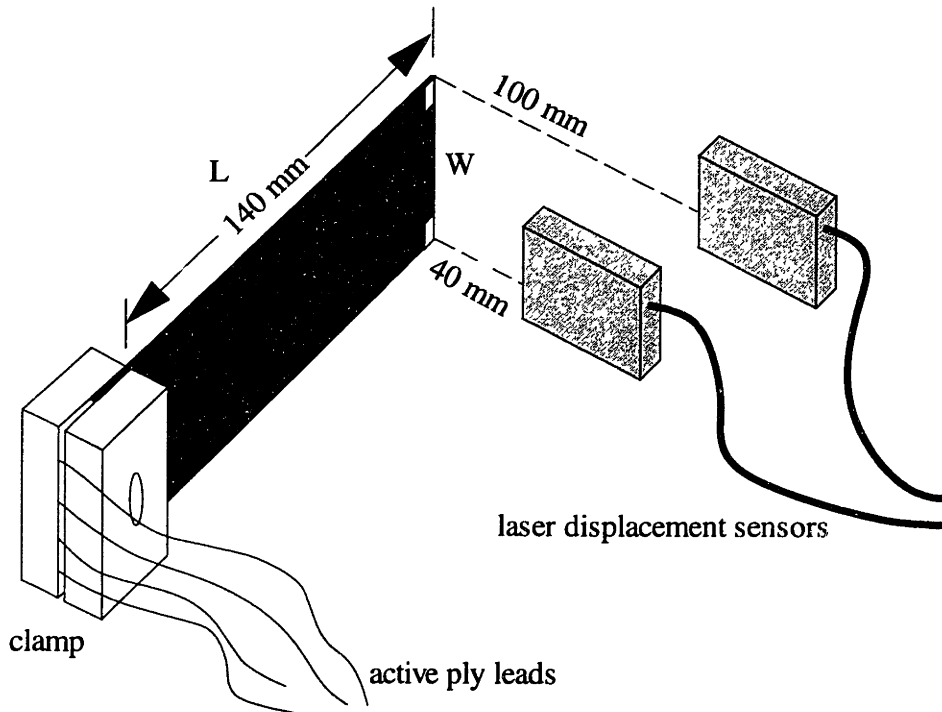


Figure 4-1. Experimental set-up for adaptive plate testing.

Further experiments on the poled adaptive plate were performed with the same experimental arrangement. The entire set-up was mounted on a dynamically isolated optics bench and was protected from airborne disturbances. The measured displacements from the two tip sensors were used to calculate the bend rate and the twist rate of the cantilevered plate.

Assuming a constant curvature for the plate, the longitudinal bend curvature and the twist curvature are defined:

$$\kappa_1 = -\frac{\partial^2 w}{\partial x^2} \quad \text{and} \quad \kappa_6 = -2\frac{\partial^2 w}{\partial x \partial y} \quad (73)$$

The expression for the bending curvature can be integrated twice to find an expression for the deflection of the plate as a function of x . The deflection of the free end of the plate, which has length, L , can then be described by the average of the two laser displacement sensor measurements, z_1 and z_2 , at the free tips of the plate:

³² Envirotronics ST8-R, Grand Rapids, MI

$$w(L) = -\frac{1}{2}\kappa_1 L^2 = -\frac{z_1 + z_2}{2} \quad (74)$$

The bend rate, or average bending curvature, can then be solved for:

$$\bar{\kappa}_1 = \frac{z_1 + z_2}{L^2} \quad (75)$$

The expression for the twist curvature can be integrated with respect to x and evaluated at $x=L$ to find the average slope at the tip:

$$\frac{\partial w}{\partial y}(L) = -\frac{1}{2}\kappa_6 L = -\frac{z_1 - z_2}{W} \quad (76)$$

The twist rate or average twist curvature of the plate is:

$$\bar{\kappa}_6 = \frac{2(z_1 - z_2)}{LW} \quad (77)$$

where W is the distance between the laser sensing beams. Typical values for L and W in the experiments were 14.3 cm and 6.3 cm, respectively.

Once poled, the applied electric field never exceeded the coercive field (to avoid repoling). Although, for some tests, the negative of the coercive field was exceeded. In such cases, high field levels were applied in the same direction as the polarization of the PFC, which is toward saturation.

4.1.3 Current Measurements

In addition to the strain data collected, it was necessary to measure the current delivered to the PFC's. The current measurements could be integrated to find the charge or the electrical displacement, D . The voltage drop across a small resistor in series with the PFC was used to estimate the current flow. The resistance was selected to minimize the voltage drop across the current monitoring resistor while enabling a measurable signal. In addition, transfer function data were used to ensure that the dynamics of the entire circuit were not altered within the frequency range of interest. A 500 Ω resistor was typically used. In comparison, the resistance of a 2.5 cm square PFC was on the order of 100 $M\Omega$.

4.2 PFC CHARACTERIZATION

Before evaluating the characteristics of the adaptive plates manufactured in the previous chapter, the properties of the PFC's or active plies must first be known. Previous investigations of PFC's have provided experimental data on the electrical and

electromechanical properties [Bent and Hagood, 1994]. This was essential for validating the DUF model used for predicting the effective properties of the active plies in this work. Further data are needed to better characterize the specific component materials which comprise the current PFC.

4.2.1 Typical Operation

The first step in the characterization process was to measure the typical operation strains for a free PFC sample. The coercive field of the sample was approximately 2500 V/mm. Using a 1000 V/mm peak-to-peak, sinusoidal voltage signal, a PFC was driven at 1 Hz in an oil bath. High field data was also collected using a 7300 V/mm signal with a 3650 V/mm DC offset. In both tests, the electric field was applied in the same direction as the polarization. The longitudinal and transverse strains were measured and are plotted versus applied electric field in Figure 4-2 for a unconstrained sample having a 0.75 width line fraction of fibers. It is important to note the anisotropy in the actuation—the longitudinal strains (along the fibers) are significantly larger than the transverse strains. This is the piezoelectric free-strain anisotropy. Additional anisotropy is evident in the stiffness properties of the PFC's.

At low electric field levels, the strain versus electric field plots are similar to pure PZT5H data as was presented in Section 2.1; however, the slope of the approximately linear operating curve is greater in the fiber direction than in the transverse direction. The unequal d_{31} and d_{32} constants reflect this trend.

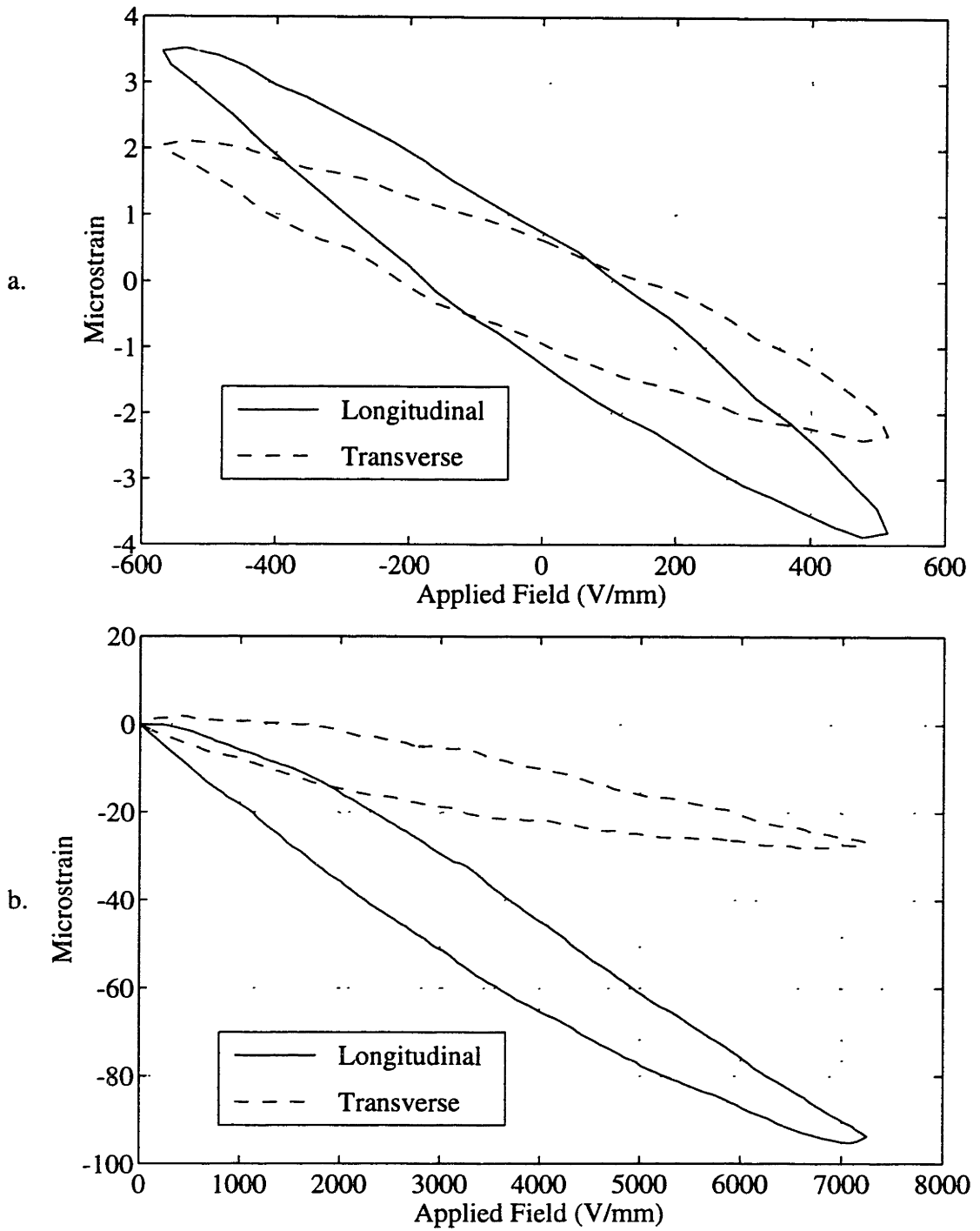


Figure 4-2. Typical operating curves for a free PFC in longitudinal and transverse directions at 1 Hz: a. low field, b. high field.

4.2.2 Component Property Tests

In order to accurately model the effective properties of PFC's, the properties of each of the component materials must be established. For the DUF model, the inputs include the mechanical, electrical, and electromechanical coupling properties of the fibers and the matrix. Table 4-1 presents the general strategy used in evaluating the component properties. First, the referenced values for the relative dielectric and d-constant of the PZT5H fibers were assumed to be fairly accurate. This left only the fiber stiffness as an unknown. Measuring the fiber stiffness directly has proven to be extremely difficult; therefore, the stiffness of the matrix was measured, and the longitudinal stiffness of the complete composite was measured. Then, the DUF model was used to back out the approximate fiber stiffness.

Table 4-1. Component Property Evaluation Strategy

	Dielectric	Stiffness	d-constants
Fibers	<i>assumed</i>	<i>predicted</i>	<i>assumed</i>
Matrix	<i>measured</i>	<i>measured</i>	<i>negligible</i>
PFC	<i>measured</i>	<i>measured</i>	<i>measured</i>

For the electrical properties, the relative dielectric of the matrix was measured for a given PZT5H powder content. The effective relative dielectric of the PFC's could also be measured. The latter measurements were used as a check on the model predictions. Finally, the effective d-constants of the PFC's could also be measured. This data was used as a check, although accurate measurements proved difficult to obtain, especially because of an unmodeled frequency dependence which will be described in Section 4.4.

Compliance Data

Two independent sets of stiffness tests were performed on pure matrix and complete PFC samples. In all tests, a force transducer³³ was used to measure the load applied to the sample while the surface strain was measured with a strain gage. In the first set, a 1.27 cm by 2.54 cm PFC was bonded to a 75 μm thick steel substrate. The modulus of the substrate was approximated as 205 GPa. Epotek 330 epoxy³⁴ was used for the bond. The bond layer was approximated as 12 μm thick, and the modulus of the epoxy was estimated as 3 GPa. The fiber/matrix layer was 0.135 mm thick, and the polyester

³³ PCB Model 208A02/484B, Depew, NY

³⁴ Epoxy Technology, Inc., Billerica, MA

electrodes were 25 μm thick. Figure 4-3a shows a schematic of the bending stiffness tests. A pure matrix sample with dimensions 1.27 cm by 3.8 cm, but without the substrate was also tested. One end of each sample was clamped while a line force was applied to the free end using a razor blade edge. Each sample was tested at an approximately constant strain rate to 500 microstrain over 10 seconds. A linear curvefit of the force versus strain data at 100 microstrain was used to approximate a constant slope. Assuming standard values for the steel substrate and polyester electrodes, the stiffness of the fiber/matrix layer was calculated for each sample. Bernoulli beam theory assumptions were applied for a multilayer beam in pure bending. Each sample was tested three times, and the values were averaged. Six PFC samples with a 0.5 line fraction of fiber, and one matrix sample were tested. The matrix contained 83 wt. % PZT5H powder with 2 % dispersant in all cases.

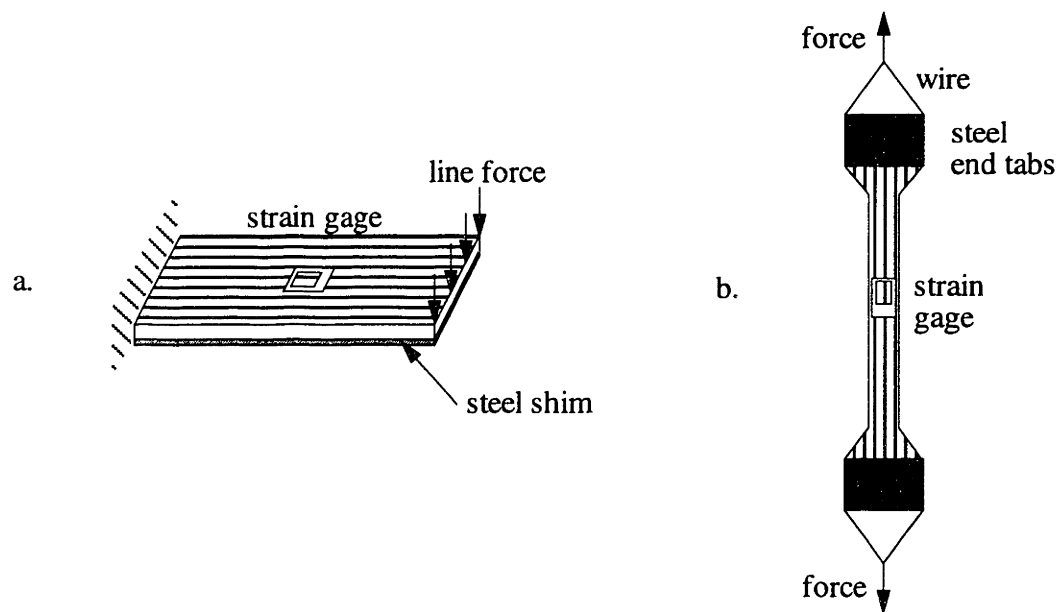


Figure 4-3. PFC stiffness tests: a. bending, b. extension.

In the second set of tests, six PFC samples in a dogbone shape were tested in extension as shown in Figure 4-3b. The test was designed to conform as well as possible with ASTM standards, but limits in the size and availability of piezo fibers necessitated modifications [ASTM, 1993]. The dimensions of the narrow section were 0.64 cm by 6.35 cm with an additional 1.27 cm of length at each end in the taper and the tab. This set of PFC coupons had a 0.75 line fraction of fiber across the width. The fiber/matrix layer was 0.135 mm thick, and the polyester electrodes were 25 μm thick. A pair of pure matrix samples were also tested, but with a rectangular geometry with dimensions of 0.86 cm by 4.13 cm. The electrodes on each sample were shorted together ($E=0$) using Epotek 410E conductive epoxy. The load was applied through steel end tabs joined to a wire loop. The

end tabs ensured a more uniform application of the load, while the wire reduced off-axis forces and moments. The tabs were affixed with M-Bond adhesive. The extension tests were performed at an approximately constant strain rate up to 500 microstrain over 10 seconds. The slope of the stress versus strain plot at 100 microstrain was used to estimate the stiffness of each sample. For each sample, the estimated values of two tests were averaged. The stiffness of the fiber/matrix layer was calculated using the standard stiffness value for the polyester electrodes.

The DUF model was used to estimate the fiber stiffness based on predictions for the effective longitudinal modulus. First, the stiffness of the matrix was estimated from the experimental data. In the bending test, the matrix stiffness was estimated as 9.3 GPa. In the extension tests, the stiffness was 6.5 GPa. This latter value was assumed to be more accurate on the basis of more data points and more straightforward testing. Next a mean and standard deviation were calculated for the experimental fiber/matrix stiffness data. Finally, the fiber stiffness was determined in order to match the mean experimental stiffness, as well as one standard deviation unit above and below the mean stiffness. This resulted in a mean, high, and low value for the fiber compliance for both the bending and extensional tests. Table 4-2 summarizes the two sets of stiffness tests. The experimental longitudinal modulus data is given for each sample, along with the mean and standard deviation. The predicted fiber stiffness is then listed relative to the bulk PZT5H value (62 GPa). A value of 1.0 means that the fiber stiffness is equal to the bulk ceramic stiffness.

Table 4-2. PFC Stiffness Data (GPa) and Predicted Fiber Compliance Relative to Bulk.

	PFC Samples						Statistics		Ratios		
	1	2	3	4	5	6	μ	σ	LB	Base	UB
bend	28.2	17.8	35.4	21.6	27.8	36.4	27.7	6.7	0.63	0.87	1.06
extend	17.2	14.2	15.8	17.8	20.2	20.2	17.3	2.2	0.34	0.41	0.47

In summary, the stiffness of the fibers was found to be significantly less than the stiffness of the bulk ceramic. In the bending tests, the stiffness was reduced by a factor of 0.87 while in the extensional tests, the reduction was a factor of 0.41. In order to investigate the possibility that the fibers were being broken during the manufacturing process, thus increasing the effective compliance of the PFC's, additional extensional test coupons were manufactured using no pressure for compression. This resulted in coupons with very low through-thickness fiber line fractions ($x_3=0.5$). The measurements from

three coupons having the same geometry as the original extensional coupons correlated well with the initial tests.

One explanation for the significantly different data for the bending and extensional tests is the presence of a secondary load path in the bending test articles. The steel substrate bonded to each PFC provides a means for load transfer within the coupon. The low effective stiffness in the extensional tests may have resulted from multiple fractures along the length of the fibers. The load is transferred between fiber segments through the soft matrix material. In the bending tests, the load could be transferred between fiber segments through the steel rather than through the matrix. This could increase the effective stiffness of the composite. The results of the extensional tests were used for the adaptive plate model predictions which are summarized in Section 4.2.3. The bending test results were used in a previous publication [Rodgers and Hagood, 1995].

Dielectric Data

Referring back to the original material property evaluation strategy, the next step was to determine the relative dielectric of the hybrid matrix material. The matrix dielectric was a variable in the development of the PFC prepreg manufacturing process described in the previous chapter. Matrix samples with various compositions were manufactured and then tested. Each sample had dimensions of 1.27 cm by 3.81 cm with a thickness of approximately 1 mm. Silver/polyester electrodes were used. The capacitance of each sample was measured³⁵ along with the thickness in order to calculate the relative dielectric. All doped samples contained PZT5H powder and 2% dispersant. Table 4-3 lists experimentally determined relative dielectric values for various powder weight percents. Viscosity limitations resulted in the selection of an 83 wt. % mixture for the adaptive plates. The value of 23 was used for all model predictions.

Table 4-3. Matrix Dielectric Measurements

PZT wt. %	0	69	83	84	85
ϵ_m/ϵ_0	5	11	23	27	28

Dielectric data was also obtained for PFC samples of various compositions in order to check the accuracy of DUF model predictions. All samples were 1.27 cm square and had 0.5 width line fraction of fibers (x_2). Thickness measurements spread over 9 locations on each sample were averaged to determine the x_3 parameter for each sample. The relative

³⁵ Omega Engineering, Model HHM57, Stamford, CT

dielectric of each sample was calculated from the geometry and a capacitance measurement. These values are compared with DUF model predictions in Table 4-4. A significant portion of the error may be attributed to inconsistencies in the manufactured quality of the samples. For example, the presence of any air bubbles in the matrix reduced the measured capacitance. The value of the matrix dielectric also contains some uncertainty. The last two samples were the most recently manufactured, and may have the best quality. Predictions were more reliable for these samples.

Table 4-4. Comparison of Predicted and Experimental Relative Dielectric.

Sample	1	2	3	4	5	6	7	8	9	10	11	12
x_3	0.93	0.91	0.96	0.98	0.97	0.91	0.91	0.90	0.97	0.70	0.90	0.94
matrix	13	28	28	25	28	28	28	28	28	37	24	24
PFC	39	121	99	116	113	103	67	69	123	81	75	84
DUF	33	87	126	151	142	87	87	82	142	63	71	91
Error (%)	-15	-28	27	30	26	-16	30	19	15	-22	-5	8

For embedded PFC plies, the exact thickness of the cured actuators cannot be determined. Only the capacitance can be measured. The effective relative dielectric can be estimated from the approximate thickness of the ply. In order to establish DUF model predictions for the effective properties, the dielectric data are used to estimate the x_3 geometric parameter, which is the actual input to the DUF model. In order to account for the errors in the model predictions, as shown in Table 4-4, a $\pm 30\%$ error in the predicted dielectric was assumed. This error was applied to the x_3 input of the model, creating upper and lower bounds.

4.2.3 DUF Model Predictions for Effective Properties

Given the experimental and referenced values for the material properties of the components, the effective properties of the active plies can be predicted. For each active ply, the relative dielectric was estimated. The DUF model was then used to establish a range for the x_3 parameter, which was combined with the range for fiber compliance to yield a baseline model prediction along with upper and lower bounds. The input parameters and predicted effective properties from the DUF model are presented in Table 4-5 for each adaptive plate manufactured.

Table 4-5. Summary of Inputs and Outputs of DUF Model for Two Adaptive Plates.

		plate 1			plate 2		
		worst	baseline	best case	worst	baseline	best case
Input	x_2	--	0.5	--	--	0.75	--
	x_3	0.91	0.94	0.97	0.92	0.96	0.975
	s_{11}^f (pm ² /N)	47.9	40.4	35.5	47.9	40.4	35.5
	s_{11}^m (pm ² /N)	--	155	--	--	155	--
	$(\epsilon_3^T/\epsilon_0)^f$	--	3400	--	--	3400	--
	$(\epsilon_3^T/\epsilon_0)^m$	--	23	--	--	23	--
	d_{31}^f (pm/V)	--	-273	--	--	-273	--
Output	ϵ_3^T/ϵ_0	72	87	119	99	146	185
	d_{31} (pm/V)	-6.8	-9.5	-14.5	-9.2	-14.4	-18.3
	d_{32} (pm/V)	-5.5	-7.6	-11.7	-8.0	-12.6	-16.1
	s_{11}^E (pm ² /N)	83.1	72.5	64.5	65.6	56.6	50.3
	s_{12}^E (pm ² /N)	-27.2	-24.2	-21.8	-22.1	-19.6	-17.9
	s_{22}^E (pm ² /N)	101	94.9	90.2	78.0	70.9	66.0
	s_{66}^E (pm ² /N)	265	256	249	194	180	170

The outputs from the DUF model were input directly into the Rayleigh Ritz plate model. The DUF model predictions represented only the fiber/matrix layer, without electrodes; therefore, separate polyester plies were included in the model. The properties of the polyester as well as the AS4/3501-6 plies are provided in Table 4-6. The thickness of the graphite plies was 0.134 mm, while the thickness of the polyester plies was 0.025 mm. The density of the fiber/matrix layer was calculated as 5200 kg/m³ for the first plate and 5700 kg/m³ for the second.

Table 4-6. Material Properties of Graphite/Epoxy and Polyester Plies.

	AS4/3501-6	polyester
s_{11} (pm ² /N)	7.7	1000
s_{12} (pm ² /N)	-2.2	-300
s_{22} (pm ² /N)	95.2	1000
s_{66} (pm ² /N)	167	1430
ρ (kg/m ³)	1520	1100

In the comparisons of adaptive plate data with model predictions which appear in Section 4.4, a solid line is shown for the baseline model predictions. A pair of dashed lines represents the best and worst cases.

4.2.4 Preliminary Strength Testing

In order to evaluate the efficacy of embedding PFC plies within a graphite/epoxy laminate, tensile strength tests were performed. Test coupons were manufactured with either a 12.5 μm kapton film layer, a 12.5 μm copper/kapton film layer, or nothing at all for the control case. Two types of symmetric laminates were manufactured. The interlaminar film layer was placed at the center of the laminates. A [15/0/-15]_S lay-up was selected for high shear stresses on the interlaminar film. A [60/0/-60]_S lay-up was selected because it was quasi-isotropic [Jones, 1975]. Six plates with dimensions of 30.5 cm by 35.6 cm were manufactured from Hercules AS4/3501-6 prepreg tape. The plates were cured using the standard autoclave cure schedule. From each plate, representing one of the six combinations of interlaminar material and lay-up, three 5.0 cm by 30.5 cm tensile coupons were cut. Only two coupons were cut for the copper/kapton, [60/0/-60]_S laminate because of a delamination failure during machining. Fiberglass end tabs were bonded to each coupon using FM-123-2 adhesive³⁶. The tabs were cut from an 11-ply fiberglass laminate having alternating 0° and 90° plies. Each tab had dimensions of 5.0 cm by 7.5 cm, and had a bevel on the edge facing the center of the coupon. A single strain gage was bonded to the center of each test article.

The coupons were tested to failure in an MTS machine³⁷ with 600 psi hydraulic grips and stroke control. The stroke rate was 750 seconds/inch. Force and strain data were recorded with a LabView data acquisition system. Thickness and width measurements in the test section were used to determine the failure stress. Results of the tests are shown in Figure 4-4 for both lay-ups. No degradation in strength was observed for the laminates containing pure kapton film. Only a slight degradation on the order of 10% was observed for the copper/kapton laminates. Delamination was evident in the copper/kapton failures. This result correlates well with the bonding difficulties discussed in Chapter 3 between copper and epoxies containing amine curing agents, such as the 3501-6 [Hercules]. An excess of amine curing agent can also degrade the kapton polyimide film [DuPont], though no such effect was observed in these tests. No effect has been observed with the polyester electrodes used in the manufacture of the adaptive plates.

³⁶ Cyttec, FM-123-2 adhesive, Havre de Grace, MD

³⁷ MTS 800 system, Minneapolis, MN

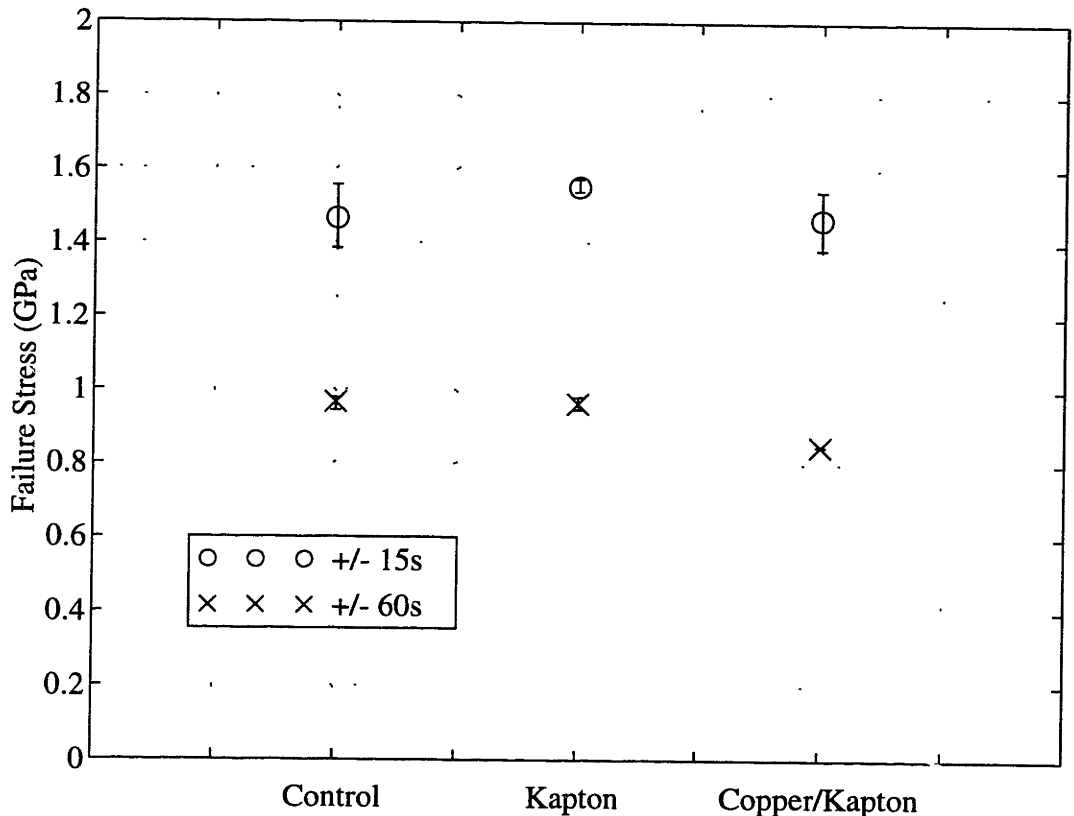


Figure 4-4. Tensile strength tests of AS4/3501-6 laminate coupons, $[15/0/-15]_S$ and $[60/0/-60]_S$.

4.3 ADAPTIVE PLATE EXPERIMENTS

Two adaptive plates were tested as described in the experimental set-up section. The first experiment was intended to demonstrate the independent control of bending and twisting operating modes of the cantilevered plate. Unfortunately, a defect in the first plate resulted in the electrodes for the -45° active ply being shorted. This was most likely a result of an air bubble which enabled a dielectric breakdown to occur, resulting in the short-circuit condition. The $+45^\circ$ ply was fully operational and did provide data, which are presented in later sections. The second adaptive plate was functional and was used to demonstrate bend and twist operation.

Subsection 4.3.2 presents transfer function data for each of the plates. In each case, a random noise signal from the Tektronix Fourier Analyzer drove a single active ply. Laser displacement data are used to characterize the response. Plate dynamics are compared with model predictions for the natural modes of the structures.

Model predictions for the actuation of the plates were then compared with experimental data across a range of frequencies below the first structural mode.

Comparisons are presented for both plates. For the second plate, single- and dual-ply actuation were evaluated. The last section presents data describing unmodeled nonlinearities in the plate actuation.

4.3.1 Bend and Twist Operating Modes

Independent control of bending and twisting actuation was demonstrated with the second adaptive plate. A 740 V/mm DC offset was used to shift the triangular wave in order to avoid depoling. Data were recorded at 0.01 Hz for a 5900 V/mm peak-to-peak applied field. Four cases were tested: +45° ply actuation, -45° ply actuation, both plies out-of-phase, and both plies in-phase. Figure 4-5 shows the results.

Single ply actuation resulted in a combination of bending and twisting as expected (Figure 4-5a, 4-5b). Actuation of both plies out-of-phase caused the shear contributions of each active ply to add. The magnitude of the bending was approximately doubled, while the twisting was nearly canceled out (Figure 4-5c). The shear was also doubled, while the extensional contributions were canceled. In contrast, actuation of both plies in-phase resulted in a doubling of the twist and cancellation of the bending (Figure 4-5d). In this case the extension was doubled, while the shear was canceled. The results correspond with the predicted operation discussed in the design for an antisymmetric laminate. The origin of the large hysteresis in the twist data is not known. The hysteresis exhibited appears to be significantly greater than that shown for a free PFC in Section 4.2.1.

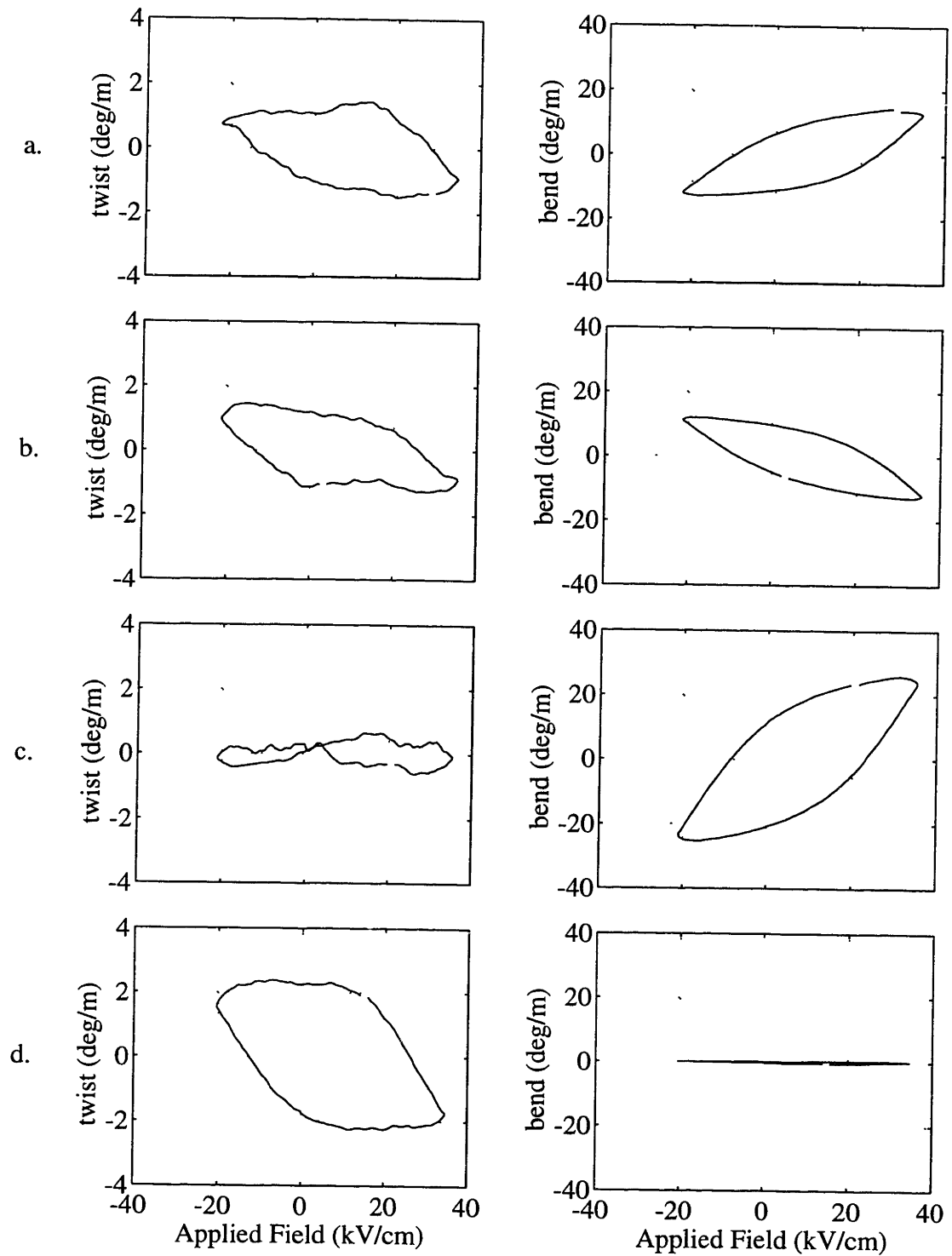


Figure 4-5. Bend and twist operation of adaptive plate 2, 0.01 Hz.

4.3.2 Passive Properties of the Adaptive Plates

Thermal stresses in the adaptive plates resulting from the high temperature cure of asymmetric laminates created a room temperature deformation as was described in Section 3.4.3. Both plates have a significant pretwist and a slight prebend which affect the passive coupling properties of the laminates. In order to quantify this coupling, a passive test was performed in which a point force was applied at locations along the free edge of a cantilevered plate. The bending and twisting response of the plate was measured for an applied force at the center of the free end as well as both free tips. In the first case, a pure bending load was applied, while in the latter cases, both bending and torsional moments were applied. Both plates were tested with applied forces of 0.098 N and 0.196 N in each location.

Analysis of the data revealed a slight bend/twist coupling in both laminates. This was the most clearly demonstrated with the application of the bending load at the center of the free edge which resulted in a combination of bending and twisting in each laminate. The 0.098 N force resulted in a deflection of 2.5 mm and a tip twist of 0.14° . Point forces applied at the free corners of the plate were intended to further evaluate the coupling through the application of combined bending and torsional moments. However, inconsistencies in that data precluded accurate conclusions about the level of the coupling present. The magnitude of the bending curvature resulting from the applied torsional moment was small.

Classical Laminated Plate Theory predicts the bend/twist coupling of the plates to be zero for an antisymmetric laminate. This passive bend/twist coupling may be explained using a von Karman analysis [Timoshenko *et al*, 1959] for initial centerline deformations of a plate. A preliminary investigation into this type of model did show that bend/twist coupling was predicted for a plate with an initial deformation shape. However, the incorporation of the actual deformation magnitudes measured for the adaptive plates resulted in extreme changes in the modal structure in comparison with the linear, flat plate predictions. The flat plate predictions were found to better represent the experimental plate behavior, which is shown below.

The unforced solution of the Rayleigh Ritz plate model provides the natural mode shapes and frequencies for a given adaptive plate. The model was used to predict the first three natural modes of each adaptive plate, using the five Jensen shape functions and four in-plane shear and extensional shapes. In order to determine the actual plate modes, transfer functions were taken from the input voltage to a single active ply, to the resulting

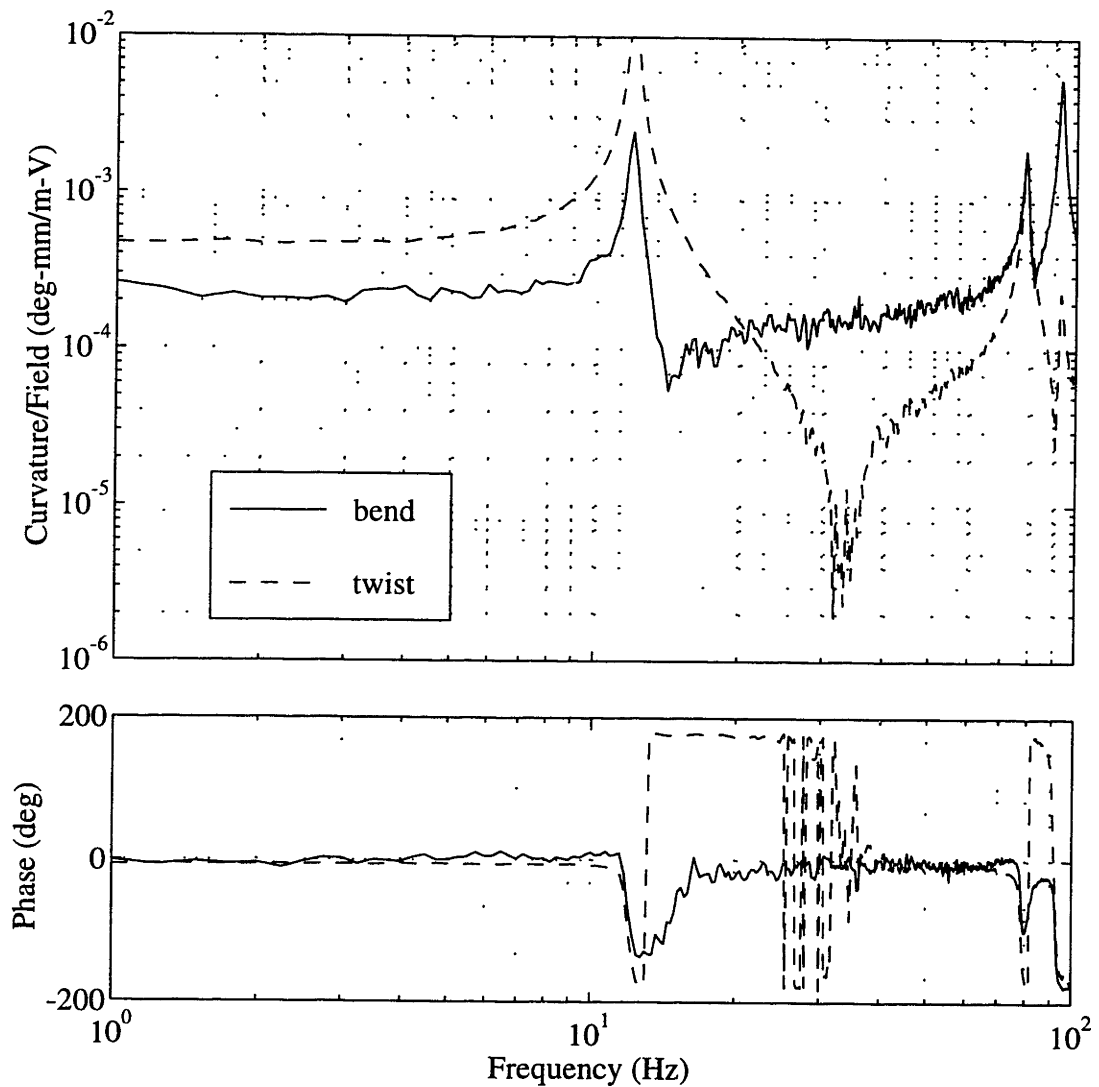


Figure 4-6. Transfer function data for plate 1 from voltage input to the $+45^\circ$ ply to bend and twist rates.

bending and twisting of the free tip of each plate. Transfer function data for the bend and twist curvature per applied field and phase are plotted for plates 1 and 2 in Figures 4-6 and 4-7, respectively.

For both plates, the location of the first three modes was clearly defined. Identification of the mode shapes was made difficult by the apparent bend/twist coupling in the plates. Large twist curvature was measured along with the bending at the first bending mode resonance. Comparison of the experimentally determined modes with the predicted natural frequencies suggested the proper mode shapes. A comparison of the predicted and experimental natural frequencies is given in Table 4-7.

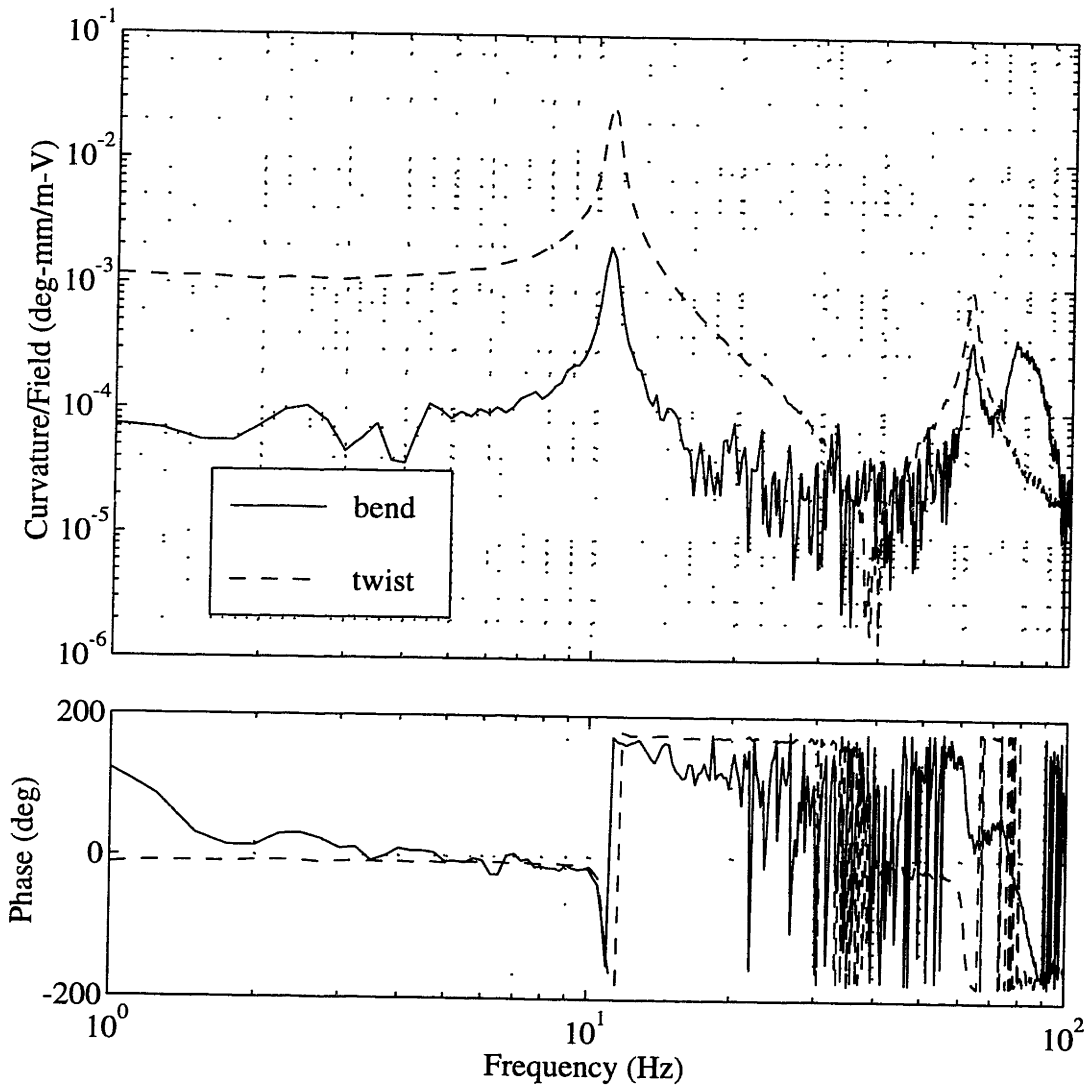


Figure 4-7. Transfer function data for plate 2 from voltage input to the +45° ply to bend and twist rate.

Table 4-7. Comparison of Predicted and Experimental Natural Frequencies (Hz).

mode	plate 1			plate 2		
	B1	T1	B2	B1	T1	B2
model	12.5	61.2	78.3	12.1	59.5	75.7
experiment	12.1	79.3	91.4	10.9	62.0	76.3
error (%)	3.3	-22.8	-14.3	11.0	-5.6	-0.8

The Rayleigh Ritz model should overestimate the natural frequencies of the plates since the model is constrained by the limited number of assumed shapes. This is true for the first bending modes, but the frequencies for higher modes were underpredicted. This was especially true for the first plate, where the errors were significant. The model may have underestimated the true stiffness of the fibers or initial deformations may have altered the modal characteristics of the plate.

4.3.3 Predicted Actuation

In this subsection, data from both adaptive plates are compared with model predictions. Model predictions are for the dynamic response of the plate, harmonically forced by either one or two active plies. For each data point measured, the active plies were forced with a triangular wave signal having no DC offset. The quoted bending or twisting curvature values used in the data plots represent half of the peak-to-peak curvature measured in the experiments. The model prediction for a given data point is the magnitude of the bend and twist curvatures calculated for the maximum specified electric field.

Data for the first plate is presented only for single ply actuation. The applied field was ± 1000 V/mm, and data was obtained for frequencies between 0.01 Hz and 10 Hz, where the first structural mode begins to appear in the response. The predicted and experimental plate response are plotted in Figure 4-8. The measured response is significantly greater than the predictions, especially for bending. The predictions are the most accurate in the 1 to 5 Hz range. At lower frequencies, a strong unmodeled frequency dependence is evident, and will be addressed further in the next section. Above 5 Hz, the first bending mode of the plate begins to affect the response. The bend/twist coupling of the plate is evident at 10 Hz, near the first resonance.

The plots for the second adaptive plate are divided into the different operating modes. First, the model predictions are compared to curvature measurements for single ply actuation. Each ply was actuated with a ± 2000 V/mm field at frequencies between 0.01 Hz and 10 Hz. The data from the $+45^\circ$ ply and the -45° ply are compared with the model predictions in Figure 4-9. Note that the agreement between the data and the model is fairly good, especially for the $+45^\circ$ ply. The frequency dependence is again evident below 1 Hz, especially in the bending. The small twist response of the plate to the -45° ply actuation suggests that this active ply was damaged in some way, and thus less effective in inducing shear. The two active plies induced approximately equivalent bending response in the plate.

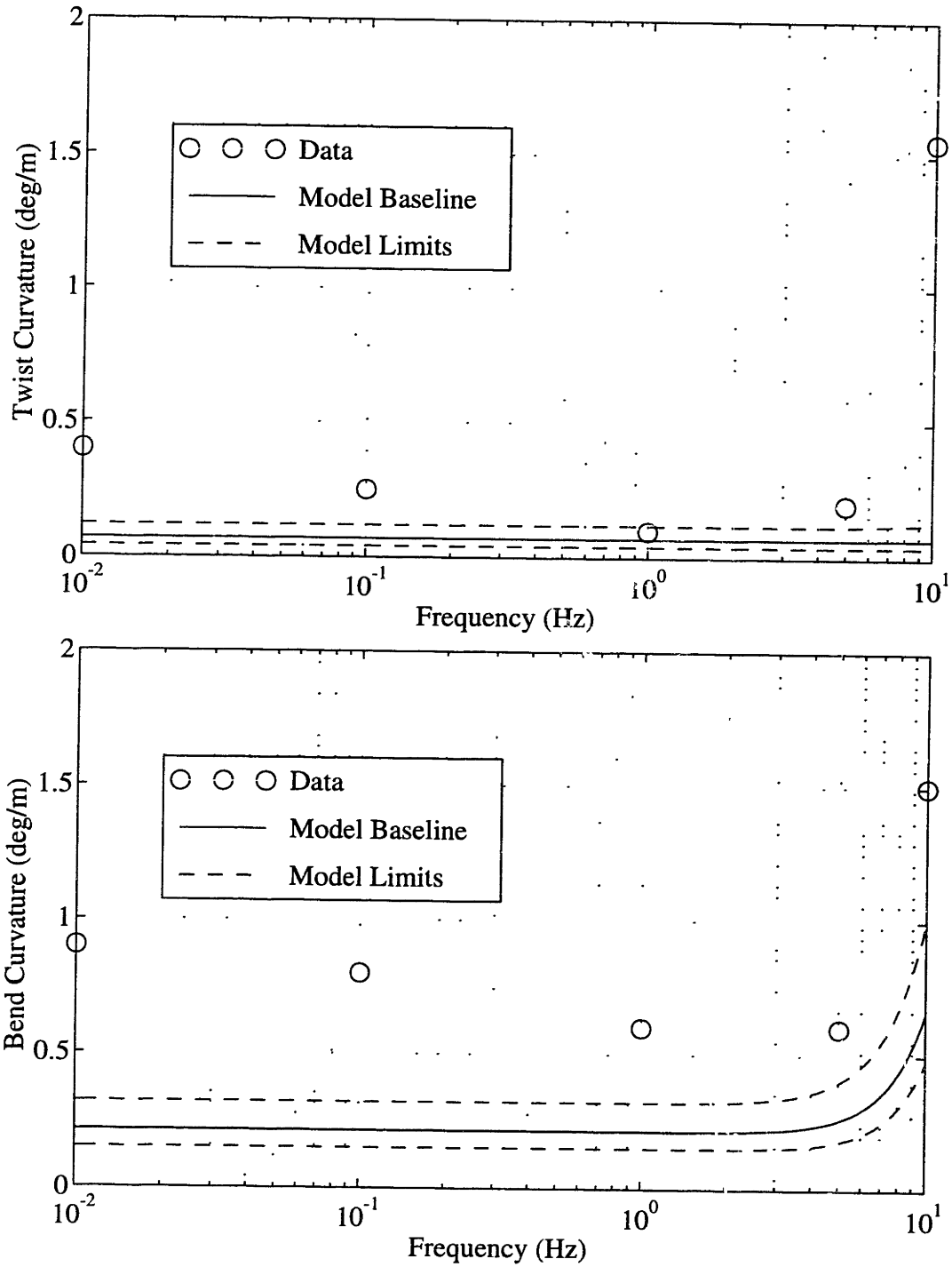


Figure 4-8. Comparison of data and model predictions for the bending and twisting of adaptive plate 1.

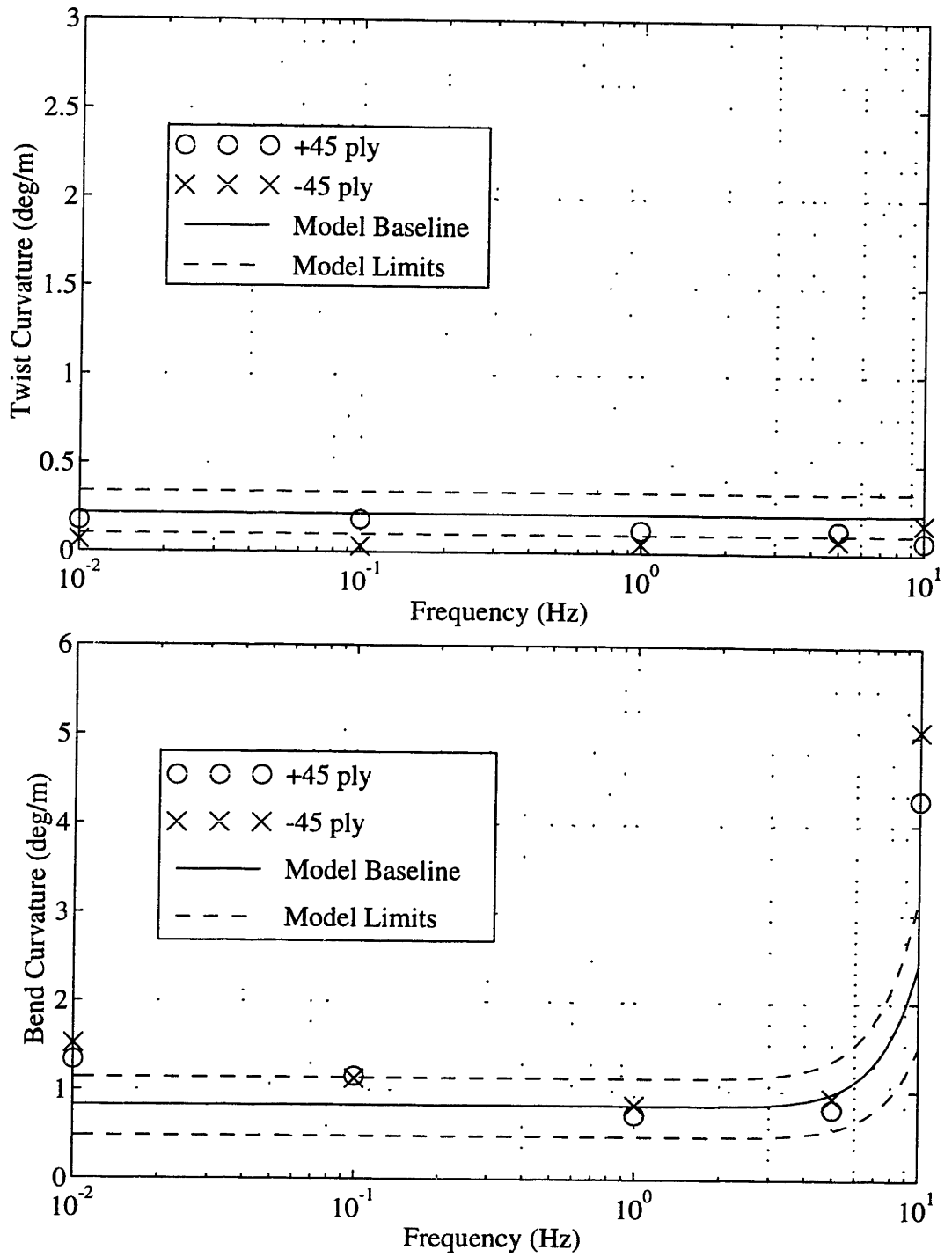


Figure 4-9. Comparison of data and model for single ply actuation in adaptive plate 2.

In the next experiment, the two active plies in the second plate were actuated in-phase at ± 2200 V/mm. The predicted twist curvature is plotted along with the measured twist and bend curvatures in Figure 4-10. Note that the predicted bend curvature is zero. As in the single-ply actuation experiment, the measured twist was below predicted levels. The frequency dependence is evident at low frequencies, but the previously noted increase in the plate response near the first bending mode is not present, since no bending was being commanded.

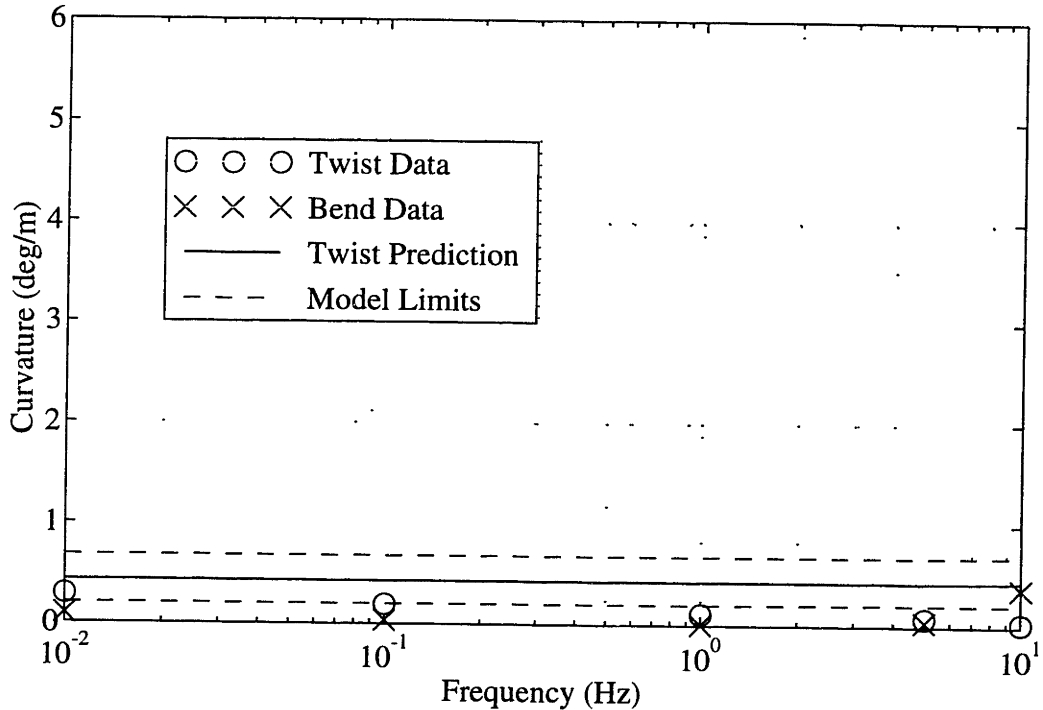


Figure 4-10. Comparison of data and model for in-phase operation of adaptive plate 2.

The final comparison between the model predictions and the data is for the out-of-phase operation case. The predicted bend curvature is plotted with the measure bend and twist curvatures in Figure 4-11. In this case, the predicted twist curvature is zero. The measured twist was rather small. The correlation between the data and the model for the bending curvature is good, especially at the 1 Hz and 5 Hz data points. The frequency dependence was again evident at low frequencies, resulting in the model underpredicting the response. At 10 Hz, both the model and the data show the effects of the first bending mode.

In summary, the adaptive plate model showed some positive predictive capabilities, especially with the second plate. Several uncertainties contributed to the inaccuracies. The

underpredictions for the response of the first plate suggested that there was a significant variation in the properties of the two plates. Predictions for the second plate were much better, though differences in the actuation capabilities of the two active plies further demonstrated the scale of possible manufacturing uncertainties. The effective mechanical properties of the fibers is a subject for further investigation, especially with regard to the load transfer mechanisms involved in the active plies. The unmodeled frequency dependence impaired correlation at lower frequencies (<1 Hz). This and other nonlinearities will be discussed in the next section.

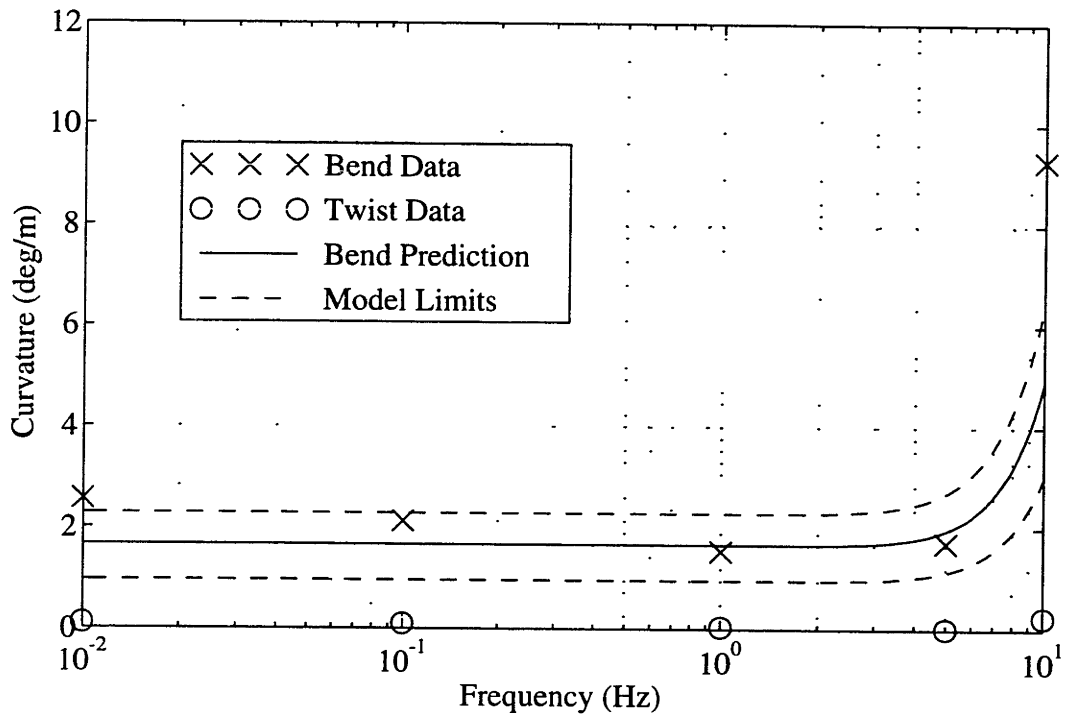


Figure 4-11. Comparison of data and model for out-of-phase operation of adaptive plate 2.

4.4 UNMODELED EFFECTS

This section is intended to better characterize the response of the adaptive plate in order to explain unmodeled effects. The adaptive plate data showed two notable nonlinearities, a high field effect and a frequency dependence. The first effect is the high field nonlinearity evident in all piezoceramics. The simple, linear model of piezoelectricity presented in Chapter 2 assumes constant, low-field values for d_{31} and d_{32} . The frequency dependence found in the plate data is also unmodeled. While the high field effect has been

previously studied for pure piezoceramics, the frequency dependence appears to be predominantly a composite effect.

Previous studies have included a nonlinear d-constant in models of piezoelectric actuation in which the value was a quadratic function of the applied field [Crawley and Lazarus, 1989]. In addition, an iterative solution technique was used to account for the dependence of the d-constant on the level of induced strain in the actuators. This capability has not been used in the current study. Other nonlinear, high field models have accounted for polarization effects in piezoceramics [Chan and Hagoood, 1994]. Anderson and Crawley [1993] have characterized piezoelectric relaxation effects which vary with frequency.

In the piezoelectric fiber composite, the composite form of the actuator further complicates the effects of piezoelectric nonlinearities. The two-phase matrix, which contains a high filler volume fraction, and the inclusion of circular fibers result in a rather complex electromechanical system. The FEM predictions for the electric field distribution presented in the previous chapter demonstrate the complexity. Different regions of the PFC are poled to varying extents and are actuated at different field levels. The development of complex models to account for the nonlinearities of piezocomposites is a topic for further study.

The following subsections will present data on high field and frequency dependent effects in free and embedded PFC actuators. The high field data is fairly consistent with data for pure piezoceramic wafers. The frequency dependence is much more significant for PFC's than for pure piezoceramics. An explanation is presented along with supporting data for free strain and adaptive plate actuation.

4.4.1 High Field Nonlinearities

The linear model of piezoelectricity assumes a constant value for the d_{31} and d_{32} parameters for all applied field levels. This assumption is generally valid only for low field operation, where the actuation is approximately linear, with some hysteretic effects. However, there is a measurable increase in the induced strain as the applied field is increased. The piezoelectric d-constants represent only the zero-field slope of the strain versus field operating curve.

The response of a free PFC ($x_2=0.5$) was measured at room temperature to determine the variation in the maximum induced free strain with applied field. The poled PFC was actuated with an electric field aligned with the poling direction. The voltage was applied as a 0.01 Hz triangular wave with a DC offset which placed the lower edge of the wave at 0 volts. The peak longitudinal strain (Λ_1) was measured for each field level. The

data are plotted in Figure 4-12 along with a linear model based on the slope of a second order curvefit to the data at 500 V/mm. The measured free strain exceeds the linear estimates by as much as 50% when actuated with up to 8000 V/mm.

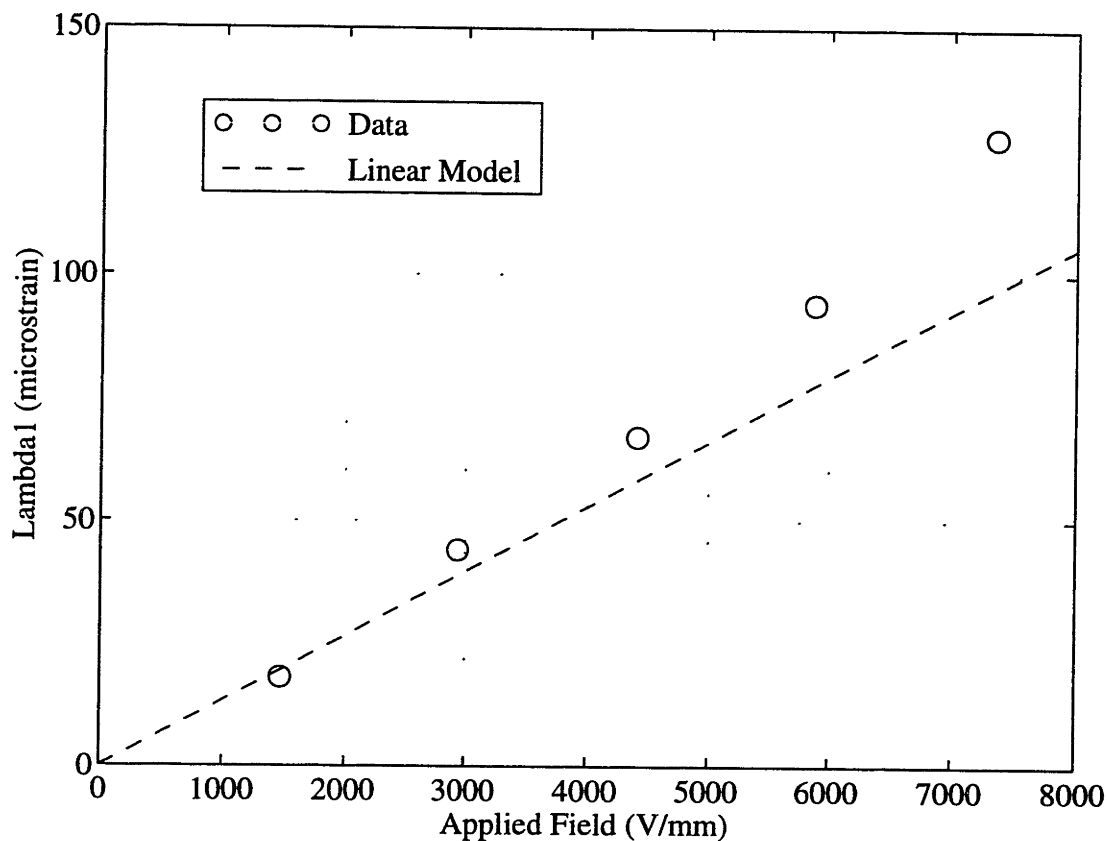


Figure 4-12. High field tests of a free PFC at 0.01 Hz.

A similar trend can be seen in data collected from the first adaptive plate. A single ply was actuated as described for the free data at 0.01 Hz with an offset triangular wave. The measured twist and bend curvatures are compared with linear estimates in Figure 4-13. The estimates were again derived from the approximate slope of a second order polynomial curvefit at 500 V/mm. In this case, the measured twist exceeds the linear estimate by a factor of two at only 4000 V/mm. The bending exceeds the estimate by more than a factor of three at 4000 V/mm. The effect appears to be stronger for the embedded actuators. This may be attributed to variations in the properties of manufactured PFC's or some nonlinear plate effect. Dielectric breakdown problems prevented testing of the adaptive plate at field levels as high as for the free PFC (8000 V/mm).

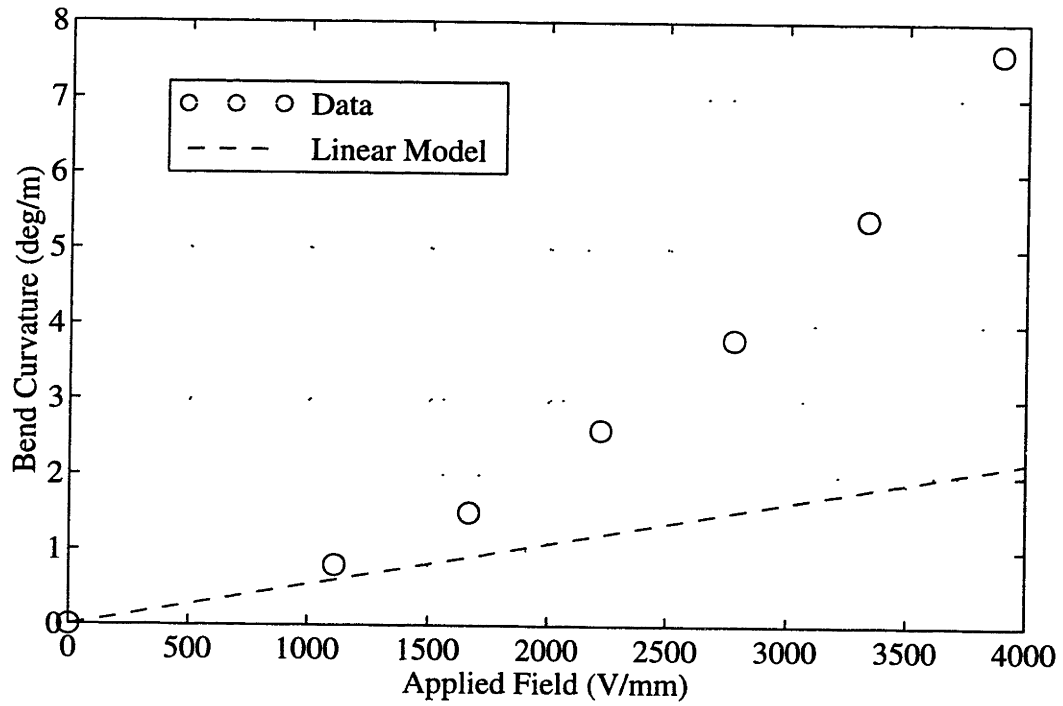
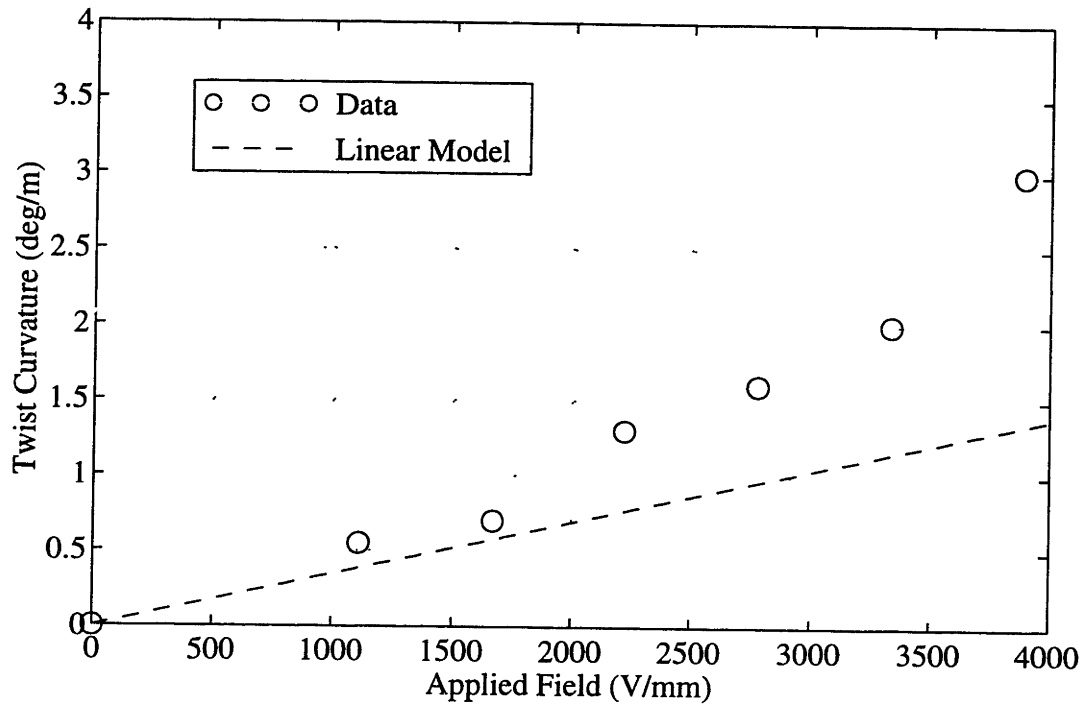


Figure 4-13. High field tests of adaptive plate 1.

4.4.2 Frequency Dependence

In order to better characterize the frequency dependence shown in the adaptive plate, data for the measured free strain of a PFC ($x_2=0.5$) were collected. The applied field was in the form of a triangular wave with a peak-to-peak amplitude of 7350 V/mm and a DC offset of 3675 V/mm to ensure that the electric field was applied in the same direction as the polarization. The maximum longitudinal and transverse strains (Λ_1 and Λ_2) were recorded for each frequency tested. The results are plotted in Figure 4-14 for frequencies between 0.01 Hz and 100 Hz. Data collection at higher frequencies was limited by amplifier bandwidth and structural modes of the actuator.

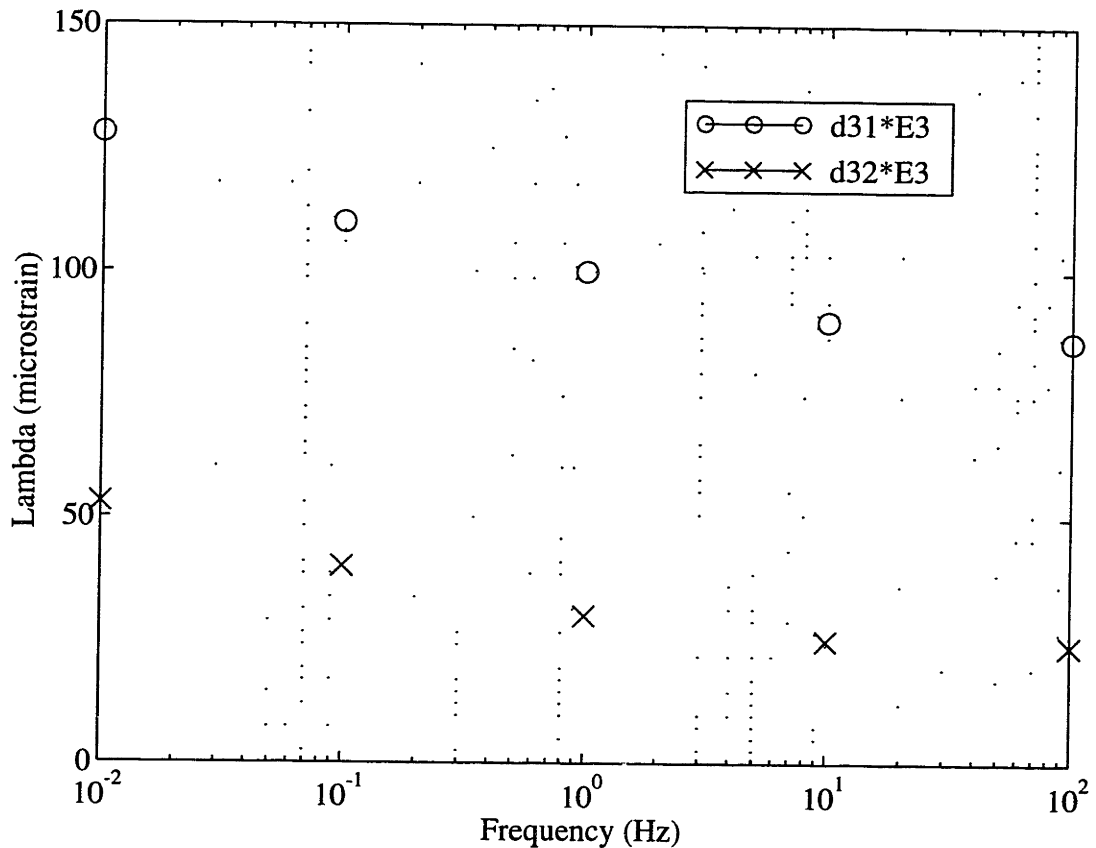


Figure 4-14. Frequency dependence of maximum free strain for a PFC.

The data show a trend of decreasing magnitude for both the longitudinal and transverse measurements. The descent appears to be approaching an asymptote near 100 Hz. A similar trend has been observed in measurements of the zero-field d-constants for PFC's. This suggests that it is not only occurring at high fields, where many nonlinearities are present [Chan and Hagood, 1994].

One theory for this phenomenon is that a trade-off is occurring between resistive and capacitive effects in the fiber/matrix system. Models of the fiber and matrix, such as the FEM discussed in Section 3.1, use a capacitive model of the piezoelectric material to estimate the electric field distribution in the composite. The dielectric properties of the materials drive the analysis. Alternatively, the PFC can be represented very simply by a resistor and capacitor in parallel. At low frequencies, the capacitor appears as an open circuit, while at higher frequencies, the capacitor approaches a short circuit. This consideration suggests that at the lower frequencies, the resistive effects may dominate.

In the DUF model, it is the dielectric mismatch between the fibers and matrix that most strongly controls the effective electromechanical coupling predictions. The matrix material above and below the fibers is combined in series with the fibers. In a resistive model, the dielectric mismatch would not effect the field distribution; moreover, the resistive mismatch may present less of an obstacle for getting the electric field into the fibers since the resistance of the matrix layer is probably significantly smaller than that of the fiber in series.

In order to provide support for this theory, polarization curves were measured for a free PFC ($x_2=0.75$) over a range of frequencies. Current measurements were taken for a 7400 V/mm peak-to-peak sinusoidal applied field at each frequency. The current measurement signal was integrated in order to calculate the electrical displacement, D . The strain was also measured. Figures 4-15 and 4-16 present the polarization curves and longitudinal strain curves for frequencies between 0.001 Hz and 100 Hz.

The relative phase between the electrical displacement and applied electric field described the general nature of the impedance. When the two are in-phase, the impedance is capacitively dominated. When the two are out-of-phase, the impedance is resistively dominated. Thus the data show a strong resistive effect at very low frequencies. As the frequency increases, the capacitive effect becomes stronger. Above 1 Hz (Figure 4-16a-c), the capacitive effect dominates. As the capacitive component grows, the strain levels decrease. The exception occurred at 100 Hz (Figure 4-16c), where structural resonance in the PFC may have amplified the response. The rounded corners on the polarization and butterfly loci may be attributed to the composite form of the actuator. Different localized regions of the piezoceramic are reaching the coercive field level at different applied field levels.

The simple parallel resistor and capacitor model also supports the trend seen in the data. A transfer function from input voltage to current was measured for an active ply in the second plate at frequencies between 0.05 Hz and 5 Hz. This was the lower frequency

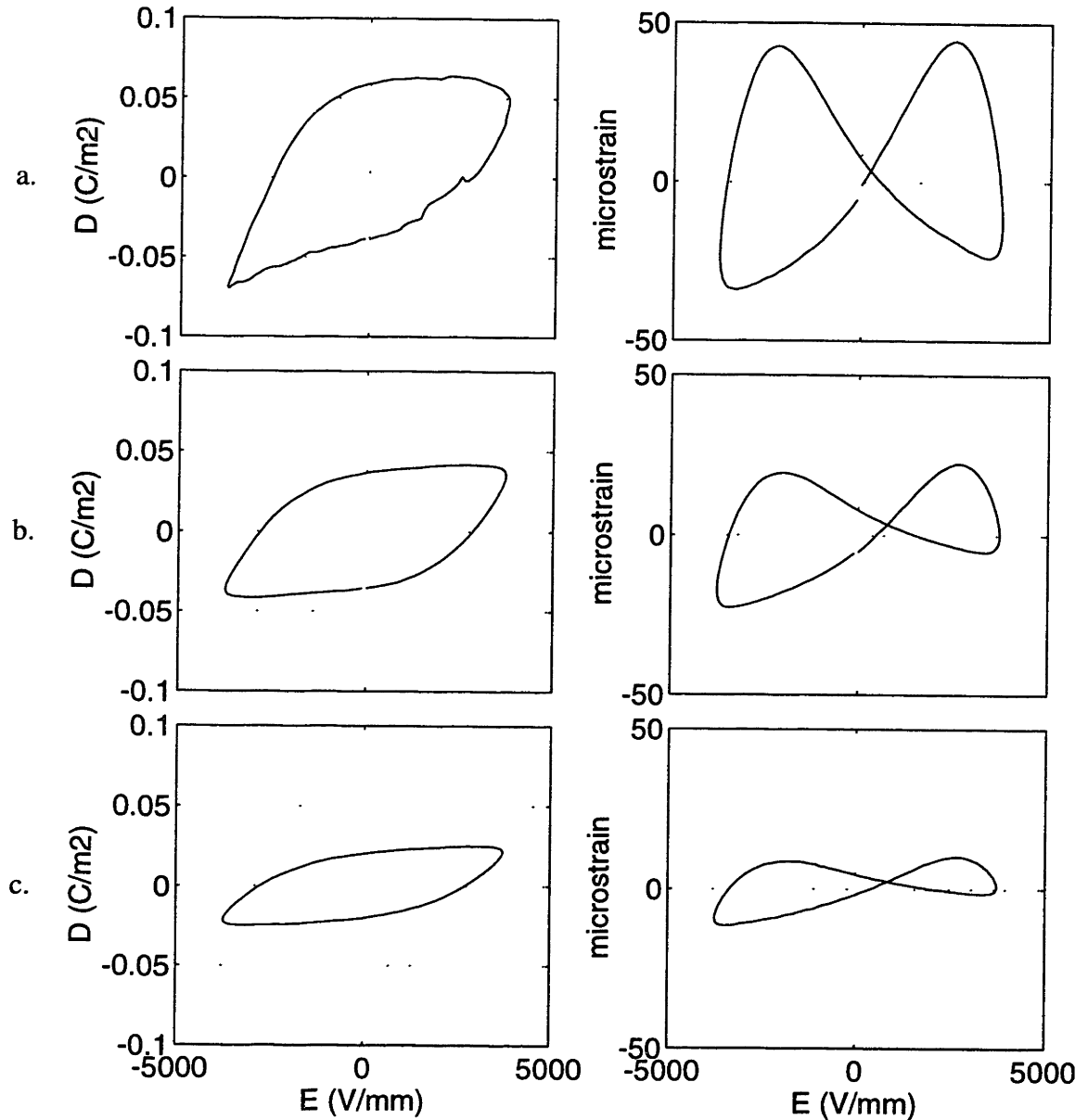


Figure 4-15. Polarization and butterfly curves for a free PFC: a. 0.001 Hz, b. 0.01 Hz, c. 0.1 Hz.

limit of the fourier analyzer. The amplitude of the applied field was 2000 V/mm peak-to-peak. Figure 4-17 shows the results of the testing.

The simple parallel model for the complex impedance was used to estimate values for the resistance and capacitance of the sample. The model followed the amplitude of the signal fairly well, though the corner frequency is below the frequency range measured. The plotted phase data, which was smoothed, did not settle to -90° as with the model. The decrease in the magnitude of the phase at the lower frequencies was the critical factor in

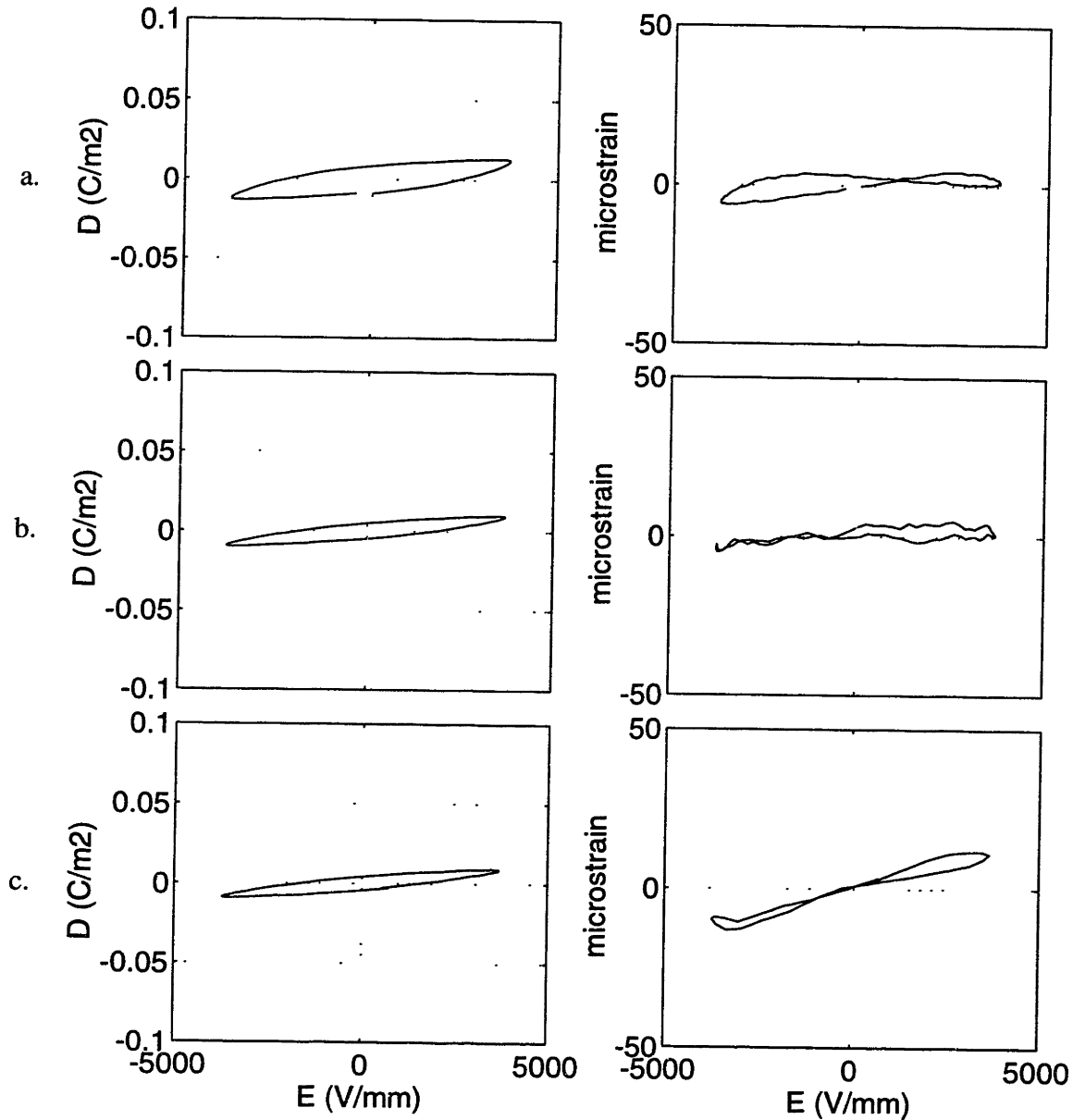


Figure 4-16. Polarization and butterfly curves for a free PFC: a. 1 Hz, b. 10 Hz, c. 100 Hz.

fitting the model. The approximated resistance was 39 M Ω and the capacitance was 102 nF. The corner frequency for these values was 0.04 Hz. This frequency corresponds with the trend in the single frequency data shown in Figures 4-15 and 4-16. The transition from a resistive to a capacitive response seems to occur in the range of 0.01 Hz to 0.1 Hz. In control terminology, this is the location of the pole in the transfer function.

Although the data presented support the resistive-capacitive explanation for the frequency dependence, other factors may be involved. The effects of piezoelectric

relaxation, strain rate, and creep have been observed in pure piezoceramics [Anderson and Crawley, 1993], and may contribute to the trends in the current data. Further analysis and more complex models including polarization effects will be required to adequately evaluate this phenomenon.

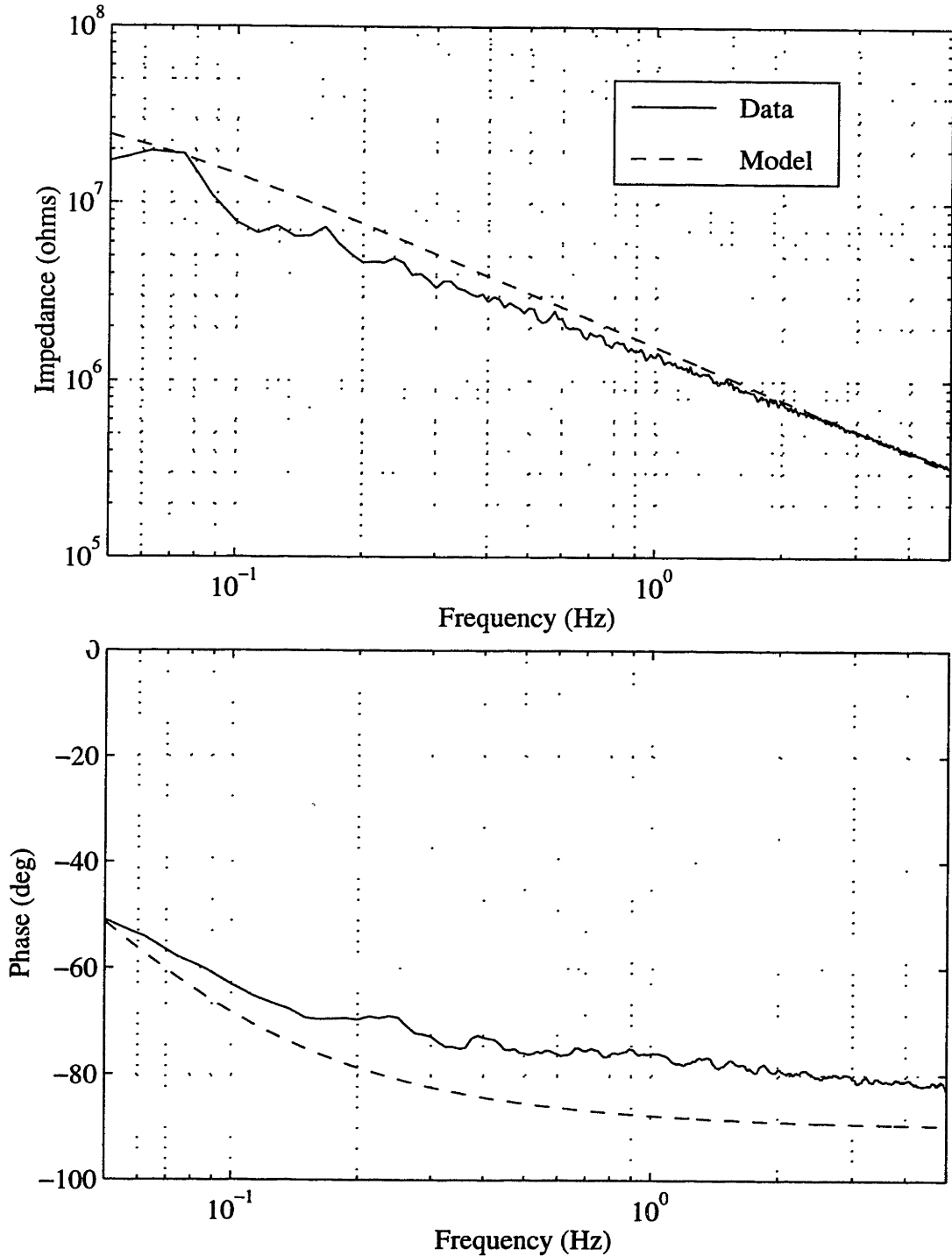


Figure 4-17. Transfer function from applied voltage to current for an active ply and model.

4.5 EVALUATION OF PEAK ACTUATION CAPABILITIES

For comparison, material properties for a perfect composite PZT5H-based actuator were established. Such an actuator would have the same amount of piezoelectric material as a PFC, but would have zero matrix stiffness and a matrix dielectric equal to that of PZT5H. The perfect composite would have the ideal stiffness anisotropy ($c_{22}^E/c_{11}^E = 0$) and ideal piezoelectric anisotropy ($d_{32}/d_{31} = 0$). The through-thickness fiber fraction would be 1. The estimated properties of the perfect composite actuator are listed in Table 4-8 for two fiber spacings.

Table 4-8. Perfect Composite Properties

x_2	0.5	0.75
ϵ_3^T/ϵ_0	3400	3400
Λ_1 (e^{-6})	450	450
Λ_2 (e^{-6})	0	0
s_{11}^E (pm^2/N)	41.1	27.4
s_{12}^E (pm^2/N)	-11.5	-8.4
s_{22}^E (pm^2/N)	∞	∞
s_{66}^E (pm^2/N)	∞	∞

In order to better evaluate the capabilities of the current PFC's, a comparison of the maximum induced stress and maximum free strain achievable was made between a PFC and the perfect composite. The conditions for the maximum applied field in the adaptive plates were chosen for the comparison. In the first plate, the maximum twist rate of 3 deg/m was measured at 3800 V/mm. 1.5 deg/m of twist was observed with an applied field of 2800 V/mm in the second plate using the +45° active ply. In order to estimate the induced stress and induced strains in the experimental laminate, the induced free strain values used in the linear adaptive plate model were chosen to match the twist actuation observed. The ratio between d_{31} and d_{32} from the model baseline was maintained.

The maximum applied field level for the perfect composite was selected to correspond with the experimental conditions for the real active plies. The actual electric field levels reaching the fibers in a PFC are much lower than the applied field. In the perfect composite, there is no loss; therefore, the comparable field level for the perfect composite was significantly lower. A value of 1000 V/mm was chosen based on high field testing of PZT5H wafers [Chan and Hagood, 1994]. This was the approximate saturation field of the ceramic.

Table 4-9 compares the actuators in several ways. First, the performance of the actuators was measured with regard to deforming the adaptive plate. The twist rate stated for the active plies were the exact experimentally determined values. The bend rate is the Ritz model prediction based on matching the experimental twist, as described above. Next, the induced longitudinal and transverse stresses achievable in the actuator ($\tilde{e}_{31}E_3$ and $\tilde{e}_{32}E_3$, respectively) are given. These were estimated from the stiffness and induced free strain and represent the maximum stress for zero strain or clamped boundary conditions. The induced shear stress of a 45° ply was also considered ($e_{36}E_3$), which is the most significant for inducing twist in the laminate. Finally, the peak equivalent free strain capability is given ($\Lambda_1 = \tilde{d}_{31}E_3$). This is the maximum longitudinal strain for a stress-free boundary condition.

Table 4-9. Comparison of Actuation Capabilities for Current PFC and Perfect Composite.

	Plate 1 active ply	Perfect Composite	Plate 2 active ply	Perfect Composite
reference field (V/mm)	3800	1000	2800	1000
twist (deg/m)	3.0	12.6	1.5	16.5
bend (deg/m)	10.6	5.6	7.4	6.8
induced long. stress (MPa)	-9.1	-10.9	-6.4	-16.4
induced trans. stress (MPa)	-6.6	0	-5.0	0
induced shear stress (MPa)	1.3	5.5	0.7	8.2
Λ (microstrain)	500	450	250	450

These comparisons illustrate several important aspects of current PFC's. In the comparison of actuation capabilities of a single active ply embedded within either of the adaptive plates, two features stand out. First, the twist rate induced in the actual PFC's in experimental plates is much less than the hypothetical capabilities of the perfect composite actuators. The second point is that the combination of low twist and relatively high bending in the adaptive plates suggests that the anisotropy exhibited in the PFC's is also much less than the ideal. In comparing the first and second adaptive plates, it is immediately evident that the maximum actuation capabilities of the first plate exceeded those of the second by a factor of approximately two. This can mostly be attributed to the limit on the maximum applied field due to dielectric breakdown in the second plate. The active ply in the first plate was pushed much closer to saturation.

The induced stress capabilities of the active plies and perfect composites were also calculated using the high field, scaled values of the piezoelectric induced stress constants. Here the great difference in the anisotropy of the active plies and the perfect composites is clear. Although the induced stress along the fibers is comparable, at least in the first plate, the transverse stress is vastly different. This is because the transverse induced stress in the ideal actuator is zero. The reduced anisotropy in the real active plies leads to greatly reduced induced shear capabilities. It is the induced shear stress which is the most crucial for actuating twist in an adaptive plate.

The final comparison is for the free strain of the various actuators. The values for the perfect composites are based on the referenced capabilities of PZT5H. The values for the current active plies also depend on the scaled d-constants. These values were not experimentally validated since the active plies were embedded in the graphite laminates. Inaccuracies in the scaling assumption may have inflated these values. Experimentally measured free strain in other PFC actuators of the same composition have produced a maximum of roughly 250 microstrain in laboratory tests. Note that these values represent actuation with a positive field only. The total induced strain capabilities of the actuators may be double that size when peak-to-peak strains are measured for a bipolar applied field.

4.6 SUMMARY

Two adaptive plates have been tested and the data have been compared with model predictions. Preliminary tests were also performed to establish properties of the component materials used in the manufacture of PFC's. These tests revealed a factor of two or more reduction in the effective stiffness of PZT5H fibers. The independent control of bending and twisting actuation was demonstrated for the second adaptive plate. Passive dynamic tests were used to evaluate model predictions for the natural frequencies of the plates. Model predictions were poor for the second and third modes of the first plate, but were otherwise good. Next, the actuation capabilities of the active plies in the two plates were compared with model predictions. The model significantly underestimated the induced bend rate and twist rate in the first plate, but was fairly accurate for the second plate. The comparisons also highlighted an unmodeled frequency dependence in the actuation. Additional data for the frequency dependence and the high field nonlinearity shown in the plate experiments were presented in the final section, and probable causes were suggested. These results will be further discussed in the conclusions.

CHAPTER 5

Conclusions and Recommendations

The final chapter of this thesis is divided into a conclusions section and a discussion of recommendations. The conclusions are drawn from the experimental results and model comparisons described in the previous chapter. This also serves as a final summary of the accomplishments to this point in the manufacturing and testing of adaptive plates. The recommendations section focuses on the next generation of PFC's. Several improvements will be implemented in the near future. In addition, preparations are underway for applications intended to demonstrate the effectiveness of PFC actuators.

5.1 SUMMARY AND CONCLUSIONS

- Successfully developed piezoelectric fiber composite prepreg manufacturing process.
- Adaptive plate manufacturing process developed to incorporate active plies in composite laminates.

The manufacturing process for the PFC prepreg was described along with the steps taken in the integration with the structural plies. A suitable B-staging epoxy was selected for the matrix material. In addition, a two-phase, hybrid matrix consisting of high dielectric filler and other additives was developed for the epoxy resin system. An etch pattern was used to improve the interlaminar electrode layers, preventing edge arcing and providing accessible electrical connections. PZT5H-type fibers, the hybrid matrix, and the

interlaminar electrodes were combined to form a prepreg tape to be used in a standard composite lay-up procedure. The prepreg form of the PFC enables some degree of conformability during the lay-up. The adaptive plate cure followed standard graphite/epoxy procedures with provisions for maintaining electrical connections at the ends of the laminate.

- Demonstrated the independent control of bend and twist actuation of an adaptive plate.
- The peak actuation capabilities of the active PFC plies induced 4.5 deg/m of twist in a graphite/epoxy laminate.

Two adaptive plates, 6.35 cm by 15.2 cm in size, were manufactured and tested. The lay-up for both plates, $[90/45_A/0/-45_A/90]_T$, was selected to enable the independent control of bending and twist actuation using a pair of active plies. The second of these plates demonstrated the bend and twist operating modes in laboratory testing. The independent modal control capabilities resulted from the induced shear stresses in the anisotropic active plies. The anisotropic active plies can be used to tailor the design of the adaptive structure to meet specific structural actuation requirements.

- Rayleigh Ritz adaptive plate model developed to predict plate response to anisotropic embedded actuators.
- A combination of polynomial in-plane and Jensen out-of-plane assumed shape functions was found to be suitable for modeling the adaptive plates.

An adaptive plate model has been developed to predict the response of composite laminates containing anisotropic active plies. A manufacturing process for producing piezoelectric fiber composite prepregs has been developed. PFC prepreg layers have been integrated with graphite/epoxy plies to form adaptive plates. Independent bending and twisting modes of operation were demonstrated. PFC's have been further characterized through tests of unconstrained and embedded actuators.

The adaptive plate model consisted of a Rayleigh Ritz plate model incorporating Classical Laminated Plate Theory. Properties of the embedded PFC active plies were obtained from an existing micro-electromechanical model of the actuators. Experiments were used to characterize the electrical and mechanical properties of the component

materials. The spread of these data, especially for the effective fiber stiffness, established an error range for model predictions.

- The Rayleigh Ritz model captured the major adaptive plate deformation trends, but improvements in the quantitative agreement require further development.

The adaptive plates were also tested in order to compare with model predictions for the response of the plate to the actuators. The tip deflections of the cantilevered plates were measured over three decades of frequencies below the first structural resonance in response to both single- and dual-ply actuation. Model predictions for the first plate, which had a lower volume fraction of fibers in the active plies, were lower than the measured values for bend and twist. Model predictions for the second plate were generally higher than the measured values, but were much more accurate overall. The model predictions were fairly good near 1 Hz, where the unmodeled effects were the least significant. Frequency dependent effects were found below 1 Hz, while plate dynamics affected the response above 5 Hz.

The predicted first bending frequency was higher than the measured natural frequency in both plates. In the first plate, the first bending frequency was predicted within 5%, but the second and third modal frequencies were roughly 20% higher than predicted values. In the second plate, the first three natural frequencies were within 11% of the predicted values.

- Unmodeled effects and material property uncertainties limit model accuracy.

Several unmodeled effects hampered the accuracy of model predictions. Inconsistencies in the manufacturing process resulted in significant differences in the actuation capabilities of each active ply. The actuation of the operational active ply in the first plate was significantly greater than that of the active plies in the second plate by almost a factor of two. The two active plies in the second plate induced equal amounts of bending, but differed significantly in the amount of induced twist. The reduced twist actuation of the weaker ply suggests a manufacturing defect which led to reduced anisotropy. Possible causes include broken or misaligned fibers and variations in the level of compression achieved in the active plies.

- Reduced stiffness of the active plies was attributed to low effective fiber stiffness in conjunction with an insufficient load transfer mechanism in the piezocomposite.

Measured stiffness properties of PFC's showed a large variation depending on the presence of a load path during the tests. The effective stiffness of the piezoceramic fibers was found to be roughly one half of the bulk ceramic value. This was most likely the result of breaks along the fibers. A steel shim bonded to the PFC resulted in much greater stiffness estimates for the fibers, most likely as a result of the stiff load transfer path which the steel offered in addition to the soft matrix.

- Initial plate deformation resulting from residual thermal stresses effected a passive bend/twist coupling in the antisymmetric laminates.

Geometric effects related to the initial deformation of the plates also affected the plate response. Residual thermal stresses in the antisymmetric lay-up during manufacture resulted in a significant initial twist deformation and a slight bend along the length of both plates. A preliminary analysis supports the observed bend/twist coupling in the plates.

- High field nonlinearities were found to be the same effects shown in pure piezoceramic actuators.
- Frequency dependent trends in the adaptive plate data support the theory for a resistive to capacitive transition in the electrical properties of the piezocomposite.

Additional tests were performed to further characterize the unmodeled effects observed in the actuation of the active plies. A high field nonlinearity exhibited in free PFC's as well as in the adaptive plates was found to be similar to the effects previously studied in pure piezoceramics. The frequency dependence was found to be related to the piezocomposite form of the actuators. Data suggest a transition between resistive and capacitive effects in the fiber/matrix system which occurs between 0.01 Hz and 0.1 Hz. The transition changes the electric field distribution in the composite, resulting in improved actuation capabilities below the transition.

- The dielectric mismatch between the fibers and the matrix, and a low effective fiber stiffness currently limit actuator performance.

In order to evaluate the performance of the PFC active plies, a perfect composite actuator was modeled. This perfect composite has ideal matrix and fiber properties to maximize the anisotropic actuation capabilities. A comparison of the measured and estimated properties for the current active plies showed that the perfect actuators exhibited much greater anisotropy, resulting in a larger induced stress and improved twist actuation

in the adaptive plate. The perfect actuator benefits from bulk ceramic stiffness properties for the fibers, and no dielectric mismatch affecting the electric field distribution.

This work has furthered the development of piezoelectric fiber composites as structural actuators. The adaptive plate model has been demonstrated as both a design and analysis tool, and further model enhancements will enable more accurate predictions for the plate response. The manufacturing process has been extended from small PFC actuators to large-scale, conformable, active plies incorporated in composite laminates. The current modeling and manufacturing capabilities demonstrated in this study can be extended to meet the requirements of specific smart structures applications.

5.2 RECOMMENDATIONS

Several improvements in the adaptive plate model will enable more accurate predictive capabilities. Incorporating a nonlinear piezoelectric coupling constant will account for high field effects in the active plies. More complex electromechanical models of the fiber/matrix system will improve modeling capabilities over a wide range of frequencies. This will include resistive/capacitive effects as well as polarization effects within the piezoceramic. Large deflection nonlinearities in the plate analysis will better predict the effects of the initial deformations, providing a better representation of the plate geometry and effective coupling properties.

The hybrid matrix is another area of continuing study. Improvements in the high dielectric filler material and chemical dispersants will enable a higher effective dielectric for the matrix. This reduction in the dielectric mismatch between the fibers and the matrix will greatly improve actuator performance. In addition, the properties of the matrix may be tailored to achieve more optimal electrical characteristics for the composite system. More advanced models of the electromechanical fiber/matrix system are needed.

The effective fiber stiffness in the PFC's used in this study was found to be significantly lower than the expected value for bulk ceramic materials. Experiments suggest that the brittle fibers require reinforcements to transfer structural loads across discontinuities. This may be achieved using embedded high modulus fibers within the active plies. For example, small diameter glass fibers may be used to improve the effective stiffness of the piezo fibers.

Additional improvements may be gained through the use of better active fibers. Fibers with a smaller diameter, smaller grain size, and possibly different composition may offer improved strength, stiffness, and actuation capabilities. Improved fiber manufacturing techniques may soon enable the manufacture of 40 μm fibers and 0.5 μm

grain sizes in piezoceramics. These developments should also help to reduce the cost of fibers in the future. Advances in the matrix, fibers, and overall composite will improve performance and the consistency of manufactured active plies.

An advanced electrode pattern has been developed for piezoelectric fiber composites to improve actuation capabilities. The interdigitated electrode (IDE) piezoelectric fiber composite has been investigated [Bent and Hagood, 1995]. This electrode pattern, consisting of parallel stripes across the electrode surface of alternating polarity, effectively moves the applied electric field into the plane of the active ply. The electrode stripes are placed perpendicularly to the fibers so that the electric field runs along the length of the fibers. This arrangement offers two advantages: actuation involves a d_{33} effect along the fibers and the effective fiber volume fraction is increased. The use of the direct piezoelectric effect (as opposed to the transverse effect) improves the actuation by a factor of three. In addition, the effective transverse piezoelectric coupling constant has the opposite sign, which enhances the piezoelectric anisotropy of the actuator. The improved fiber volume fraction enables a greater fraction of the electric field to pass through the piezoceramic, thus reducing the significance of the dielectric mismatch problem. Recent experiments have demonstrated a five-fold improvement in free strain capability for IDE-PFC's as compared with conventional PFC's.

The improvements that have been described will make PFC's a more desirable form of structural actuator in comparison with other smart materials and other anisotropic actuators. Future studies will use PFC active plies in acoustic noise control applications and rotorblade control applications. In the acoustics application, the active plies will be used to cancel structural vibrations which create undesirable acoustic noise, as in an aircraft fuselage. In the rotorblade, the active plies will either induce twist in the blade directly or actuate a trailing edge flap. In both applications, the high induced stress capabilities will be required to actuate the large structures without extreme weight penalties. The actuators will also be elements of a feedback control system, requiring well-characterized response. Other issues to be addressed include strength, fatigue life, reliability, and large-scale production potential.

APPENDIX A

Rayleigh Ritz MATLAB Code

The adaptive plate model described in Chapter 2 was implemented entirely in MATLAB using m-files. The hierarchy of the many subroutines which comprise the model is shown in Figure A-1. At the highest level is the main code and the global variable definitions. This code evaluates the generalized mass, stiffness, and forcing terms, and then solves for the plate response. The sound radiation prediction is also performed. Each of the energy integrals has a main subroutine and a corresponding integrand. The stiffness integral also requires the CLPT calculations. At the next level down, the properties of the passive and active plies are determined and assumed shape functions are evaluated at points on the plate. The bottom level includes the basic calculations for rotating material properties based on ply orientation, the numerical integration, and a legendre polynomial function.

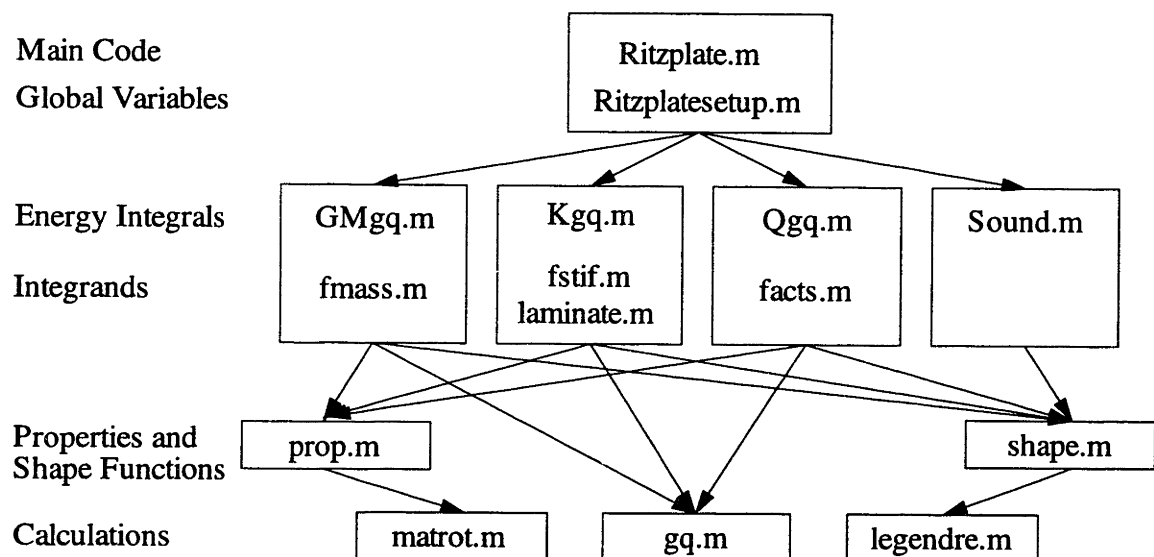


Figure A-1. M-file hierarchy in MATLAB adaptive plate model.

Ritzplatesetup.m (Global Variables for Ritz Code)

```

% ritzplatesetup declares global variables for ritzplate including geometry
% and boundary conditions as well as solution details.
global aa bb nplies nacts nshapes ushapes vshapes strainx strainy xbc ybc...
    display gqpts theta1 theta2 theta3 largedeflect q0
gqpts=8;           % grid points for gaussian quadrature (8,32,96)
nplies=2;         % number of plies
nacts=2;         % number of actuators
aa=143;          % length in x
bb=63;           % length in y
ushapes=0;       % x-direction (x,y,xy), (0->2)
vshapes=0;       % y-direction (y,x,xy), (0->2)
nshapes=5;       % u+v+w shapes
xbc=7;           % 0 for F-F, 11 for C-C, 22 for S-S, 1 for C-F,
                % 2 for S-F, 12 for C-S,
                % 3 for F-F legendre, 4 for S-F legendre,
                % 5 for F-F-F-F polynomials, 61 for C-F-F-F,
                % 62 for F-F-C-F, 7 for special C-F-F-F.
ybc=0;           % 0 for F-F, 11 for C-C, 22 for S-S, 1 for C-F,
                % 2 for S-F, 12 for C-S,
                % 3 for F-F legendre, 4 for S-F legendre. display=1;
                % 1 to plot static and dynamic modes
largedeflect=0;  % von Karman terms in strain-displacement
q0=[-5 0 0 0 0]; % linearized about this initial deflection
dnonlinear=0;   % iteration for nonlinear d-constants (ref. Lazarus)
lim=10;        % limit number of iterations
tol=.1;        % tolerance for convergence
strainx=0;     % strain values to check convergence in x and y
strainy=0;

```

Ritzplate.m (Main Rayleigh Ritz Code)

```

% John P. Rodgers; last modified 2/3/95;
% ritzplate uses matlab to determine laminate properties and perform a Ritz
% analysis of a plate. Engineering notation is used.
%%%%%% Setup %%%%%%%%%%%%%%%
clear;
clear global;
ritzplatesetup;
%t1=linspace(0,90,7);           % batch runs
%linspace(10,45,8);
%t3=linspace(0,90,2);
%for i=1:7
%    theta1=t1(i);
%    for j=1:1
%        theta2=t2(j);
%        for k=1:2
%            theta3=t3(k);
%%%%%%%% Calculate K matrix %%%%%%%%%
K=Kgg;           % gaussian quadrature (N/mm)
%%%%%%%% Calculate Q matrix %%%%%%%%%
if dnonlinear   % iterate for nonlinear d constants (ref. Lazarus)
for l=1:lim
    1
    oldstrainx=strainx;
    oldstrainy=strainy;
    Q=Qgg;       % (N/mm^2)
%%%%%%%% Calculate q vector - static solution %%%%%%%%%

```

```

    q=inv(K)*Q % (1/mm)
    scheck=shape(1,aa/2,bb/2)*q; % evaluate @ midpt.
    strainx=scheck(1)+(.79/2+.25/2)*scheck(4); % actuator strain in x
    strainy=scheck(2)+(.79/2+.25/2)*scheck(5); % actuator strain in y
    error=[(strainx-oldstrainx)/strainx (strainy-oldstrainy)/strainy]
    if (error(1)<tol)&(error(2)<tol)
        l=lim+1;
    end
end
else % no iteration -- assume linear d's
    Q=Qgg;
    q=inv(K)*Q;
end
% dnonlinear
ek=shape(1,aa/2,bb/2)*q; % strains and curvatures at (x,y)
%%%%%%%%%%%%%%%%%%%%%%%%%%%%%%%%%%%%%%%%%%%%%%%%%%%%%%%%%%%%%%%%%%%%%%%%
if display
    x=linspace(0,aa,10);
    y=linspace(0,bb,10);
    for j=1:10
        for k=1:10
            s=shape(0,x(j),y(k))';
            W_plot(j,:)=q'*s(:,3);
        end
    end
    def=max(max(W_plot))-min(min(W_plot)); % max deflection (mm)
    t=2*(W_plot(10,1)-W_plot(10,10))*90000/(aa*bb*pi);
    b=(W_plot(10,1)+W_plot(10,10))*90000/(2*aa^2*pi);
    [t b t/b]
    figure(1),mesh(W_plot);
end
%%%%%%%%%%%%%%%%%%%%%%%%%%%%%%%%%%%%%%%%%%%%%%%%%%%%%%%%%%%%%%%%%%%%%%%%
GM=GMgg; % (kg)
%%%%%%%%%%%%%%%%%%%%%%%%%%%%%%%%%%%%%%%%%%%%%%%%%%%%%%%%%%%%%%%%%%%%%%%%
% Calculate mode shapes and frequencies %%%%%%%%%
[lam2,I]=eig(inv(GM)*K*1000); % 1000 factor for kg^-1*N/mm (1/s^2)
% sort modes by frequency
% lam2 will contain ordered frequencies, and vect2 is ordered eigenvectors
[lam2,I]=sort(diag(lam2));
for i=1:nshapes
    for j=1:nshapes
        vect2(j,i)=vect(j,I(i));
    end
end
end
freq=sqrt(lam2)/(2*pi) % frequencies in Hz

if display % plot mode shapes
    figure(2);
    for j=1:10
        for k=1:10
            ss=shape(0,x(j),y(k))';
            plot1(j,k)=vect2(:,1)*ss(:,3);
            plot2(j,k)=vect2(:,2)*ss(:,3);
            plot3(j,k)=vect2(:,3)*ss(:,3);
            plot4(j,k)=vect2(:,4)*ss(:,3);
            if nshapes>=5
                plot5(j,k)=vect2(:,5)*ss(:,3);
                plot6(j,k)=vect2(:,6)*ss(:,3);
                plot7(j,k)=vect2(:,7)*ss(:,3);
                plot8(j,k)=vect2(:,8)*ss(:,3);
            end
        end
    end
end

```

```

        plot9(j,k)=vect2(:,9)'*ss(:,3);
        end
        if nshapes>=10
        plot10(j,k)=vect2(:,10)'*ss(:,3);
        plot11(j,k)=vect2(:,11)'*ss(:,3);
        plot12(j,k)=vect2(:,12)'*ss(:,3);
        end
    end

    end
    tq=2*90000*(plot1(10,1)-plot1(10,10))/(aa*bb*pi); %calculate twist and bend
    bq=90000*(plot1(10,1)+plot1(10,10))/(2*aa^2*pi);
    tq2=2*90000*(plot2(10,1)-plot2(10,10))/(aa*bb*pi);
    bq2=90000*(plot2(10,1)+plot2(10,10))/(2*aa^2*pi);
    [tq bq tq/bq;tq2 bq2 tq2/bq2;]
    subplot(2,2,1),mesh(plot1),title('mode 1');
    subplot(2,2,2),mesh(plot2),title('mode 2');
    subplot(2,2,3),mesh(plot3),title('mode 3');
    subplot(2,2,4),mesh(plot4),title('mode 4');
    end
    %%%% Forced Vibrations %%%%%%%%%%%%%%%%%%%%%%%%%%%%%%%
    w(1)=1*2*pi; % excitation frequency (input Hz)
    w(2)=5*2*pi; % second excitation frequency
    w(3)=10*2*pi;
    for j=1:3
        qd(:,j)=inv(K*1000-w(j)^2*GM)*Q*1000; % 1/mm
        s1=shape(0,aa,0)';
        s2=shape(0,aa,bb)';
        d1=qd(:,j)'*s1(:,3);
        d2=qd(:,j)'*s2(:,3);
        t1=2*90000*(d1-d2)/(aa*bb*pi);
        b1=90000*(d1+d2)/(2*aa^2*pi);
        tb(j,:)=[w(j)/(2*pi) t1 b1 t1/b1];
    end
    end
    %%%% Sound Radiation %%%%%%%%%%%%%%%%%%%%%%%%%%%%%%%
    out1=sound(qd(:,3),100,1.8,8)
    theta=linspace(0,Pi,9);
    polar(theta,out1),grid
    if display==1
    for j=1:10
        for k=1:10
            ss=shape(0,x(j),y(k))';
            dynplot1(j,k)=qd1'*ss(:,3);
            dynplot2(j,k)=qd2'*ss(:,3);
        end
    end
    end
    subplot(2,1,1),mesh(dynplot1);
    subplot(2,1,2),mesh(dynplot2);
    end

```

Prop.m (Returns Material Properties)

```

function [out]=prop(type,x,y,var)
ritzplatesetup;
% John P. Rodgers; modified 8/4/94;
% prop(plynumber/data type,x,y,property):
% if type=0, the function will return a full matrix of properties for the
% lay-up: [c11 c22 c12 c66 c16 c26 tply] (Laminate.m); when var=0, all
% actuators are ignored. otherwise, var specifies which actuator to include.

```

```

% if type is -2, the function will return [e31 e32 e36 zup zlo x1 x2 y1 y2 E3]
% for the actuator specified by var (Qgg.m).
% if type is -3, the function will return the mass/area; when var=0, all
% actuators are ignored; otherwise, the actuator specified by var is included.
% if type is -4, the actuator location (var) is returned: xmin,xmax,ymin,ymax.
##### Material Properties #####
% plane stress orthotropic or isotropic
%
%      N/mm^2          mm/V          kg/mm^3
%      EL      ET      VLT  GLT          d's      eps3^T density
mat=[130e3  10.5e3 .28 6e3  0 0 0 0 0 0 0 0 0 0 0 1.52e-6; % AS4/3501-6-1
     70e3   70e3   .33 26.6e3 0 0 0 0 0 0 0 0 0 0 0 2.9e-6; % Al-----2
     205e3  205e3  .30 77.0e3 0 0 0 0 0 0 0 0 0 0 0 7.86e-6; % Steel--3
     73e3   73e3  .17 31.2e3 0 0 0 0 0 0 0 0 0 0 0 2.2e-6; % Glass--4
     0      0      0 0      0 0 0 0 0 0 0 0 0 0 0 0 ; % air----5
     1e3   1e3   .3 0.7e3  0 0 0 0 0 0 0 0 0 0 0 1.1e-6; % electrode6

% orthotropic
%      c11 c22 c12 c33 c13 c23 c44 c55 c66^E / d31 d32 d33 d15 eps3^T density
127e3 127e3 80.2e3 117e3 84.7e3 84.7e3 23.0e3 23.0e3 23.5e3...
      -271e-9 -271e-9 593e-9 741e-9 1.73e-8 7.8e-6; % PZT5-H----7
24.3e3 5.89e3 2.97e3 14.9e3 7.19e3 2.5e3 1.67e3 1.67e3 1.52e3...
      0 0 346e-9 741e-9 1.73e-8 3.7e-6; % Pfiber----8
69.2e3 69.2e3 20.8e3 69.2e3 20.8e3 20.8e3 24.2e3 24.2e3 24.2e3 ...
      -166e-9 -166e-9 500e-9 741e-9 1.50e-8 7.6e-6; % G1195--9
127e3 127e3 80.2e3 117e3 84.7e3 84.7e3 23.0e3 23.0e3 23.5e3...
      -500e-6 -500e-6 1500e-6 741e-9 1.73e-8 7.8e-6; % FEM test--10
24.3e3 5.89e3 2.97e3 14.9e3 7.19e3 2.5e3 1.67e3 1.67e3 1.52e3 ...
      -31e-9 -6e-9 100e-9 200e-9 1.73e-8 3.7e-6; % G5 ----11

% plane stress anisotropic
%      s11 s22 s12 s16 s26 s66 0 0 0 / d31 d32 0 0 0 density
56.6e-6 70.9e-6 -19.6e-6 0 0 180e-6 0 0 0 ...
      -14.4e-9 -12.6e-9 0 0 0 5700e-9;... % PFC-----12
31.7e-6 57e-6 -13.4e-6 0 0 90e-6 0 0 0 ...
      0 0 0 0 0 4000e-9;... % dead PFC--13
41.1e-6 1e5 -11.5e-6 0 0 1e5 0 0 0 ...
      -450e-9 0 0 0 0 4e-6;]; % Perf.Comp-14

#####Layup##### mm
%mat angle thick 1<mat<7, active materials incorporated in act()
ply=[1 90 .134;6 0 .025;5 0 .135;6 0 .025;1 0 .134;...
     6 0 .025;5 0 .135;6 0 .025;1 90 .134;]; % SDM 95
##### Actuator Placement #####
%      mm          V/mm
%mat ply angle x1 x2 y1 y2 E3
act=[12 3 45 0 aa 0 bb 1000;...
     12 7 -45 0 aa 0 bb 0;]; % SDM 95
#####
if type==-4
    out=act(var,4:7);
else
    proppy=zeros(nplies,7);
for i=1:nplies % form rotated stiffness matrix
    m(i)=ply(i,1); % plane stress assumptions
    if mat(m(i))==0 % denominator, 1-vt1*vlt
        den=Inf; % air
    else
        den=1-mat(m(i),3)^2*mat(m(i),2)/mat(m(i),1);
    end
    C=[mat(m(i),1)/den mat(m(i),3)*mat(m(i),2)/den 0;...
      mat(m(i),3)*mat(m(i),2)/den mat(m(i),2)/den 0;...

```

```

    0 0 mat(m(i),4)];
    r=matrot(C,ply(i,2),2);
    propxy(i,:)=r(1,1) r(2,2) r(1,2) r(3,3) r(1,3) r(2,3) ply(i,3)];
end
if var>0
    % stiffness for active materials/plane stress
    m(act(var,2))=act(var,1);
    mvar=act(var,1);
    % plane stress--orthotropic
    if strainx==0
        d31=mat(mvar,10);
        d32=mat(mvar,11);
    else
        % nonlinear d iteration
        d31=2.54e-7+(1.94e-10/2.54e-7)*strainx; % Lazarus G1195
        d32=2.54e-7+(1.94e-10/2.54e-7)*strainy;
    end
    d=[0 0 0 0 mat(mvar,13) 0;0 0 0 mat(mvar,13) 0 0;...
        d31 d32 mat(mvar,12) 0 0 0;];
    if mvar<12
        % specify stiffness(9)
        C=[mat(mvar,1) mat(mvar,3) mat(mvar,5) 0 0 0;...
            mat(mvar,3) mat(mvar,2) mat(mvar,6) 0 0 0;...
            mat(mvar,5) mat(mvar,6) mat(mvar,4) 0 0 0;...
            0 0 0 mat(mvar,7) 0 0;...
            0 0 0 0 mat(mvar,8) 0;...
            0 0 0 0 0 mat(mvar,9)];
        S=inv(C);
        S2=S([1,2,6],[1,2,6]);
    else
        % specify plane stress compliance
        S2=[mat(mvar,1) mat(mvar,3) mat(mvar,4);...
            mat(mvar,3) mat(mvar,2) mat(mvar,5);...
            mat(mvar,4) mat(mvar,5) mat(mvar,6)];
    end
    % stiffness/compliance forms
    d2=d(3,[1,2,6]);
    in=[mat(mvar,14) d2;d2' S2];
    rot=matrot(in,act(var,3),1);
    C2=inv(rot(2:4,2:4));
    propxy(act(var,2),:)=C2(1,1) C2(2,2) C2(1,2) C2(3,3)...
        C2(1,3) C2(2,3) ply(act(var,2),3)];
end
if type==0
    out=propxy;
elseif type==-3
    rho=0;
    for j=1:nplies
        rho=rho+ply(j,3)*mat(m(j),15);
    end
    out=rho;
elseif type==-2
    th=0;
    for i=1:nplies
        th=th+ply(i,3);
    end
    k=var;
    z(1)=th/2;
    for i=1:nplies
        z(i+1)=z(i)-ply(i,3);
    end
    zlo=z(act(k,2)+1);
    zup=z(act(k,2));

```

```

        e=C2*rot(2:4,1);
        out=[e' zup zlo act(k,4:8)];
    end
end

```

GMgq.m (Generalized Mass)

```

function [out]=GMgq
ritzplatesetup;
rho0=prop(-3,0,0,0);
a=aa;
b=bb;
GM=gq('fmass',0,a,0,b,rho0);
for i=1:nacts
    rho=prop(-3,0,0,i)-rho0;
    lims=prop(-4,0,0,i);
    GM=GM+gq('fmass',lims(1),lims(2),lims(3),lims(4),rho);
end
out=GM;
return;

```

Kgq.m (Generalized Stiffness)

```

function [out]=Kgq
ritzplatesetup;
lam0=laminate(0);
a=aa;
b=bb;
K=gq('fstif',0,a,0,b,lam0);
for i=1:nacts
    lam=laminate(i);
    lims=prop(-4,0,0,i);
    K=K+gq('fstif',lims(1),lims(2),lims(3),lims(4),lam)...
        -gq('fstif',lims(1),lims(2),lims(3),lims(4),lam0);
end
out=K;
return;

```

Qgq.m (Actuator Forcing)

```

function [out]=Qgq
% Qgq sets up for the calculation of the Q vector. Note that Q currently
% lumps the effects of all actuators.
ritzplatesetup;
Q=zeros(nshapes,1);
for i=1:nacts
    dat=prop(-2,0,0,i);% [e31 e32 e36 zup zlo x1 x2 y1 y2 E3] %orthotropic material
    e=dat(1:3) '
    M=e*dat(10)*.5*(dat(4)^2-dat(5)^2)
    N=e*dat(10)*(dat(4)-dat(5)) Q=Q+gq('facts',dat(6),dat(7),dat(8),dat(9),1)*[N;M;];
end
out=Q;
return;

```

Fmass.m (Generalized Mass Integrand)

```

function [out]=fmass(x,y,rho)
% [out]=fmass(x,y,rho)

```

```

answer=shape(0,x,y) '*rho*shape(0,x,y);
out=answer;
return;

```

Fstif.m (Generalized Stiffness Integrand)

```

function [out]=fstif(x,y,stiff)
% [out]=fstif(x,y)
answer=shape(1,x,y) '*stiff*shape(1,x,y);
out=answer;
return;

```

Facts.m (Generalized Force Integrand)

```

function [out]=facts(x,y,const)
% [out]=facts(x,y,const)
out=shape(1,x,y) ' ;
return;
end

```

Gq.m (Gaussian Quadrature)

```

function [value]=gq(func,a1,a2,b1,b2,const)
% gq(func,a1,a2,b1,b2,const) returns the integral of func'*const*func between % a and
b using up to a 96-point Gaussian quadrature. Data comes from
% gaussdata.mat
ritzplatesetup;
points=gqpts;
load gaussdata
if points==8
    gpt=gpt8;
    gwt=gwt8;
    n=4;
elseif points==32
    gpt=gpt32;
    gwt=gwt32;
    n=16;
else
    %96 pts
    gpt=gpt96;
    gwt=gwt96;
    n=48;
end
xm=.5*(a1+a2); % x1+x2
xr=.5*(a1-a2); % x1-x2
if func=='facts'
    ss=zeros(nshapes,6);
else
    ss=zeros(nshapes,nshapes); % zero the sum of iterations on x end
for i=1:n % outer integral;use gpt16 with gwt32
    dx=xr*gpt(i);
    ym1=.5*(b1+b2); % y1+y2 @ xm+dx
    yr1=.5*(b1-b2); % y1-y2
    ym2=.5*(b1+b2); % y1+y2 @ xm-dx
    yr2=.5*(b1-b2); % y1-y2
    if func=='facts'
        ssy1=zeros(nshapes,6);
        ssy2=zeros(nshapes,6);
    else

```



```

        ssy1=zeros(nshapes,nshapes);           % zeros for sum of y-iterations
        ssy2=zeros(nshapes,nshapes);
    end
    for j=1:n                                 % inner integral
        dy1=yr1*gpt(j);
        xx1=xm+dx;
        yy1=yml+dy1;
        yy2=yml-dy1;
        ssy1=ssy1+gwt(j)*(feval(func,xx1,yy1,const)+feval(func,xx1,yy2,const));
        dy2=yr2*gpt(j);
        xx1=xm-dx;
        ssy2=ssy2+gwt(j)*(feval(func,xx1,yy1,const)+feval(func,xx1,yy2,const));
    end
    ss=ss+gwt(i)*(yr1*ssy1+yr2*ssy2);        % *yr to scale
    end
    value=xr*ss;                             % *xr to scale
    % routine is double integral form of routine found in Numerical Recipes-FORTRAN
    return;
end

```

Laminate.m (CLPT Calculation)

```

function [out]=laminate(n)
ritzplatesetup;
% laminate(n) returns laminate properties [A B;B D] for the laminate without any
%actuators if n=0, and for the laminate including only the nth actuator if n is
positive.
p=prop(0,0,0,n);      % [c11 c22 c12 c66 c16 c26 th]
th=0;
for i=1:nplies
    th=th+p(i,7);
end
A=zeros(3);
B=zeros(3);
D=zeros(3);
ztop=th/2;
zbot=ztop;
for i=1:nplies
    ztop=zbot;
    zbot=zbot-p(i,7);
    z1=ztop-zbot;
    z2=(ztop^2-zbot^2)/2;
    z3=(ztop^3-zbot^3)/3;
    c=[p(i,1) p(i,3) p(i,5);p(i,3) p(i,2) p(i,6);p(i,5) p(i,6) p(i,4)];
    A=A+z1*c;      % [N/mm]
    B=B+z2*c;      % [N]
    D=D+z3*c;      % [N-mm]
end
out=[A B;B D;];
return;

```

Matrot.m (Property Rotations)

```

function [out]=matrot(in,thet,flag)
% matrot(input, theta, flag) rotates in-plane.
% in = matrix of input properties
% thet = angle of rotation about 3-axis in degrees, positive clockwise
% flag = 1 for stress independent (compliance transformation or [eps d; d' s];)

```

```

% 2 for strain independent (stiffness transformation or [eps e;-e' c;])
% size of input property matrix determines transformation type
% 3x3 for reduced stiffness/compliance
% 4x4 for reduced piezo matrix
% 6x6 for stiffness/compliance
% 9x9 for full piezo matrix
[nr,nc]=size(in);
Pi=4*atan(1);
c=cos(Pi*thet/180);
s=sin(Pi*thet/180);
t1=[c s 0;...                               % first order transformation
    -s c 0;...
    0 0 1;];
t2=[c^2 s^2 0 0 0 -2*c*s;...                % stress transformation (2nd order)
    s^2 c^2 0 0 0 2*c*s;...                % ref: C-Y Chia, Nonlin An. Plates
    0 0 1 0 0 0;...                        % -- inverted for opposite rotation
    0 0 0 c s 0;...
    0 0 0 -s c 0;...
    c*s -c*s 0 0 0 c^2-s^2;];
t3=t2([1,2,6],[1,2,6]);                      % reduction
t4=[c^2 s^2 0 0 0 -c*s;...                  % strain transformation (2nd order)
    s^2 c^2 0 0 0 c*s;...
    0 0 1 0 0 0;...
    0 0 0 c s 0;...
    0 0 0 -s c 0;...
    2*c*s -2*c*s 0 0 0 c^2-s^2;];
t5=t4([1,2,6],[1,2,6]);                      % reduction
if nr~=nc
    return;
end
if nr==3
    Rstress=t3;
    Rstrain=t5;
    if flag==1                               % compliance
        out=(Rstrain\in)*Rstress;
    end;
    if flag==2                               % stiffness
        out=(Rstress\in)*Rstrain;
    end;
end;
if nr==4
    Rstress=[1 zeros(1,3);zeros(3,1) t3;];
    Rstrain=[1 zeros(1,3);zeros(3,1) t5;];
    if flag==1                               % [eps d;d' s;]
        out=(Rstrain\in)*Rstress;
    end;
    if flag==2                               % [eps e;-e' c;]
        out=(Rstress\in)*Rstrain;
    end;
end;
if nr==6
    tstress=t2;
    tstrain=t4;
    if flag==1                               % compliance
        out=(tstrain\in)*tstress;
    end;
    if flag==2                               % stiffness
        out=(tstress\in)*tstrain;
    end;
end;

```

```

        end;
    end;
    if nr==9
        tstress=[t1,zeros(3,6);zeros(6,3),t2;];
        tstrain=[t1,zeros(3,6);zeros(6,3),t4;];
        if flag==1
            out=(tstrain\in)*tstress;           % [eps d;d' s;]
        end;
        if flag==2
            out=(tstress\in)*tstrain;         % [eps e;-e' c;]
        end;
    end;
end;
return;

```

Shape.m (Assumed Shape Functions)

```

function [out]=shape(d,x,y)
% shape(d,x,y) evaluates matrix of shape function derivatives at the
% point (x,y) if d=1; evaluates matrix of shape functions at (x,y) if d=0;
% evaluates d/dx and d/dy if d=-1. Uses beam functions or other specified
% shape functions. Input [mm];
ritzplatesetup;
a=aa;
b=bb;
Pi=pi;
numu=ushapes;
numv=vshapes;
numw=nshapes-numu-numv;
deriv=zeros(6,nshapes);
func=zeros(3,nshapes);
%%%%%In plane deflections %%%%%%%%%%%%%%%%%%%%%%%%%%%%%%%%%%%%%%%%%%%%%%%%%%%%%%%%%%%%%%%%%%%%%%%%%%%%%%% %
    f(x,y)          df/dx          df/dy   [1/mm]
fu=[  x/a           1/a           0;...
      (y-b/2)/b     0             1/b;...
      x*(y-b/2)/(a*b) (y-b/2)/(a*b) x/(a*b);];
fv=[  (y-b/2)/b     0             1/b;...
      x/a           1/a           0;...
      x*(y-b/2)/(a*b) (y-b/2)/(a*b) x/(a*b);];
if (xbc==0) | (xbc==3) | (xbc==5) | (xbc==62)
    n=[1 2];
elseif (xbc==1) | (xbc==10) | (xbc==2) | (xbc==20) | (xbc==4) | (xbc==61) | (xbc==7)
    n=[1 3];
end
for i=1:numu
    deriv(:,i)=[fu(n(i),2);0;fu(n(i),3);0;0;0];
    func(1,i)=fu(n(i),1);
end
if (ybc==0) | (ybc==3) | (ybc==5) | (xbc==61) | (xbc==7)
    n=[1 2];
elseif (ybc==1) | (ybc==10) | (ybc==2) | (ybc==20) | (ybc==4) | (xbc==62)
    n=[1 3];
end
for i=(numu+1):(numu+numv)
    j=i-numu;
    deriv(:,i)=[0;fv(n(j),3);fv(n(j),2);0;0;0];
    func(2,i)=fv(n(j),1);
end
%%%%% Out of plane deflections %%%%%%%%%%%%%%%%%%%%%%%%%%%%%%%%%%%%%%%%%%%%%%%%%%%%%%%%%%%%%%%%%%%%%%%%%%%%%%%

```

```

if (xbc==5) | (xbc==61) | (xbc==62)
    if xbc==5
        num=[1 2 3 4 5];
    elseif xbc==61
        num=[1 2 4 5];
        y=y-b/2; % x-clamped
    else
        num=[1 3 4 5];
        x=x-a/2; % y-clamped
    end
%
% f(x,y)      d2f/dx2      d2f/dy2      d2f/dxdy
fw=[ x*y/(a*b)      0      0      1/(a*b);...
    (x/a)^2      2/a^2      0      0;...
    (y/b)^2      0      2/b^2      0;...
    (y/b)*(x/a)^2  (y/b)*(2/a^2)      0      (1/b)*(2*x/a^2);...
    (x/a)*(y/b)^2      0      (x/a)*(2/b^2)  (1/a)*(2*y/b^2)];
for i=(numu+numv+1):(numu+numv+numw)
    j=num(i-numu-numv);
    deriv(:,i)=[0;0;0;-fw(j,2);-fw(j,3);-2*fw(j,4)];
    func(3,i)=fw(j,1);
end
elseif xbc==7 % Jensen,Crawley,Dugundji
    lam=[1.875104 4.694091]/a;
    sig=[.734096 1.018466];
fw=[sin(Pi*x/(2*a))*(y-b/2)/b ...
    -(Pi/(2*a))^2*sin(Pi*x/(2*a))*(y-b/2)/b 0 ...
    (Pi/(2*a*b))*cos(Pi*x/(2*a));...
    sin(3*Pi*x/(2*a))*(y-b/2)/b ...
    -(3*Pi/(2*a))^2*sin(3*Pi*x/(2*a))*(y-b/2)/b 0 ...
    (3*Pi/(2*a*b))*cos(3*Pi*x/(2*a));...
    (x/a)*(1-x/a)*(4*((y-b/2)/b)^2-1/3) (-2/a^2)*(4*((y-b/2)/b)^2-1/3) ...
    (x/a)*(1-x/a)*(8/b^2) (1/a-2*x/a^2)*8*(y-b/2)/b^2;...
    cosh(lam(1)*x)-cos(lam(1)*x)-sig(1)*(sinh(lam(1)*x)-sin(lam(1)*x)) ...
    lam(1)^2*(cosh(lam(1)*x)+cos(lam(1)*x)-...
    sig(1)*(sinh(lam(1)*x)+sin(lam(1)*x))) 0 0;...
    cosh(lam(2)*x)-cos(lam(2)*x)-sig(2)*(sinh(lam(2)*x)-sin(lam(2)*x)) ...
    lam(2)^2*(cosh(lam(2)*x)+cos(lam(2)*x)-...
    sig(2)*(sinh(lam(2)*x)+sin(lam(2)*x))) 0 0;];
for i=(numu+numv+1):(numu+numv+numw)
    j=i-numu-numv;
    deriv(:,i)=[0;0;0;-fw(j,2);-fw(j,3);-2*fw(j,4)];
    func(3,i)=fw(j,1);
end
else % beam functions and legendre
    lam1(1:5)=[4.73004074 7.85320462 10.9956078 14.1371655 17.2787597];%Blevins
    sig1(1:5)=[.982502215 1.000777312 .99996645 1.00000145 .999999937];
    lam2=[1 3 5 2 4 7 9 6 8];
    lam3(1:5)=[1.87510407 4.69409113 7.85475744 10.99554073 14.13716839];
    sig3(1:5)=[.734095514 1.018467319 .999224497 1.000033553 .999998550];
    lam4(1:5)=[3.92660231 7.06858275 10.21017612 13.35176878 16.49336143];
    sig4(1:5)=[1.000777304 1.000001445 1 1 1];
    legff(1:5)=[0 1 2 3 4];
    legsf(1:5)=[1 2 3 4 5];
    ns=sqrt(numw);
    for i=6:ns
        lam1(i)=(2*i+1)*Pi/2;
        sig1(i)=1;
        lam3(i)=(2*i-1)*Pi/2;
    end
end

```

```

        sig3(i)=1;
        lam4(i)=(4*i+1)*Pi/4;
        sig4(i)=1;
        legff(i)=i-1;
        legsf(i)=i;
    end
    if xbc==0
        lamx=[0 0 lam1(1:ns-2)]'/a;
        sigx=[0 0 sig1(1:ns-2)];
    elseif xbc==11
        lamx=lam1(1:ns)'/a;
        sigx=sig1(1:ns);
    elseif xbc==22
        lamx=lam2(1:ns) '*Pi/a;
    elseif (xbc==1) | (xbc==10)
        lamx=lam3(1:ns)'/a;
        sigx=sig3(1:ns);
    elseif (xbc==12) | (xbc==21)
        lamx=lam4(1:ns)'/a;
        sigx=sig4(1:ns);
    elseif (xbc==2) | (xbc==20)
        lamx=[0 lam4(1:ns-1)]'/a;
        sigx=[0 sig4(1:ns-1)];
        x=a-x;
        % first derivatives negative
    elseif xbc==3
        lamx=legff;
        x=2*x/a-1;
        % scale for -1 to 1
        xconst=a/2;
        % constant for chain rule
    else % xbc==4
        lamx=legsf;
        x=1-2*x/a;
        % scale for 1 to -1
        xconst=-a/2;
    end
    if ybc==0
        lamy=[0 0 lam1(1:ns-2)]'/b;
        sigy=[0 0 sig1(1:ns-2)];
    elseif ybc==11
        lamy=lam1(1:ns)'/b;
        sigy=sig1(1:ns);
    elseif ybc==22
        lamy=lam2(1:ns) '*Pi/b;
    elseif (ybc==1) | (ybc==10)
        lamy=lam3(1:ns)'/b;
        sigy=sig3(1:ns);
    elseif (ybc==12) | (ybc==21)
        lamy=lam4(1:ns)'/b;
        sigy=sig4(1:ns);
    elseif (ybc==2) | (ybc==20)
        lamy=[0 lam4(1:ns-1)]'/b;
        sigy=[0 sig4(1:ns-1)];
        y=b-y;
        % first derivatives negative by chain rule
    elseif ybc==3
        lamy=legff;
        y=2*y/b-1;
        yconst=b/2;
    else % ybc==4
        lamy=legsf;
        y=1-2*y/b;
    end

```

```

        yconst=-b/2;
c=cos(lamx*x);
s=sin(lamx*x);
ch=cosh(lamx*x);
sh=sinh(lamx*x);
if xbc==0
    X=[ch+c-sigx'.*(sh+s) lamx.*(sh-s-sigx'.*(ch+c)) ...
        lamx.*lamx.*(ch-c-sigx'.*(sh-s))];
    X(1,:)= [1 0 0];
    X(2,:)= [x/a-1/2 1/a 0];
elseif (xbc==11) | (xbc==1) | (xbc==10) | (xbc==12) | (xbc==21)
    X=[ch-c-sigx'.*(sh-s) lamx.*(sh+s-sigx'.*(ch-c)) ...
        lamx.*lamx.*(ch+c-sigx'.*(sh+s))];
elseif xbc==22
    X=[s lamx.*c -lamx.*lamx.*s];
elseif (xbc==2) | (xbc==20)
    X=[ch+c-sigx'.*(sh+s) -lamx.*(sh-s-sigx'.*(ch+c)) ...
        lamx.*lamx.*(ch-c-sigx'.*(sh-s))];
    X(1,:)= [x/a-1 -1/a 0];
elseif (xbc==3)
    for i=1:ns
        X(i,:)= [legendre(lamx(i),x,xconst,0) ...
            legendre(lamx(i),x,xconst,1) legendre(lamx(i),x,xconst,2)];
    end
else %xbc==4
    for i=1:ns
        % subtract 1 to zero left endpoint
        X(i,:)= [legendre(lamx(i),x,xconst,0)-1 ...
            legendre(lamx(i),x,xconst,1) legendre(lamx(i),x,xconst,2)];
    end
end
c=cos(lamy*y);
s=sin(lamy*y);
ch=cosh(lamy*y);
sh=sinh(lamy*y);
if ybc==0
    Y=[ch+c-sigy'.*(sh+s) lamy.*(sh-s-sigy'.*(ch+c)) ...
        lamy.*lamy.*(ch-c-sigy'.*(sh-s))];
    Y(1,:)= [1 0 0];
    Y(2,:)= [y/b-1/2 1/b 0];
elseif (ybc==11) | (ybc==1) | (ybc==10) | (ybc==12) | (ybc==21)
    Y=[ch-c-sigy'.*(sh-s) lamy.*(sh+s-sigy'.*(ch-c)) ...
        lamy.*lamy.*(ch+c-sigy'.*(sh+s))];
elseif ybc==22
    Y=[s lamy.*c -lamy.*lamy.*s];
elseif (ybc==2) | (ybc==20)
    Y=[ch+c-sigy'.*(sh+s) -lamy.*(sh-s-sigy'.*(ch+c)) ...
        lamy.*lamy.*(ch-c-sigy'.*(sh-s))];
    Y(1,:)= [y/b-1 -1/b 0];
elseif (ybc==3)
    for i=1:ns
        Y(i,:)= [legendre(lamy(i),y,yconst,0) ...
            legendre(lamy(i),y,yconst,1) legendre(lamy(i),y,yconst,2)];
    end
else % ybc==4
    for i=1:ns
        Y(i,:)= [legendre(lamy(i),y,yconst,0)-1 ...
            legendre(lamy(i),y,yconst,1) legendre(lamy(i),y,yconst,2)];
    end
end

```

```

end
for j=1:ns
    for k=1:ns
        p=ns*(j-1)+k;
        fw=[X(j,1)*Y(k,1) X(j,3)*Y(k,1) X(j,1)*Y(k,3) X(j,2)*Y(k,2)];
        q=p+numu+numv;
        deriv(:,q)=[0;0;0;-fw(2);-fw(3);-2*fw(4)]; % second der's
        slope(:,q)=[X(j,2)*Y(k,1);X(j,1)*Y(k,2)]; % first der's
        func(3,q)=fw(1); % functions
    end
end
end
end % function type
if d==1
    out=deriv;
elseif d==0
    out=func;
else
    out=slope;
end
return;

```

Legendre.m (Legendre Polynomial Shape Functions)

```

function [out]=legendre(n,x,a,d)
% legendre(n,x,a,d) evaluates the dth derivative of the nth legendre
% polynomial at x. Derivatives are scaled for chain rule using a.
n=n+1; %nth polynomial is (n+1)th element of vector.
d=d+1;
P(1,:)=[1 0 0];
P(2,:)=[x 1 0];
for i=2:n-1
    P(i+1,1)=((2*i-1)*x*P(i,1)-(i-1)*P(i-1,1))/i;
    P(i+1,2)=((2*i-1)*(P(i,1)+x*P(i,2))-(i-1)*P(i-1,2))/i;
    P(i+1,3)=((4*i-2)*P(i,2)+(2*i-1)*x*P(i,3)-(i-1)*P(i-1,3))/i;
end
% recurrence relation 12.17 from Arfken, Mathematical Methods for Physicists
if d==1
    out=P(n,d);
elseif d==2
    out=P(n,d)/a;
elseif d==3
    out=P(n,d)/a^2;
end
return;

```

Sound.m (Sound Radiation Integral)

```

function [value]=gq4(q,f,R,points)
% sound(q,f,R,points) returns an array of pressures over an arc of radius R (m)
% integrated over a baffled plate using the Rayleigh integral using up
% to a 96-point Gaussian quadrature. Data comes from gaussdata.
% f is the frequency in Hz and q is the eigenvector for the mode shape.
ritzplatesetup;
a1=0;
a2=aa;
b1=0;
b2=bb;
%8,32,96

```

```

load gaussdata
if points==8
    gpt=gpt8;
    gwt=gwt8;
    n=4;
elseif points==32
    gpt=gpt32;
    gwt=gwt32;
    n=16;
else %96 pts
    gpt=gpt96;
    gwt=gwt96;
    n=48;
end
rho=1.29e-9;          % kg/mm^3
c=345e3;              % mm/s
w=2*pi*f;
theta=linspace(0,pi,9);
value(1:4)=[0 0 0 0]; %%%%%%%%%%%
R=1000*R;             % mm
x1=(a1+a2)/2; %linspace(-R,R,9)+(a1+a2)/2;%%%%%%%%%%
y1=(b1+b2)/2; %linspace(-R,R,9)+(b1+b2)/2;%%%%%%%%%%
i=sqrt(-1);
for k=1:9              %%%%%%%%%%%
    x=(a1+a2)/2+R*cos(theta(k));
    y=(b1+b2)/2;
    z=R*sin(theta(k));
    xm=.5*(a1+a2);      % a=x1+x2
    xr=.5*(a1-a2);      % a=x1-x2
    ss=0;                % zero the sum of iterations on x
    for l=1:n            % outer integral
        dx=xr*gpt(l);
        ym1=.5*(b1+b2); % b=y1+y2 @ xm+dx
        yr1=.5*(b1-b2); % b=y1-y2
        ym2=.5*(b1+b2); % b=y1+y2 @ xm-dx
        yr2=.5*(b1-b2); % b=y1-y2
        ssy1=0;          % zeros for sum of y-iterations
        ssy2=0;
        for m=1:n        % inner integral
            dy1=yr1*gpt(m);
            xx1=xm+dx;
            yy1=ym1+dy1;
            yy2=ym1-dy1;
            A1=q'*shape(0,xx1,yy1)'; % deflection vector
            A2=q'*shape(0,xx1,yy2)';
            dA1=q'*shape(-1,xx1,yy1)'; % [dA/dx dA/dy]
            dA2=q'*shape(-1,xx1,yy2)';
            N1=[-dA1 1]; % normal vector
            N2=[-dA2 1];
            ssy1=ssy1+gwt(m)*(A1*N1'*real(exp(i*w*...
                norm([x y z]-[xx1 yy1 0])/c))*N1/...
                (norm([x y z]-[xx1 yy1 0])*norm(N1))+...
                A2*N2'*real(exp(i*w*norm([x y z]-[xx1 yy2 0])/c))*N2/...
                (norm([x y z]-[xx1 yy2 0])*norm(N2)));
            dy2=yr2*gpt(m);
            xx1=xm-dx;
            A1=q'*shape(0,xx1,yy1)';
            A2=q'*shape(0,xx1,yy2)';

```



```

dA1=q'*shape(-1,xx1,yy1)';           % [dA/dx dA/dy]
dA2=q'*shape(-1,xx1,yy2)';
N1=[-dA1 1];                          % [i j k] normal
N2=[-dA2 1];
ssy2=ssy2+gwt(m)*(A1*N1'*real(exp(i*w*...
    norm([x y z]-[xx1 yy1 0])/c))*N1/...
    (norm([x y z]-[xx1 yy1 0])*norm(N1))+...
    A2*N2'*real(exp(i*w*norm([x y z]-[xx1 yy2 0])/c))*N2/...
    (norm([x y z]-[xx1 yy2 0])*norm(N2)));
end
ss=ss+gwt(1)*(yr1*ssy1+yr2*ssy2);      % *yr to scale
end
value(k)=norm(real(xr*ss));             % *xr to scale
% routine is double integral form of routine found in Numerical Recipes-FORTRAN
end
value=20*log(((w^2*rho*1000/(2*pi))*value)/2e-5); % SPrL(dB re 20uPa)
return;
end

```


APPENDIX **B**

Shape Functions

The five shape functions used to model the out-of-plane deflections of the adaptive plate were [Jensen *et al*, 1982]:

$$w(x,y) = \sin\left(\frac{\pi x}{2a}\right) \frac{y}{b} \quad (78)$$

$$w(x,y) = \sin\left(\frac{3\pi x}{2a}\right) \frac{y}{b} \quad (79)$$

$$w(x,y) = \frac{x}{a} \left(1 - \frac{x}{a}\right) \left(\frac{4y^2}{b^2} - \frac{1}{3}\right) \quad (80)$$

$$w(x,y) = \cosh\left(\frac{\lambda_1 x}{a}\right) - \cos\left(\frac{\lambda_1 x}{a}\right) - \sigma_1 \left[\sinh\left(\frac{\lambda_1 x}{a}\right) - \sin\left(\frac{\lambda_1 x}{a}\right) \right] \quad (81)$$

$$w(x,y) = \cosh\left(\frac{\lambda_2 x}{a}\right) - \cos\left(\frac{\lambda_2 x}{a}\right) - \sigma_2 \left[\sinh\left(\frac{\lambda_2 x}{a}\right) - \sin\left(\frac{\lambda_2 x}{a}\right) \right] \quad (82)$$

where

$$\lambda_1=1.875104, \lambda_2=4.694091, \sigma_1=0.734096, \sigma_2=1.018466$$

APPENDIX **C**

Rayleigh Ritz Plate Model Validation

This section provides additional comparisons between the predictions for natural frequencies and mode shapes of the Rayleigh Ritz adaptive plate model and referenced data. The Rayleigh Ritz model described in Chapter 2 was validated for passive isotropic plates through a comparison with referenced experimental data from Blevins [1987] for both free and cantilevered plates. In addition, FEM predictions are provided as a comparison. The Rayleigh Ritz model used combinations of standard beam shape functions, which are the exact solutions for beam modes. A pair of one-dimensional functions (e.g. $f(x)$, $g(y)$) is multiplied together to create plate shape functions. The product of the functions satisfies the geometric boundary conditions for the plate. A total of 25 combinations of beam functions were used, with a 32 by 32 point Gaussian quadrature grid for evaluating the integrals. ANSYS 4 software was used to produce the FEM for the plates. For the free plate, a 12 by 12 grid was used with 350 degrees of freedom. The cantilevered plate used a 10 by 10 grid with 300 degrees of freedom. The nodal spacing and degrees of freedom were selected for adequate convergence of the solutions. Both plates were aluminum, which has a modulus of 70 GPa. The free plate had dimensions of 292 mm by 292 mm with a thickness of 0.79 mm. The cantilevered plate had dimensions of 1 m by 0.3 m with a thickness of 6 mm. Table C-1 summarizes the predicted natural frequencies of the free plate while Table C-2 summarizes those of the cantilevered plate. All frequencies are in Hertz, and the mode designations represents the x and y beam function combinations from Blevins. For example, the digit '1' represents the simplest beam shape for the particular boundary conditions.

Table C-1. Comparison of Data and Model Predictions for Free Aluminum Plate

mode	Rayleigh Ritz	ANSYS	Blevins	Ritz Error	ANSYS Error
22	29.4	30.5	29.9	1.5	2.0
13	43.2	44.3	43.8	1.5	1.0
31	54.5	54.9	54.1	0.7	1.5
32	76.8	78.4	77.6	1.0	1.1
23	76.8	78.4	77.6	1.0	1.1
33	141.0	143.1	136.3	3.5	5.0

Table C-2. Comparison of Data and Model Predictions for Cantilevered Aluminum Plate

mode	Rayleigh Ritz	ANSYS	Blevins	Ritz Error	ANSYS Error
11	4.9	4.9	4.9	-0.4	-1.7
21	30.7	30.2	30.8	-0.1	-1.7
12	33.0	32.4	33.3	-1.0	-2.9
31	86.3	84.6	94.9	-9.1	-10.9
22	103.2	101.0	101.0	2.2	0.0

The Rayleigh Ritz model was extremely accurate in predicting the modes of the plates. For the free plate, the predictions for the first 5 modes were within 1.5% of the experimental values. For the cantilevered plate, the predictions were within 10%. In both cases, the Rayleigh Ritz model was more accurate than the FEM.

APPENDIX **D**

Acoustic Noise Control

One future application of piezoelectric fiber composites will involve the control of structurally radiated noise. PFC actuators embedded in plates will be used to cancel structural vibrations which create sound waves in the surrounding medium. Predictions for sound radiation from plates based on surface vibration will be a useful tool in this application.

One particular problem is to determine the sound radiated from a plate induced by embedded actuators. The Rayleigh Ritz model previously described can be used to solve for the dynamic mode shape of the plate. Once the deflection shape is determined from the dynamic solution at a given excitation frequency, the sound pressure radiated from the plate can be estimated. The theory for the calculations was obtained from Norton [1989]. The equations for the sound pressure are most easily evaluated using a radial vector originating from a corner of the undeformed plate, as shown in Figure D-1. The vector \mathbf{l} begins at the origin and extends to some point in space where the sound power level, P , needs to be estimated. \mathbf{l}_0 is the vector from the origin to a point on the plate being considered. $\hat{\mathbf{n}}$ is the unit normal to the surface of the plate. The normal surface velocity is $\mathbf{u}_n(\mathbf{l}_0)$, and is defined

$$\mathbf{u}_n(\mathbf{l}_0) = \omega w(x, y) \hat{\mathbf{n}} \quad (83)$$

where ω is the excitation frequency and $w(x, y)$ is the deflection shape.

The assumption of a harmonic source allows for the simplification,

$$P(\mathbf{l}, t) = P(\mathbf{l})e^{j\omega t} \quad (84)$$

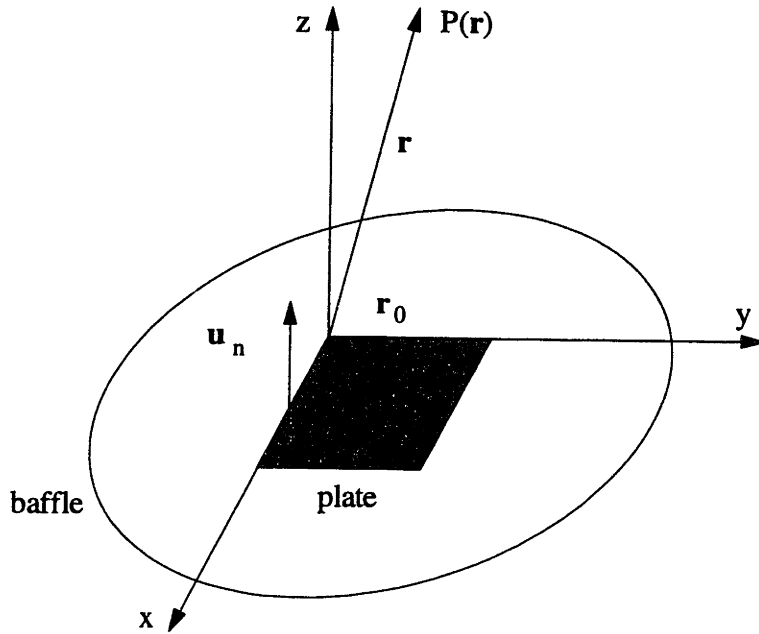


Figure D-1. Coordinates for sound power level calculations.

Removing the time dependence from the expression for the sound power radiated results in the Kirchhoff-Helmholtz integral equation:

$$P(\mathbf{l}) = \int_S \left\{ P(\mathbf{l}_0) \frac{\partial G_\omega(\mathbf{l}, \omega / \mathbf{l}_0, \omega)}{\partial \hat{\mathbf{n}}} + j\omega\rho_0 \mathbf{u}_n(\mathbf{l}_0) G_\omega(\mathbf{l}, \omega / \mathbf{l}_0, \omega) \right\} dS \quad (85)$$

where $P(\mathbf{l}_0)$ is the surface pressure distribution, G_ω is the frequency domain Green's function solution to the wave equation for a harmonic source, S is the vibrating surface, and ρ_0 is the density of the fluid medium. For a point source, the Green's function is:

$$G_\omega = \frac{e^{jkl}}{4\pi l} \quad (86)$$

In this expression, k is the wavenumber, defined:

$$k = \frac{\omega}{c} \quad (87)$$

where c is the wave speed. The scalar l is defined:

$$l = |\mathbf{l} - \mathbf{l}_0| \quad (88)$$

Assuming that the surface pressure is negligible and that the plate approximates a planar source mounted in an infinitely large rigid baffle, equation (82) can be reduced to Rayleigh's equation for radiated sound pressure:

$$P(\mathbf{l}) = \int_S j\omega\rho_0 \mathbf{u}_n(\mathbf{l}_0) \frac{e^{jkl}}{2\pi l} dS \quad (89)$$

Further simplification is possible for far-field sound power calculations. Returning the time dependence, equation (86) reduces to

$$P(\mathbf{l}, t) \equiv \frac{j\omega\rho_0 e^{j\omega t}}{2\pi L_0} \int_S \mathbf{u}_n(\mathbf{l}_0) e^{jkl} dS \quad (90)$$

where L_0 is the average distance from the plate to the point of interest.

Equation (87) was implemented in MATLAB. The two-dimensional Gaussian quadrature was also used to evaluate this surface integral. This model will eventually be compared with experimental measurements of the far-field sound pressure radiated from a composite plate mounted in a rigid baffle in a free-field environment.

Noise Control Experiment

An acoustic noise control experiment has been designed to test the effectiveness of PFC actuators for controlling the vibration of a plate. By controlling the structural modes of the plate excited with some acoustic or structural noise source, PFC's may reduce the level of sound radiated from the surface of the plate. Previous studies have demonstrated the effectiveness of this concept using monolithic piezoceramics [Fuller *et al*, 1992]. These experiments typically use feedback control to minimize the sound radiated. Sensor information is obtained from error microphones in the far field, or surface mounted sensors, such as PVDF film. Feedforward control can also be used for harmonic or narrow band disturbances, which may be applicable to the aircraft/rotorcraft noise problems related to the blade passage frequency. The primary objective of the proposed experiment is to improve the noise control performance using the anisotropic actuation capabilities of the PFC.

The initial design for the experiment was modeled after work by Clark and Fuller [1991, 1992]. In their experiments, multiple piezoceramic actuators were bonded to the surface of a roughly 30 cm square plate which was mounted in a wooden baffle. The tests were performed in an anechoic chamber to achieve a free field environment. Similarly, the current experimental design, shown in Figure D-2, will be performed in the anechoic facility. A plate mount and wooden baffle will be arranged within an existing microphone track. The microphone track can be used to automatically measure the sound pressure field at discrete locations in a hemisphere around the test article. Disturbance sources will be input from the opposite (lower) side of the plate.

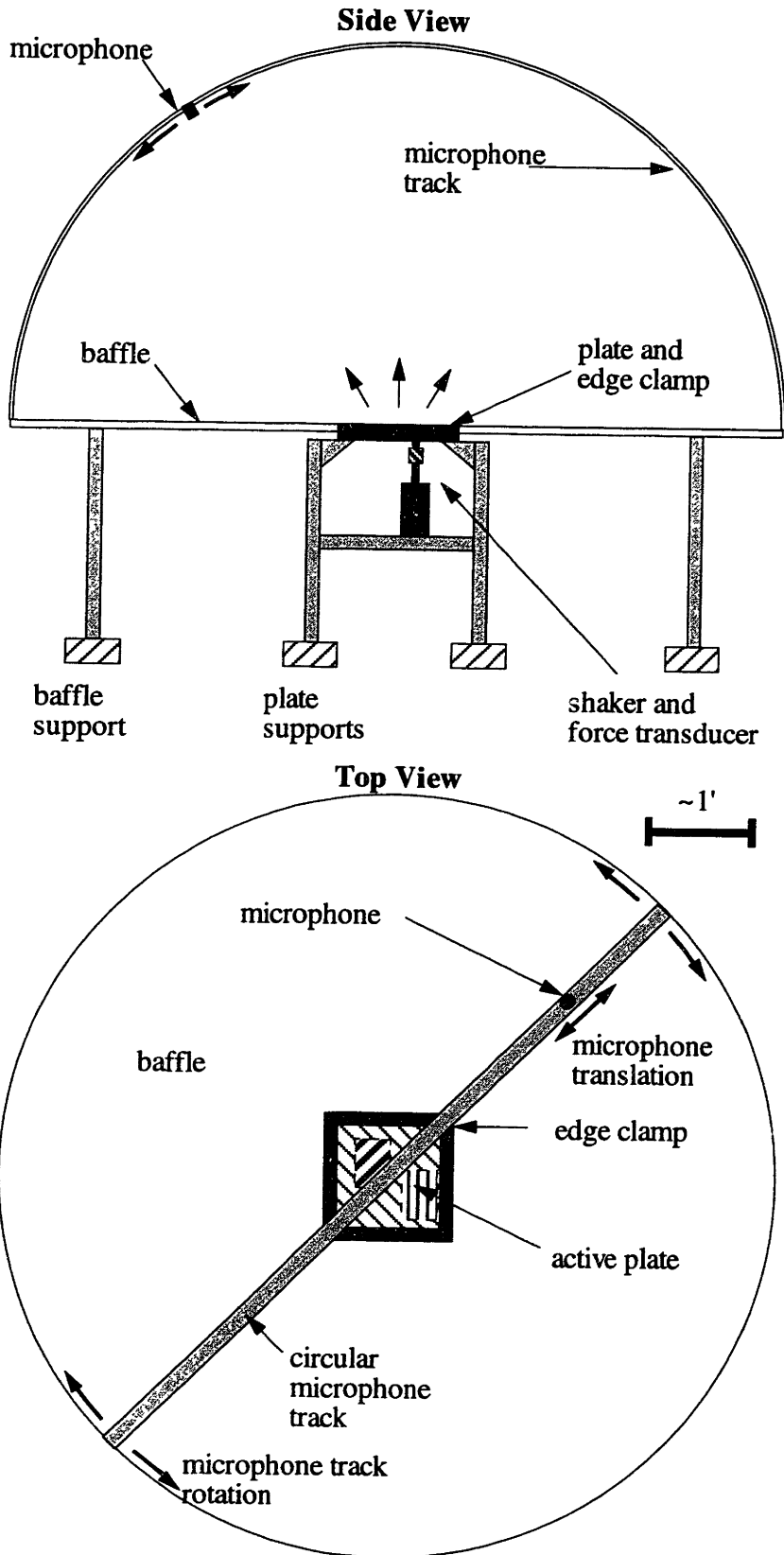


Figure D-2. Preliminary design for noise control experiment.

Glossary

Acronyms

CLPT: Classical Laminated Plate Theory

DAP: Directionally Applied Piezoceramic

DUF: Discretized Uniform Fields Model

GNPT: Guaranteed Nonporous Teflon

IDE: Interdigitated Electrodes

IDE-PFC: Interdigitated Electrode Piezoelectric Fiber Composite

MEK: Methyl Ethyl Ketone, solvent

MIT: Massachusetts Institute of Technology

PFC: Piezoelectric Fiber Composite

PVDF: Polyvinylidene Difluoride, piezopolymer

PZT: Lead Zirconate Titanate, piezoceramic

SERC: Space Engineering Research Center, MIT

TELAC: Technology Laboratory for Advanced Composites, MIT

Words

actuator: A device used to deform a structure in a constructive manner.

adaptive structure: A structure designed to adapt to its environment using actuators and sensors.

- anisotropic:** Having material properties which differ in all directions and with no planes of symmetry.
- antisymmetric:** Laminate in which opposing pairs of laminae about the middle surface have the same thickness but opposite orientations of the principal material direction with respect to the laminate axes.
- arcng:** Dielectric breakdown through air.
- baffle:** Large, flat partition which inhibits sound transfer from one side to the other.
- B-stage:** An intermediate stage in the polymerization process of a thermosetting resin in which the somewhat tacky and fairly solid, but flexible.
- cocure:** Curing multiple structural elements of different types simultaneously to form a single structure.
- coercive field:** The applied electric field required to repole a piezoelectric material.
- cure:** The complete polymerization of a thermoset, such as an epoxy resin, resulting in solidification.
- Curie temperature:** The transition temperature in ferroelectric materials above which polarization is not possible due to a change in the crystal structure.
- degas:** Application of a low hydrostatic pressure to an epoxy resin in order to expand trapped gases, allowing them to rise to the surface and escape.
- ferroelectric:** Materials which exhibit the piezoelectric effect and can retain a net polarization, below the Curie temperature.
- hybrid:** Referring to a matrix material composed of more than one phase, or composition, as in a filler dispersed in an epoxy resin.
- hysteresis:** A nonlinear behavior in ferroelectrics that occurs during polarization reversal due to an applied electric field.
- lamina** (pl: laminae): One ply or layer of a composite laminate usually consisting of unidirectional fibers in a matrix.

laminate: Structure composed of multiple composite laminae having various orientations of principal material directions in order to tailor the directional dependence of the mechanical properties.

matrix: Element of a composite system which surrounds structural components, such as fibers, enhancing mechanical and possibly electrical characteristics of the composite.

monolithic piezoceramic: Volume of pure piezoelectric ceramic material used for actuation and sensing often in a thin, rectangular wafer.

orthotropic: Having material properties that differ in three mutually perpendicular directions and having three mutually perpendicular planes of symmetry.

Perovskite: A cubic crystal structure with the formula ABO_3 . A is a mono- or divalent metal ion at the corners of the unit cell and B is a tetra- or pentavalent metal ion in the body center. Oxygen ions are on the face centers.

piezoelectric: Polar material which produces a proportional surface charge for an applied stress as a result of an asymmetry in the unit crystal structure.

poling: A process in which a DC electric field greater than the coercive field is applied to a ferroelectric to create a remanent polarization.

prepreg: Form of composite ply in which the resin/matrix is in a B-stage or uncured state so that it is somewhat tacky and flexible at room temperature.

quasi-isotropic: Laminate that have essentially isotropic extensional stiffnesses as a result of the lay-up.

remanent polarization: Net alignment of the dipoles within a ferroelectric resulting from a poling process.

surfactant: Compounds that change the chemical nature of a filler system to be used in an aqueous media; Classifications include flow enhancers, coupling agents, dispersants, and anti-foaming additives.

symmetric: Laminates having symmetric geometry and material properties about the middle surface.

thermosei: Polymer that becomes hard and rigid after being cured, and cannot be reshaped as in a thermoplastic.

References

- Abramowitz, Ed. M. and I.A. Stegun, Handbook of Mathematical Functions, AMS 55, U.S. Dept. of Commerce, 1964, pp.916-9.
- Anderson, Eric H., and E. F. Crawley, "Piezoceramic Actuation of One- and Two-Dimensional Structures," MIT Space Engineering Research Center Report #5-93, March 1993.
- Arfken, George, Mathematical Methods for Physicists, Academic Press, Inc., New York, 1985, pp.573-7, 637-50.
- ASTM, "Standard Test Method for Tensile Properties of Polymer Matrix Composite Materials," D 3039/D 3039M-93, Annual Book of ASTM Standards, Vol. 15.03, ASTM, Philadelphia, 1993, pp.118-27.
- Barrett, R., "Intelligent Rotor Blade and Structures Development Using Directionally Attached Piezoelectric Crystals," M.S. Thesis, Dept. of Aerospace Engineering, U. of Maryland, College Park, 1990.
- Barrett, R., "Aeroservoelastic DAP Missile Fin Development," *Third International Conference on Adaptive Structures*, San Diego, CA, 1992, pp.70-84.
- Bent, Aaron A., Unpublished data on effective PFC properties, August 1994.
- Bent, Aaron A. and Castro, Z., Unpublished results for the coercive field of PZT5H-type ceramics versus temperature, August 1993.
- Bent, Aaron A., and Nesbitt W. Hagood, "Improved Performance in Piezoelectric Fiber Composites Using Interdigitated Electrodes," Paper No. 2441-50, *SPIE Proceedings of the 1995 North American Conference on Smart Structures and Materials*, San Diego, 1995.

- Bent, Aaron A., and Nesbitt W. Hagood, "Piezoelectric Fiber Composites for Structural Actuation," MIT Space Engineering Research Center Report #6-94, January 1994.
- Bent, A.A., Hagood, N.W., and J. P. Rodgers, "Anisotropic Actuation with Piezoelectric Fiber Composites," *J. Intel. Mat. Syst. and Struct.*, 1995.
- Berlincourt, D., Krueger, H, and C. Near, "Important Properties of Morgan Matroc Piezoelectric Ceramics," TP-226, Electro Ceramics Division, Morgan Matroc, Inc., Bedford, OH.
- Blevins, R. D., Formulas for Natural Frequency and Mode Shape, Robert Krieger Pub. Co., Malabar, FL, 1987, pp.108, 253-68.
- Boll, David, Telephone Conversation, Hercules Inc., October 1994.
- Butler, John L. "Application Manual for the Design of Etrema Terfenol-D Magnetostrictive Transducers," Etrema Products, Inc., Ames, IA, 1988.
- Chan, Kin H., and Nesbitt W. Hagood, "Nonlinear Modeling of High Field Ferroelectric Ceramics for Structural Actuation," MIT Space Engineering Research Center Report #13-94, July 1994.
- Charon, W., and H. Baier. "Active Damping and Compensation of Satellite Appendages," IAF Paper No. 93-222, *Proceedings of the 44th Congress of the International Astronautical Federation*, Graz, Austria, 1993.
- Chen, P., and I. Chopra, "Hover Testing of a Smart Rotor with Induced-Strain Actuation of Blade Twist," AIAA Paper No. 95-1097, *Proceedings of the 36th AIAA/ASME/ASCE/AHS/ASC Structures, Structural Dynamics, and Materials Conference*, New Orleans, LA, 1995.
- Chia, C. Y., Nonlinear Analysis of Plates, Ch. 1, McGraw-Hill International, NY, 1980, pp.1-5.
- Clark, Robert L. and C. R. Fuller, "Control of Sound Radiation with Adaptive Structures," *J. of Intell. Mater. Syst. and Struct.*, 2(3), July 1991, pp.431-52.

- Clark, Robert L. and C. R. Fuller, "Experiments on Active Control of Structurally Radiated Sound Using Multiple Piezoceramic Actuators," AIAA 90-1172, *J. Acoust. Soc. Amer.*, 91(6), 1992, pp.3313-20.
- Crandall, S. H., Karnopp, D. C., Kurtz, E. F. Jr., and D. C. Pridmore-Brown, Dynamics of Mechanical and Electromechanical Systems, Robert E. Krieger Pub. Co., Malabar, FL, 1968.
- Crawley, E.F. and de Luis, J., "Use of Piezoelectric Actuators as Elements of Intelligent Structures," *AIAA Journal*, 25(10), 1987, pp.1373-85.
- Crawley, E.F., and K. B. Lazarus, "Induced Strain Actuation of Isotropic and Anisotropic Plates," *AIAA Journal* , 29 (6), 1989, pp.944-51.
- de Luis, Javier, Crawley, E. F., and Steven R. Hall, "Design and Implementation of Optimal Controllers for Intelligent Structures Using Infinite Order Structural Models," Space Systems Laboratory Report # 3-89, MIT, January 1989, Ch.4.
- DuPont Kapton Polyimide Film," Adhesion to Kapton," Bulletin H-12, Du Pont Co., Wilmington, DE.
- Ehlers, Steven M., and Terrence A. Weisshaar, "Effect of Adaptive Material Properties on Static Aeroelastic Control," *Proceedings of the 33th AIAA/ASME/ASCE/AHS/ASC Structures, Structural Dynamics, and Materials Conference*, Dallas, TX, 1992, pp.914-924.
- Fripp, Michael, "Distributed Structural Actuation and Control with Electrostrictors," S.M. Thesis, Massachusetts Institute of Technology, 1995.
- Fuller, C. R., Rogers, C. A., and H. H. Robertshaw, "Control of Sound Radiation With Active/Adaptive Structures," *J. of Sound and Vibration* , 157 (1), p.19-39, 1992.
- Ghandi, Kamyar. "Shape Memory Ceramic Actuation of Adaptive Structures," *AIAA Journal*, Submitted for publication 1994.
- Hagood, N.W. and A. A. Bent, "Development of Piezoelectric Fiber Composites for Structural Actuation," AIAA Paper No. 93-1717, *Proceedings of the 34th AIAA Structures, Structural Dynamics, and Materials Conference*, La Jolla, CA, 1993.

- Hagood, N.W., Chung, W.H., and A. von Flotow, "Modeling of Piezoelectric Actuator Dynamics for Active Structural Control," *J. Intell. Mater. Syst., and Struct.* (1), 1990, pp.327-54.
- Hagood, N.W., Kindel, R., Ghandi, K., and P. Gaudenzi, "Improving Transverse Actuation of Piezoceramics Using Interdigitated Surface Electrodes." SPIE Paper No. 1917-25, *Proceedings of the 1993 North American Conference on Smart Structures and Materials*, Albuquerque, NM, 1993, pp.341-52.
- Hall, S. R., Crawley, E. F., How, J. P., and B. Ward, "Hierarchic Control Architecture for Intelligent Structures," *J. Guidance, Control, and Dynamics*, 14 (3), 1991, pp.503-12.
- Hercules Magnamite Product Data, Number 844, "AS/3501-6 Prepreg Tape," Magna, UT.
- IEEE Std 176-1978, *IEEE Standard on Piezoelectricity*, The Institute of Electrical and Electronics Engineers, 1978.
- Jaffe, B., Cook, W. R., and H. Jaffe, Piezoelectric Ceramics, R.A.N. Pub., Marietta, 1971.
- Jensen, D. W., Crawley, E. F., and J. Dugundji, "Vibration of Cantilevered Graphite/Epoxy Plates With Bending-Torsion Coupling," *J. Reinforced Plastics and Composites*, Vol. 1, 1982, pp. 254-69.
- Jia, J. and C. A. Rogers, "Formulation of a Laminated Shell Theory Incorporating Embedded Distributed Actuators," *Adaptive Structures*, AD-Vol. 15, Ed: B.K. Wada, ASME, NY, 1989, pp.25-34.
- Jones, R.M., Mechanics of Composite Materials, Hemisphere Pub. Corp., New York, 1975, Ch. 2, 4.
- Kane, J. L., "Oriented Noncontinuous Boron Composites," *J. Comp. Mat.*, Vol. 1, 1967, pp.42-52.
- Lanczos, C., The Variational Principle of Mechanics, U. of Toronto Press, Toronto, Canada, 1949.

- Lazarus, Kenneth B., and E.F. Crawley, "Induced Strain Actuation of Composite Plates," Gas Turbine Laboratory Report #197, MIT, March 1989.
- Lester, H.C. and R. J. Silcox, "Active Control of Interior Noise in a Large Scale Cylinder Using Piezoelectric Actuators," *NASA 4th Aircraft Interior Noise Workshop*, N92-32958, 1992.
- Lin, C., Crawley, E. F., and J. Heeg, "Open Loop and Preliminary Closed Loop Results of a Strain Actuated Active Aeroelastic Wing," AIAA Paper No. 95-1386, *Proceedings of the 36th AIAA/ASME/ASCE/AHS/ASC Structures, Structural Dynamics, and Materials Conference*, New Orleans, 1995.
- Masters, Alan R., and James D. Jones, "Basic Design Guidelines for Embedded Piezo-Actuators in a Layered Composite Structure," SPIE, *Proceedings of the 1993 North American Conference on Smart Structures and Materials*, Albuquerque, NM, 1993, pp.329-40.
- Meirovitch, Leonard, Computational Methods in Structural Dynamics, Sijthoff & Noordhoff, Rockville, MD, 1980, pp.286-99.
- Newnham, R. E., Bowen, L. J., Klicker, K. A., and L. E. Cross, "Composite Piezoelectric Transducers," *Materials in Engineering*, Vol. 2, 1980, pp.289-94.
- Newnham, R. E., and Gregory R. Ruschau, "Electromechanical Properties of Smart Materials," *J. of Intelligent Material Systems and Structures*, Vol. 4, July 1993.
- Norton, M. P. Fundamentals of Noise and Vibration Analysis for Engineers, Cambridge University Press, New York, 1989, pp.170-4.
- Parish, M., CeraNova Corp., 14 Menfi Way, Hopedale, MA, 01747.
- Piezo Systems, Inc., Product Catalog 2, Cambridge, MA, 1993.
- Prechtel, E. F., "Development of a Piezoelectric Servo-Flap Actuator for Helicopter Rotor Control," S.M. Thesis, MIT, 1994.
- Press, William H., Flannery, Brian P., Teukolsky, Saul A., and William T. Vetterling, Numerical Recipes, Cambridge University Press, 1986, pp.121-30.

- Rodgers, J. P., and N. W. Hagood, "Manufacture of Adaptive Composite Plates Incorporating Piezoelectric Fiber Composite Plies," AIAA Paper No. 95-1096, *Proceedings of the 36th AIAA/ASME/ASCE/AHS/ASC Structures, Structural Dynamics, and Materials Conference*, New Orleans, 1995.
- Rogers, C. A., Liang, C., and J. Jia, "Behavior of Shape Memory Alloy Reinforced Composite Plates," AIAA Paper No. 89-1389, *Proceedings of the 30th AIAA/ASME/ASCE/AHS/ASC Structures, Structural Dynamics and Materials Conference*, 1989, pp.2011-7.
- Shell Chemical Co., Product Data Sheet for Epon 9405 and Epicure 9470.
- Skeist, Irving, Handbook of Adhesives, Reinhold Pub. Corp., London, 1962, pp.ix-xv, 323-32.
- Smith, W.A., "The Role of Piezocomposites in Ultrasonic Transducers," *Proceedings of the 1989 IEEE Ultrasonics Symposium*, Montreal, Quebec, October 1989.
- Spangler, R. L., and S. R. Hall, "Piezoelectric Actuation for Helicopter Rotor Control," AIAA Paper No. 90-1076CP, *Proceedings of the 31st AIAA/ASME/ASCE/AHS Structures, Structural Dynamics, and Materials Conference*, Long Beach, CA, 1990.
- Timoshenko, S., and S. Woinowsky-Krieger, Theory of Plates and Shells, McGraw-Hill, London, 1959, pp.417-8.
- Wada, B. K., Fanson, J. L., and E. F. Crawley, "Adaptive Structures," *Adaptive Structures*, AD-Vol. 15, Ed. B.K. Wada, ASME, NY, 1989, pp.1-8.
- Waller, David J., and Ahmad Safari, "Piezoelectric Lead Zirconate Titanate Ceramic Fiber/Polymer Composites," *J. Am. Ceram. Soc.* 75(6), 1992, pp.1648-55.
- Wareham, Scott T., "Diagram of Prepreg Line 4," HAMSCO, Composite Products Group, Bacchus Plant 3, 1993.

- Warkentin, D. J., Crawley, E.F., and S. D. Senturia, "The Feasibility of Embedded Electronics for Intelligent Structures," *J. Intel. Mat. Sys. & Str.*, 3 (3), 1992, pp.462-82.
- Wegman, Raymond F., Surface Preparation Techniques for Adhesive Bonding, Noyes Pub., New Jersey, 1989, pp.80-7.
- Wetherhold, Robert C., and Nandakumar Panthalingal, "Piezoelectric PZT/Epoxy Composites for Sensing and Actuating Torsional Motion," SPIE, *Proceedings of the 1993 North American Conference on Smart Structures and Materials*, Albuquerque, NM, 1993, pp.266-74.
- Whitney, J. M., Structural Analysis of Laminated Anisotropic Plates, Technomic Pub. Co., Lancaster, PA, 1987.
- Yoshikawa, S., Selvaraj, U., Brooks, K.G., and Kurtz, S.K., "Piezoelectric PZT Tubes and Fibers for Passive Vibrational Damping," *IEEE ISAF '92*, Greenville, SC, 1992.



THESIS PROCESSING SLIP

FIXED FIELD III _____ name _____

index _____ biblio _____

► COPIES Archives Aero Dewey Eng Hum
Lindgren Music Rotch Science

TITLE VARIES ► _____

NAME VARIES ► Patrick

IMPRINT (COPYRIGHT) _____

► COLLATION 165 p

► ADD DEGREE _____ ► DEPT _____

SUPERVISORS: _____

NOTES

cat'r

date

► DEPT Aero

page
<u>J119</u>

► YEAR. 1995 ► DEGREE M.S.

► NAME RODGERS, John P.

